

**ADVANCED SOLUTIONS FOR THERMAL MANAGEMENT AND
RELIABILITY OF GALLIUM NITRIDE-BASED HIGH ELECTRON
MOBILITY TRANSISTORS ON DIAMOND SUBSTRATES**

A Thesis
Presented to
The Academic Faculty

by

Nicholas J. Hines

In Partial Fulfillment
of the Requirements for the Degree
Master of Science in the
School of Mechanical Engineering

Georgia Institute of Technology

May, 2019

COPYRIGHT © 2019 BY NICHOLAS J. HINES

**ADVANCED SOLUTIONS FOR THERMAL MANAGEMENT AND
RELIABILITY OF GALLIUM NITRIDE-BASED HIGH ELECTRON
MOBILITY TRANSISTORS ON DIAMOND SUBSTRATES**

Approved by:

Dr. Samuel Graham, Advisor
School of Mechanical Engineering
Georgia Institute of Technology

Dr. Satish Kumar
School of Mechanical Engineering
Georgia Institute of Technology

Dr. Vanessa Smet
School of Electrical and Computer Engineering
Georgia Institute of Technology

Date Approved: April 5, 2019

For my Lord and Savior, Jesus Christ

ACKNOWLEDGEMENTS

The completion of this master's thesis has been an enduring labor of love and test of faith. As I reflect on this journey that began in the fall of 2015, I am filled with gratitude for all of those who have consistently invested in my growth, patiently supported my progress, and faithfully encouraged me toward the finish line. I would like to earnestly thank my faculty advisor, Dr. Samuel Graham, for his patient and persistent dedication to my academic success and personal growth, for his leadership and guidance throughout my academic endeavors, and for his inspiring passion and enthusiasm for our research. Embracing his advice and following his example has challenged me to deepen my understanding and broaden my intellectual perspective. I deeply appreciate the opportunity I have been afforded as a graduate student in the Graham Group. I would also like to thank my thesis committee members: Dr. Satish Kumar and Dr. Vanessa Smet for their time and service on my committee and for their insight and encouragement.

I would like to thank the Defense Advanced Research Projects Agency (DARPA) and Honeywell for their financial support in funding my research and all of the participating members of the DARPA Diamond Round Robin Program, the Honeywell Radar 2021 Consortium, and the Georgia Tech 3D Systems Packaging Research Center (PRC) for providing numerous novel materials and devices for measurement, for their collaboration and feedback on my research, and for their forthcoming contributions to joint projects. I would like to thank the National GEM Consortium, Corning Incorporated, and the Woodruff School of Mechanical Engineering at Georgia Tech for their financial support in my GEM PhD Fellowship and Georgia Tech President's Fellowship. I would

also like to extend a special thanks to Dr. Tia Jackson-Truitt, Dr. Felicia Benton-Johnson, and the rest of the Georgia Tech Center for Engineering Education and Diversity (CEED) staff for their mentorship, encouragement, and financial support via the Peer to Peer (P2P) Mentoring Program and the Graduate Student RISE Scholarship.

Furthermore, I am extremely grateful for the laboratory training and tutorials, technical insight, moral support, encouragement, and friendship from my peers in the Graham Group (in no particular order and a few outside the group): Dr. Georges Pavlidis, Dr. Luke Yates, Kenechi Agbim, Dr. Brian Foley, Zhe Cheng, Dr. Darshan Pahinkar, Dr. Kyungjin Kim, Dr. Wale Odukamaiya, Samuel Kim, Jason Hirschey, Brian Kelly, Gabriel Cahn, Michael Sulkis, Priyanka Deo, Angelica Connor, Myela Paige, Kirkland Malcolm, Dr. Ankit Singh, Dr. Minseok Ha, Waylon Puckett, and Dr. Anne Mallow. I would like to give a special thanks to Dr. Georges Pavlidis, Dr. Luke Yates, Dr. Brian Foley, and Zhe Cheng for their direct contributions to and in support of this work.

I would like to thank my loving wife, Dominique Michelle Grasty Hines, for her faithful support and encouragement despite her daily adversities in medical school, for her conviction to challenge my character whenever I get in my own way, and for joyfully celebrating all of my victories no matter how small. I would like to thank my parents, my brother, and the rest of my extended family and friends for all of their loving patience and support. I would not be the man or husband I am today if it were not for all of their sacrificial love for my wife and me.

All of this would not have been possible without the love and grace of my Lord and Savior, Jesus Christ. It has only been through fullness of life and power that comes from God that I have accomplished this work.

TABLE OF CONTENTS

ACKNOWLEDGEMENTS	iv
LIST OF TABLES	ix
LIST OF FIGURES	x
CHAPTER 1. Introduction	1
1.1 RF Electronics	1
1.2 AlGaN/GaN High Electron Mobility Transistors	3
1.2.1 Overview of Device Physics	3
1.2.2 Reliability Challenges and Implications	9
1.3 Advanced Thermal Management Solutions	14
1.3.1 Diamond for Passive Heat Spreading	14
1.4 Research Overview	17
CHAPTER 2. Thermal Transport in PCD Films	20
2.1 Introduction.....	20
2.1.1 Chemical Vapor Deposition.....	20
2.1.2 Thermal Characterization: Challenges and Motivation	24
2.2 Sample Preparation and Design	26
2.3 Methodology for In-Plane Thermal Conductivity Characterization	30
2.3.1 Particle-Assisted Raman Thermometry	33
2.3.2 Electrical Resistance Thermometry	39
2.3.3 Steady-State Thermal Finite Element Model.....	44
2.4 Uncertainty and Error Analysis	47
2.4.1 Uncertainty: Monte Carlo Simulation.....	48
2.4.2 Uncertainty: Analytical Derivation.....	49
2.4.3 Uncertainty: Sensitivity Analysis	52
2.4.4 Error Analysis	56
2.5 Experimental Results and Discussion	60
2.6 Summary and Conclusions	67
CHAPTER 3. PCD Substrate Implementation: Growth vs Bonding	69
3.1 Introduction to GaN-on-Diamond Fabrication.....	69
3.1.1 AlGaN/GaN Heteroepitaxy on Single-Crystal Diamond.....	71
3.1.2 AlGaN/GaN Heterostructure Transfer: PCD Growth and Bonding	72
3.1.3 GaN-on-PCD Challenges: Thermal Boundary Resistance	73
3.1.4 GaN-on-PCD Challenges: Material Quality and Residual Stress.....	75
3.2 Stress Metrology Techniques	79
3.2.1 Stress Metrology via Raman Spectroscopy	79
3.2.2 Stress Measurement via Photoluminescence Spectroscopy.....	84
3.3 Sample Details and Experimental Apparatus	87
3.3.1 Sample Details	87
3.3.2 Experimental Apparatus.....	90

3.4	Results and Discussion.....	95
3.4.1	3D Stress Mapping of GaN.....	95
3.4.2	Steady-State Thermal Modeling: PCD Substrates Compared	108
3.5	Summary and Conclusions	118
CHAPTER 4.	Conclusions and Future Work	120
4.1	Research Summary	120
4.2	Future Work.....	123
REFERENCES	125

LIST OF TABLES

Table 1. FEM parameters explored in the sensitivity analysis of a NCD suspended membrane with backside-deposited Al shown in Figure 20.	56
Table 2. Experimental in-plane thermal conductivity ($k_{ }$) results obtained from TiO ₂ particle-assisted Raman thermometry, ERT, and the 1D lateral thermal conduction approximation. A dash indicates data that was not measured and is otherwise unknown. The note of N/A indicates that the 1D thermal transport simplifying assumption is not applicable due to the presence of backside aluminum.	61
Table 3. Linear temperature and biaxial stress conversion coefficients and strain-free reference peak positions for Raman spectroscopy and photoluminescence (PL) determined from literature. The conversion coefficient subscripts denote the spectrum peak indicated in the first column. All measurement uncertainties (abbreviated as ‘Unc’) were derived from 95% confidence intervals.....	84
Table 4. Thermal conductivity of materials and GaN-substrate thermal boundary resistances (TBR_{eff}) used in the FEM of the GPA.	111

LIST OF FIGURES

Figure 1. Material properties [2] of semiconductor materials used to fabricate FET devices.	
The superior material properties of GaN and the capability of forming a dopant-free 2DEG at the AlGaIn-GaN heterojunction make GaN ideal for high-power RF applications.	3
Figure 2. Schematic of (a) the crystal structure of wurtzite Ga- and N-face GaN and the polarization-induced sheet charge density (σ) caused by the (b) spontaneous polarizations (P_{SP}) only and (c) both the spontaneous and piezoelectric polarizations (P_{SP} and P_{PE} respectively) in Ga- and N-face AlGaIn/GaN heterostructures adapted from literature [6].	5
Figure 3. Schematic of a typical (un-field-plated) AlGaIn/GaN HEMT cross-section annotated with typical layer thicknesses, channel and gate lengths, and the general location of the acute self-heating or hot spot. The indicated channel and gate lengths are typical for RF applications [2].	7
Figure 4. A typical process flow for fabricating an AlGaIn/GaN HEMT device reproduced from literature [2].	7
Figure 5. Representation of the most critical regions of degradation in the drain-source I-V characteristics during RF operation of an AlGaIn/GaN HEMT device along three different classes of load lines measured at the same output power of 35 dBm that has been reproduced from literature [7].	9
Figure 6. (a) Representative AlGaIn/GaN HEMT device geometry with thermal and structural boundary conditions for an electro-thermo-mechanical FEM	

presented in literature [9]. The two labeled locations are the gate foot print (GFP), where high amounts of mechanical stress have been shown to develop, and the region directly below the gate-connected field plate (GCFP), where stress is typically probed optically via Raman spectroscopy. (b) Electro-thermal FEM results that show the electric field distribution (top row) and Joule heating (bottom row) near the drain-side of the gate. [9]	11
Figure 7. Mechanical degradation at the drain-edge of the gate of an AlGaIn/GaN HEMT [2].	12
Figure 8. (a) Transient electro-thermo-mechanical FEM stress results reported in literature [9] from a 5 x 1 nm area within the AlGaIn layer near the drain-side of the gate of AlGaIn/GaN HEMT as depicted in (b). (b) 2D stress map before the end of the first ON state as indicated with the vertical line (green) in (a). [9].	14
Figure 9. Schematic of the chemical and physical processes occurring during diamond CVD [34].	22
Figure 10. Examples of common types of diamond CVD reactor. (a) Hot filament, (b) “NIRIM-type” microwave plasma reactor [36], (c) “ASTEX-type” microwave plasma reactor [37], (d) DC arc jet (plasma torch). [34].	22
Figure 11. Schematic of the global coordinate system used to identify NCD samples distributed amongst the participating members of the DARPA Round Robin Program [33]. The concentric circles denote the wafer periphery. The outer circle indicates the wafer perimeter and the inner circle indicates the region of the wafer with uniform NCD film thickness. NCD film thickness non-uniformity within the inner circle was measured to be less than 1 % [49].	28

Figure 12. NCD suspended membrane sample (a) design, (b) microscope image, and (c) schematic taken from the FEM. The nominal dimensions of the suspended membrane perimeter and 1D region are shown.	30
Figure 13. (a) Schematic of the steady-state thermometry techniques, particle-assisted Raman thermometry and electrical resistance thermometry (ERT), used to measure the suspended nanocrystalline diamond (NCD) membrane samples, and (b) the finite element model (FEM) used to extract the NCD in-plane thermal conductivity.....	32
Figure 14. Experimental setups for the particle-assisted Raman thermometry and electrical resistance thermometry (ERT) techniques.	33
Figure 15. (a) Microscope image of TiO ₂ nanoparticle aggregates. (b) Measured Raman spectra of TiO ₂ and hBN particles deposited on NCD suspended membranes.	36
Figure 16. (a) Schematic of the NCD suspended membrane samples with dimensions of the metal lines used as RTDs. (b) Temperature rise along the length of the NCD suspended membrane calculated according to the FEM. Notice that the temperature rise measured from RTD 1 (dashed) is averaged across the entire membrane length and therefore is less than the isothermal maximum temperature present within the 1D Conduction Regime.	41
Figure 17. Finite element model (FEM) (a) geometry, (b) temperature map, and (c) x-directional heat flux map of an NCD suspended membrane sample (Sample B). The substrate and substrate-supported NCD film are not shown for visual clarity.	46

Figure 18. Flow chart summary of the Monte Carlo (MC) simulation implemented for determining the best-fit NCD in-plane thermal conductivity, k_{\parallel} , and the MC-based uncertainty, k_{\parallel}^{MC} . Experimental results shown in Table 2 demonstrate that $\delta k_{\parallel}^{MC} \approx 3\%$ on average.	49
Figure 19. Individual component uncertainties (each component uncertainty = $\partial T \partial p \delta p$ for component p) of exemplary TiO_2 particle-assisted Raman thermometry and ERT temperature measurements.	52
Figure 20. Sensitivity analysis results of an NCD suspended membrane with backside-deposited Al for which input parameters are listed in Table I. (a) Sensitivity as a function of (NCD) k_{\parallel} . The sensitivities to (NCD) k_{\parallel} and t_{NCD} are indistinguishable and shown as one curve (black). The sensitivities to k_{Al} and t_{Al} are indistinguishable and shown as one curve (blue). The sensitivities to η , G_1 , G_2 , G_3 , and T_b are negligibly low and omitted for clarity. (b) Sensitivity-based uncertainty in k_{\parallel} (δk_{\parallel}^S) as a function of k_{\parallel} demonstrates that $\delta k_{\parallel}^S \approx 2.5\%$ for our NCD samples.	55
Figure 21. Temperature dependent thermal conductivity measurement results as a function of average membrane temperature calculated from the best-fit FEM from sample 1b. The vertical error bars represent the total in-plane thermal conductivity uncertainty, δk_{\parallel} . The larger vertical error bars for $T_{avg} < 50$ °C indicate increased uncertainty due to an insufficient average temperature rise, $\Delta T_{avg} = T_{avg} - T_b$, where T_b is the sample base temperature.	58
Figure 22. Comparative model error analysis between FEM and Fourier's law assuming 1D thermal conduction. The dashed line indicates the conditions that yield 1D	

assumption model error less than 5% ($\varepsilon_{1D} < 5\%$) (a) 1D assumption model error (ε_{1D}) as a function of NCD in-plane thermal conductivity (k_{\parallel}) input to the FEM. Linear power density along the centerline heater (Q/t in Equation 9) was held constant to maintain a nearly constant temperature rise (ΔT in Equation 9). (b) 1D assumption model error (ε_{1D}) as a function of length-to-width aspect ratio. 60

Figure 23. Temperature profile measured from sample 2a via TiO_2 particle-assisted Raman thermometry and electrical resistance thermometry (ERT) with 200 mW dissipated from the centerline heater (RTD 1). The independent steady-state thermometry techniques demonstrated precise agreement with the finite element model (FEM). The average membrane temperature, $T_{avg} = 62.8\text{ }^{\circ}\text{C}$, calculated via the FEM is denoted by the dashed line. As discussed in Section 2.3.2, the temperature measured from RTD 1 understated the peak membrane temperature. 62

Figure 24. Histograms resulting from the MC simulations used to propagate the experimental temperature uncertainties from (a) Raman thermometry and (b) ERT measurements from sample 2a into MC-based uncertainties, $\delta k_{\parallel}^{MC}$ 63

Figure 25. Temperature profile measured from sample 4 ($3\text{ }\mu\text{m}$) via TiO_2 particle- assisted Raman thermometry with 200 mW and 800 mW dissipated from the centerline heater. The k_{\parallel}^{Raman} results of $157 \pm 8\text{ W/mK}$ and $158 \pm 8\text{ W/mK}$ measured with temperature rises of $21.5\text{ }^{\circ}\text{C}$ and $84\text{ }^{\circ}\text{C}$, respectively, demonstrate the possibility of resolving k_{\parallel} for low temperature rises via TiO_2 particle-assisted Raman thermometry. 64

Figure 26. Values of $k_{ }$ measured from Samples 3 and 4 (stars) compared to values of $k_{ }$ as a function of thickness reported in literature [40].	67
Figure 27. Summary of the phonon scattering mechanisms contributing to the thermal interface resistance in GaN-on-substrate composites. [77].	70
Figure 28. Schematic of typical GaN-on-diamond heterostructure transfer processes: direct growth and transfer bonding.	73
Figure 29. Schematic illustrating the accumulated strain and stress developed in epi-substrate composites during cooldown processes as a result of CTE mismatch. Cooldown processes tend to cause GaN-on-Si and GaN-on-PCD wafers to develop biaxial tension in the GaN and biaxial compression in the substrate (concave-up wafer bow) since the CTE of GaN is greater than that of Si and PCD ($CTE_{GaN} > CTE_{PCD}$) as shown in Figure 30.	77
Figure 30. Coefficients of thermal expansion (CTEs) of GaN [89], silicon (111) [90], and CVD diamond [90]. The horizontal lines denote temperature independent CTEs that result from averaging the temperature dependent CTEs ranging from 300 K (RT) to 800 K.	77
Figure 31. Crystal structure of, graphical illustration of the atomic vibration modes in, and tetrahedral bonding arrangement within hexagonal wurtzite GaN (left to right). [97]	81
Figure 32. (a) Raman response to isothermal heating of a bulk GaN substrate, and (b) Raman response to tensile stress applied to a GaN/6H-SiC template. [97]	81
Figure 33. Photoluminescence processes in direct bandgap and indirect bandgap semiconductors. Electrons and holes created by absorption of photons are	

illustrated as the shaded states in the conduction band and the empty states in the valence band, respectively. Photon absorption and emission processes are illustrated by vertical arrows according to energy and momentum conservation rules. For indirect bandgap semiconductors, photon absorption and emission requires phonon absorption or emission to conserve momentum. [97]	85
Figure 34. Room temperature PL spectra of GaN epitaxial films under tensile (GaN/6H-SiC) and compressive (GaN/4H-SiC) stress. [97]	87
Figure 35. Microscope images of the (a) bare and (b) HEMT-processed die from wafer G2 and the (c) topside and (d) backside of approximate region measured located between adjacent HEMT devices on wafer B. Stress measurements collected from the G2 bare die were collected on a “light” region away from the wafer periphery. The location of the delamination that is shown in Figure 44 is denoted in (d).	88
Figure 36. Material composition details of the grown GaN-on-PCD wafers G1 and G2, and the bonded GaN-on-PCD wafer B.	88
Figure 37. (a) Raman, (b) topside PL, and (c) backside PL measured from the GaN buffer layer within the gate-drain access region of the GaN-on-diamond HEMT from wafer G2. Each Raman peak was fitted with a single pseudo-Voigt line shape, whereas each PL peak was fitted with multiple (three) pseudo-Voigt line shapes.	93
Figure 38. Spectrometer drift accumulated throughout ~8 hours of Raman measurements of the 4H-SiC reference sample used for system calibration.	95
Figure 39. Schematic of Raman and photoluminescence stress metrology technique.	96

Figure 40. Residual biaxial stress in the GaN buffer layer of AlGaIn/GaN heterostructures of GaN-on-diamond wafers G1, G2, and B measured via Raman and PL spectroscopy. The red data labels correspond to the magnitude of the stress gradient measured across the GaN layer of each wafer sample.....	98
Figure 41. Wafer G1 Raman and PL measurement locations for assessing cross-wafer stress uniformity.....	99
Figure 42. Spatial maps of the (a) topside PL stress, (b) Raman stress, and (c) backside PL stress and (d) peak intensity measured from the GaN buffer layer located within the gate-drain access region of a GaN-on-diamond HEMT from wafer G2 shown in Figure 35. The stress extrema shown in the right side of (c) are artifacts of insufficient PL peak intensity as shown in (d). The annotations above (a), (b), and (c) indicate the spatially-averaged mean \pm uncertainty (max, min).	100
Figure 43. (a) Spatial map of the backside PL peak intensity and (b) microscope image of the backside of the 5 x 60 μm gate-drain access region (boxed) when illuminated by white light.	101
Figure 44. (a) Microscope images of the delamination at the transfer bonded GaN/PCD interface of wafer B captured from the backside of the wafer. Raman and PL stress measurements across the delamination were collected along the 200 μm line annotation. Note that the delamination is just beyond the field of view captured in the microscope images of the same devices shown in Figure 35. (b) Raman and PL stress measurement results of the delamination line scan.	103
Figure 45. (a) SEM image of cleaved GaN-on-diamond wafer G1 and (b) TEM image of the wafer G1 cross-section at the GaN-diamond interface as published in	

literature [92]. The higher dislocation density along the backside (GaN-diamond) of the GaN can clearly be seen in (b).....	106
Figure 46. Experimental and finite element simulation stress results as a function of vertical position along the cross-section of wafer G1 published by Hancock <i>et al.</i> [92]. New Raman and PL stress measurements presented in this work are superimposed in red over the literature data.	108
Figure 47. (a) Top-view of TriQuint TGA2814 GPA with active channel regions R1 and R2. (b) FEM geometry of GPA mounted on Mo/Cu heat sink. (c) Converged finite element mesh of GPA FEM. (d) Example of temperature distribution across the GPA FEM.....	111
Figure 48. (a) Mesh convergence of maximum device temperature with respect to the number of quadratic elements. (b) Simulation times for each mesh refinement of the mesh convergence analysis.	112
Figure 49. (a) Die-attach thermal resistance/impedance analysis schematic. (b) Effective die-attach impedance analysis published in literature. [114]	115
Figure 50. Effective die-attach thermal conductivity analysis performed by the parameterization of the Au/Sn solder thermal conductivity. The dashed line represents a model alternative in which the die-attach layer was removed and the total layer/interface impedance was treated as a single interface resistance. This idealization serves as a reference condition to illustrate the thermal management advantages from lateral heat spreading that are possible using high thermal conductivity interface layers.	115

Figure 51. Temperature rise as a function of dissipated power density for each GaN-on-PCD implementation alternative to GaN-on-SiC. The horizontal (black) dashed line indicates the maximum operating temperature (for maximum power density of 6.25 W/mm).	117
Figure 52. Steady-state thermal finite element analysis of an AlGaIn/GaN high-power amplifier device reproduced from literature [40] that shows the cross-plane temperature distribution through the device, substrate, and package for polycrystalline diamond thermal conductivities subject to various assumptions. Assuming an effective isotropic thermal conductivity of 1250 W/mK (at 300 K) (dashed black) yields the same peak channel temperature result as considering a (cross-plane) inhomogeneous and anisotropic thermal conductivity.	118

CHAPTER 1. INTRODUCTION

1.1 RF Electronics

Radio frequency (RF) electronics are a class of electronic systems that contain component devices that operate with an alternating electrical current with oscillations ranging roughly between the upper range of audio frequencies (20 kHz) and the lower range of infrared frequencies (300 GHz). The majority of RF electronics are used for power amplification towards a wide range of applications including: wireless communications in mobile devices and base transceiver stations, satellite communications, advanced consumer and military radar systems, and electronic warfare [1-4]. For nearly all of these applications, high output power and output power density are desired to maximize signal-to-noise ratio and minimize power losses, respectively. The mainstay component for RF electronic devices is the field-effect transistor (FET). FETs are particularly well suited for amplifying weak signals because the input power required to control the charge carrier-dense channel is much less than the output power available for an external load [2].

The high-power and high-frequency requirements of RF electronics demand that FETs are made from wide bandgap (WBG) semiconductor materials that exhibit a large breakdown field and a high saturation velocity such as silicon carbide (SiC) and gallium nitride (GaN) instead of narrow bandgap materials such as silicon (Si) and gallium arsenide (GaAs). Figure 1 shows a comparison of relevant material properties and the Johnson's figure of merit (JFOM) for these common semiconductor materials [3]. The JFOM represents the ultimate performance limits of a high-power and high-frequency FET and is expressed as

$$JFOM = \frac{E_{br}v_{sat}}{2\pi} \quad (1)$$

where E_{br} is the critical breakdown field and v_{sat} is the saturation velocity. Because of its large bandgap energy (E_g), GaN has a high critical breakdown field that allows GaN-based FETs to withstand high operational voltages before experiencing voltage breakdown. The high saturation velocity of GaN indicates that the electrons in GaN maintain a high velocity under high electric field conditions, a characteristic that is favorable for the high switching frequencies required for RF applications. Figure 1 clearly demonstrate that SiC and GaN are far superior than Si and GaAs for high-power and high-frequency FET devices. Although SiC and GaN have comparable JFOMs, GaN can form high quality and highly conductive heterojunctions (discussed in further detail in Section 1.2.1) that enable the fabrication of high-performance FETs called high electron mobility transistors (HEMTs). Due to the high cost and limited diameter of device quality bulk GaN substrates, GaN-based HEMTs have been epitaxially grown on Si, SiC, or sapphire substrates. Further, the high-temperature operating conditions typical of high-power RF devices requires a highly conductive non-native growth substrate. Hence, SiC ($k \sim 330\text{-}450 \text{ W/mK}$) is the preferred growth substrate for GaN-based HEMTs used for high-power RF applications. Commercial GaN-on-SiC HEMT devices from companies such as Qorvo currently demonstrate operation for 1 million hours for channel temperatures of 200°C with fallout rates below 0.002% [2]. However, since high power RF HEMT devices experience acute self-heating (discussed in further detail in Section 1.2.2) and are designed to withstand high operating temperatures ($> 200^\circ\text{C}$), substrates with even higher thermal conductivity such

as chemical vapor deposited diamond ($k \sim 1400\text{-}2000 \text{ W/MK}$) are under development for high-performance applications.

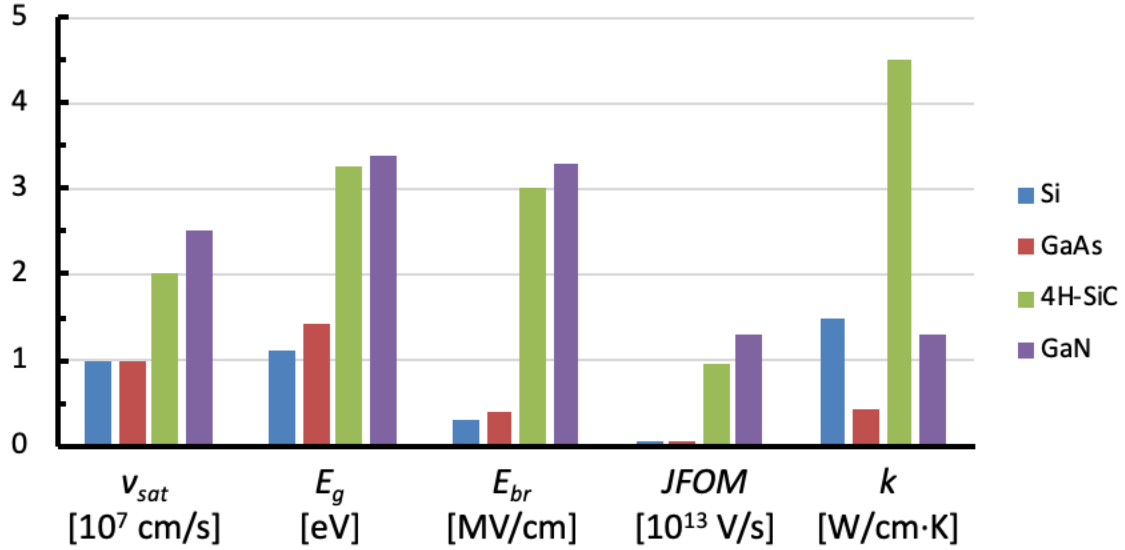


Figure 1. Material properties [2] of semiconductor materials used to fabricate FET devices. The superior material properties of GaN and the capability of forming a dopant-free 2DEG at the AlGaIn-GaN heterojunction make GaN ideal for high-power RF applications.

1.2 AlGaIn/GaN High Electron Mobility Transistors

1.2.1 Overview of Device Physics

A high electron mobility transistor (HEMT) is a field-effect transistor (FET) that relies on the formation of an electrically active channel by joining two similar semiconductor materials with unequal bandgaps such as aluminium gallium nitride (AlGaIn) and gallium nitride (GaN) to create a heterojunction. The device architecture of AlGaIn/GaN HEMTs is fundamentally different than both metal oxide semiconductor field effect transistors (MOSFETs) and AlGaAs/GaAs HEMTs and enables superior electron mobility within the active channel – called the two-dimensional electron gas (2DEG) – due to the absence of dopants that are responsible for electron mobility reduction caused by

ionized impurity scattering [5]. Instead of requiring doping to produce free charge carriers, AlGaN/GaN heterostructures rely only on the intrinsic spontaneous and piezoelectric polarizations of the AlGaN and GaN materials to induce ionized surface donor states that create free electrons (the 2DEG) with sheet charge densities in excess of 10^{13} cm^{-2} [6]. This phenomenon is possible because the intrinsic polarization and polarizability of the wurtzite crystal structure of AlGaN and GaN shown in Figure 2.

Since the wurtzite crystal structures of AlGaN and GaN are non-centrosymmetric, both materials have spontaneous electrical polarizations in a relaxed (unstrained) state. When the GaN is epitaxially grown in the Ga-face orientation, the directionality of the spontaneous polarizations creates a sheet charge density within the AlGaN at the AlGaN-GaN interface as shown in Figure 2. However, optimal charge density achieved within the 2DEG of the AlGaN/GaN heterostructure also requires the additional piezoelectric polarization of the AlGaN that is achieved by pseudomorphically growing the lattice-mismatched AlGaN under tensile strain onto the GaN [6]. This superior 2DEG charge density ($\sim 10^{13} \text{ cm}^{-2}$) enables the high current carrying capability of AlGaN/GaN HEMTs. Therefore, the high current carrying capability and superior material properties of GaN shown in Figure 1 have made AlGaN/GaN HEMTs the most promising components for high-temperature and high-power RF electronics.

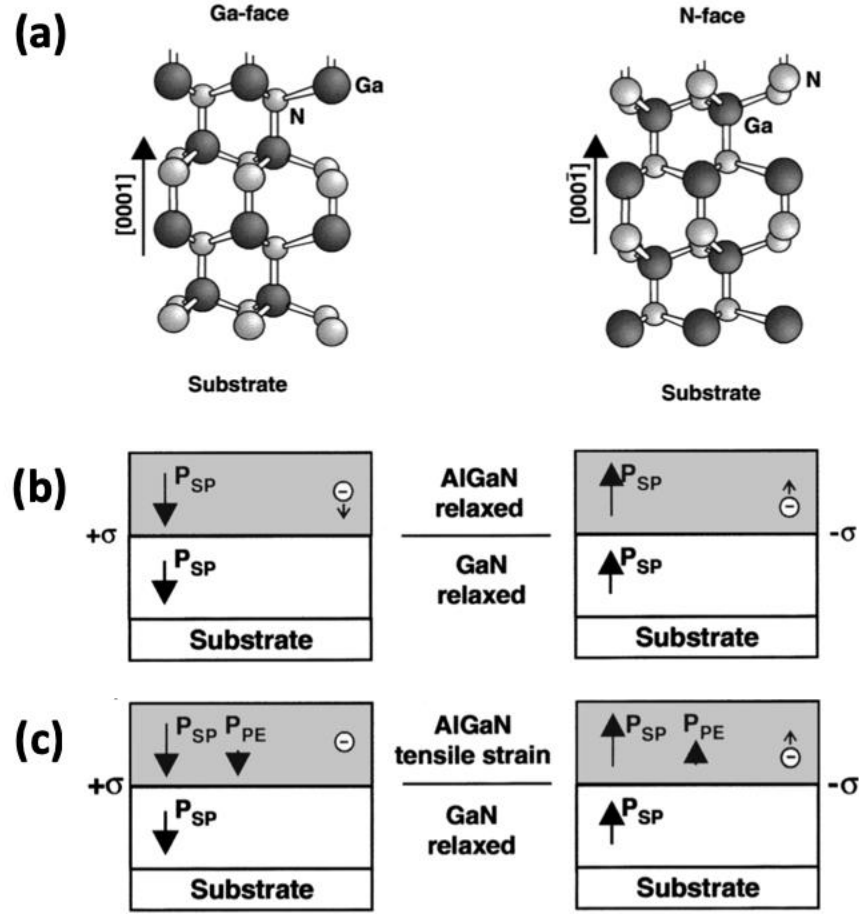


Figure 2. Schematic of (a) the crystal structure of wurtzite Ga- and N-face GaN and the polarization-induced sheet charge density (σ) caused by the (b) spontaneous polarizations (P_{SP}) only and (c) both the spontaneous and piezoelectric polarizations (P_{SP} and P_{PE} respectively) in Ga- and N-face AlGaN/GaN heterostructures adapted from literature [6].

Due to the high cost and limited availability of GaN substrates, AlGaN/GaN heterostructures are typically epitaxially grown via molecular beam epitaxy (MBE) or metal oxide chemical vapor deposition (MOCVD) on non-native substrates such as sapphire, Si, or SiC [3]. Ohmic source and drain contacts and a Schottky gate are deposited on the AlGaN/GaN heterostructure along with a dielectric passivation layer (typically SiN) to enable electrical control and to protect the heterostructure from charged surface states and contaminants, respectively. In addition, advanced metallization design schemes such as source-connected field plates and T-gates have been implemented to improve device

reliability by mitigating the highly concentrated electric field on the drain-side of the gate present under large voltage bias conditions [3]. A typical (un-field-plated) AlGaN/GaN HEMT cross-section and fabrication process flow are shown in Figure 3 and Figure 4, respectively.

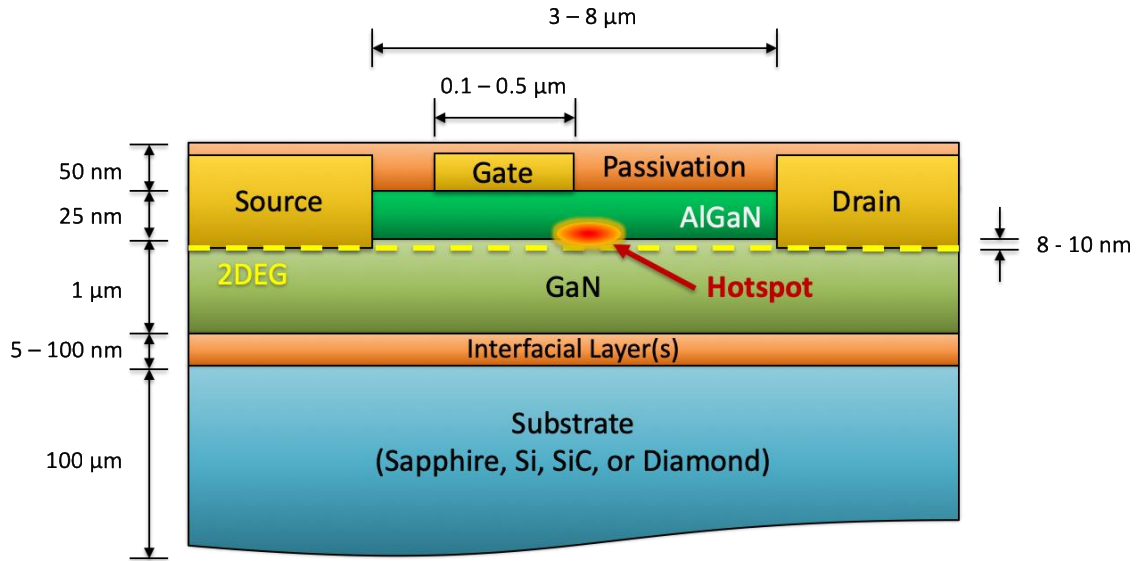


Figure 3. Schematic of a typical (un-field-plated) AlGaN/GaN HEMT cross-section annotated with typical layer thicknesses, channel and gate lengths, and the general location of the acute self-heating or hot spot. The indicated channel and gate lengths are typical for RF applications [2].

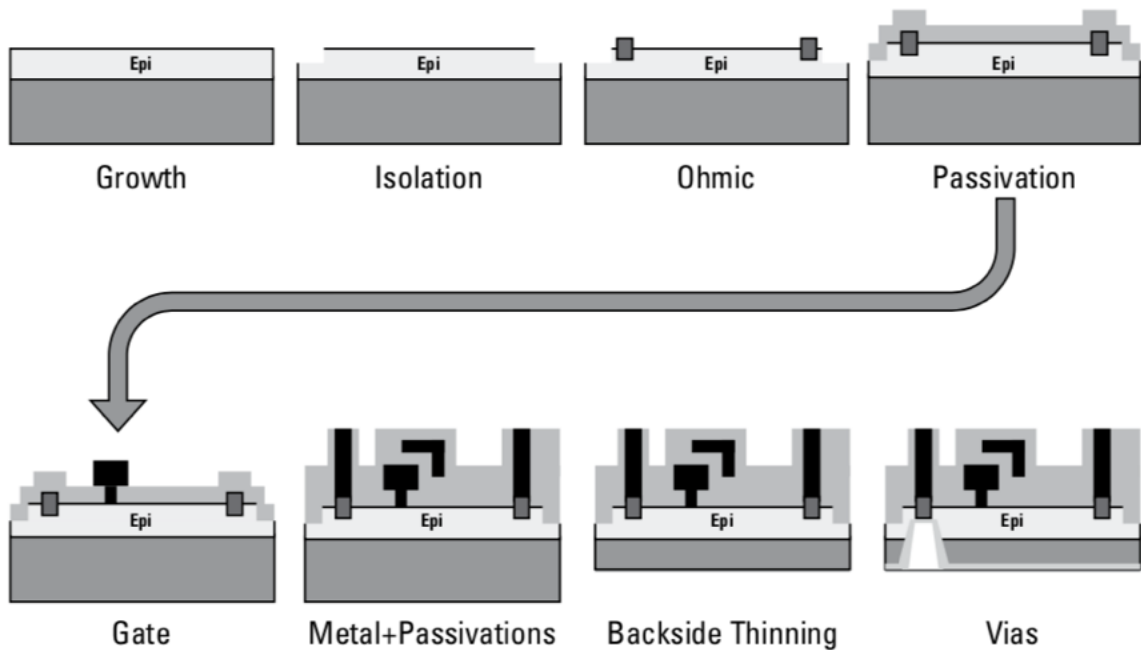


Figure 4. A typical process flow for fabricating an AlGaN/GaN HEMT device reproduced from literature [2].

The electrical power output of a HEMT is controlled by manipulating the applied voltage or bias conditions between three electrical terminals: the source, gate, and drain. The source and drain terminals are called Ohmic contacts, have a linear current-voltage relationship in accordance with Ohm's law, and allow bidirectional current flow directly to and from the 2DEG. On the other hand, the gate terminal is called a Schottky contact and forms a rectifying electric potential barrier at the metal-semiconductor interface that is used to control the flow of electrons between the gate metal and the AlGaIn/GaN heterostructure. The drain-source voltage (V_{ds}) bias is used to control the driving potential that governs the flow of electrons through the 2DEG, the gate-source voltage (V_{gs}) bias is used to arrest current flow in the 2DEG to impose a pinched-OFF state, and the source terminal is used as a ground condition.

Typical AlGaIn/GaN HEMT devices are classified as “normally ON” and will immediately conduct electricity with a positive drain bias and an open gate bias ($V_{ds} > 0$ and $V_{gs} = 0$). The pinched-OFF state is achieved by applying a negative gate bias that is more negative than a threshold voltage that is typically between -2 and -3 V ($V_{gs} < V_{th} \approx -3$). Applying a negative gate bias effectively pulls electrons into the gate terminal thereby creating a local electric field or depletion region that interrupts (or “pinches off”) the flow of electrons in the 2DEG by forcing them into the GaN buffer layer. During RF operation, the drain and gate bias conditions are varied continuously along a load line in rapid cycles. An example of the drain current-voltage (I_{ds} - V_{ds}) characteristics of an AlGaIn/GaN HEMT device under RF operation along three classes of load lines that were measured during reliability testing reported in literature [7] are shown in Figure 5. The following section

presents a more thorough introduction to the predominant known stress effects in AlGaIn/GaN HEMTs.

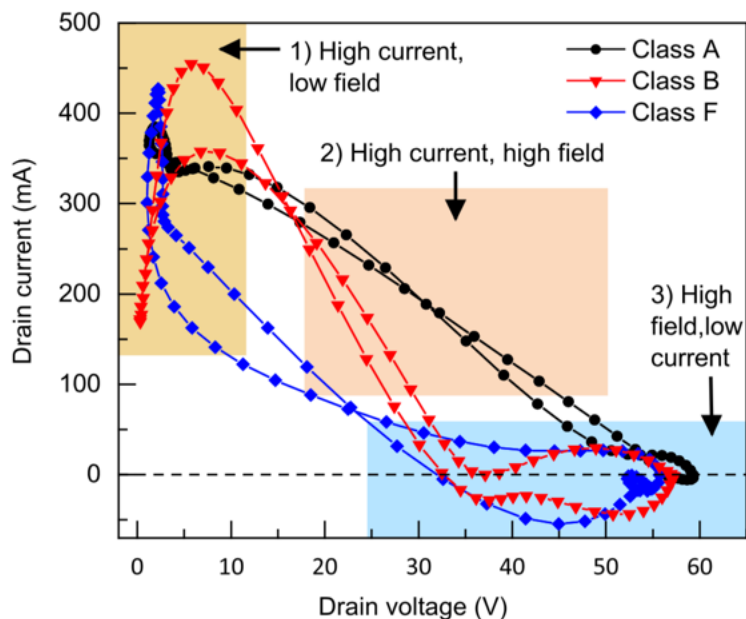


Figure 5. Representation of the most critical regions of degradation in the drain-source I-V characteristics during RF operation of an AlGaIn/GaN HEMT device along three different classes of load lines measured at the same output power of 35 dBm that has been reproduced from literature [7].

1.2.2 Reliability Challenges and Implications

According to the basic operating principles of AlGaIn/GaN HEMTs, the application of a positive drain bias during the ON and pinched-OFF states generates a localized electrical field near the AlGaIn/GaN interface and the drain-edge of the gate as shown in Figure 6. The localized high electric field causes electrons in the 2DEG to rapidly accelerate and gain extremely high kinetic energy. These highly energetic electrons, called “hot electrons,” primarily dissipate energy to the GaN lattice by emitting longitudinal optical (LO) phonons that in turn decay into transverse optical (TO) phonons and acoustic phonons [8]. Since the LO phonon decay time of ~ 350 fs is much greater than the LO

phonon emission (via hot electrons) time of ~ 10 fs, a localized accumulation of non-equilibrium LO phonons or hot phonons occurs near the peak electric field forming an effective bottleneck for energy transport. As a result, the complex cascade of phonon interactions results in a localized increase in lattice temperature or “hotspot” of approximately 10-100 nm in diameter forms near the peak electric field as illustrated in Figure 6. This highly concentrated self-heating (Joule heating) is the cause of the elevated operating temperatures of AlGaN/GaN HEMTs and is a critical contributor along with the highly concentrated electric field, to the numerous stress effects and reliability limitations present during high-power RF operation.

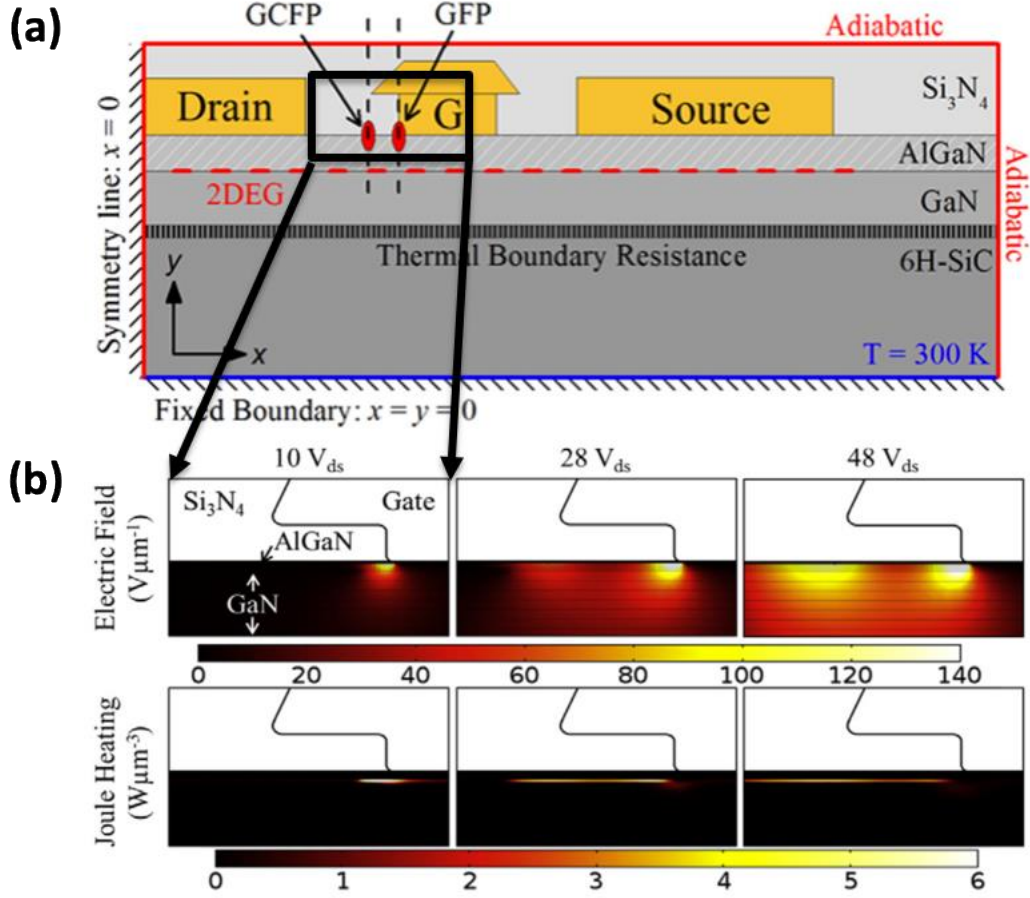


Figure 6. (a) Representative AlGaN/GaN HEMT device geometry with thermal and structural boundary conditions for an electro-thermo-mechanical FEM presented in literature [9]. The two labeled locations are the gate foot print (GFP), where high amounts of mechanical stress have been shown to develop, and the region directly below the gate-connected field plate (GCFP), where stress is typically probed optically via Raman spectroscopy. (b) Electro-thermal FEM results that show the electric field distribution (top row) and Joule heating (bottom row) near the drain-side of the gate. [9]

High-power RF operating conditions produce several competing stress effects that lead to various forms of device degradation. Although experimental characterization of these various stress effects have been studied extensively in literature [9-12], the underlying physical degradation mechanisms present during RF operation have yet to be fully understood. Electrical degradation has been characterized by measuring the onset of device gate leakage, loss of power added efficiency (PAE), current collapse, changes in

transconductance and gate current noise [11-14]. Physical degradation of the AlGaIn/GaN heterostructure near the drain-edge of the gate in the form of cracking or pitting, as illustrated in Figure 7, has been observed by high resolution transmission electron microscopy (TEM) as a result of high drain bias reliability testing [2, 15].

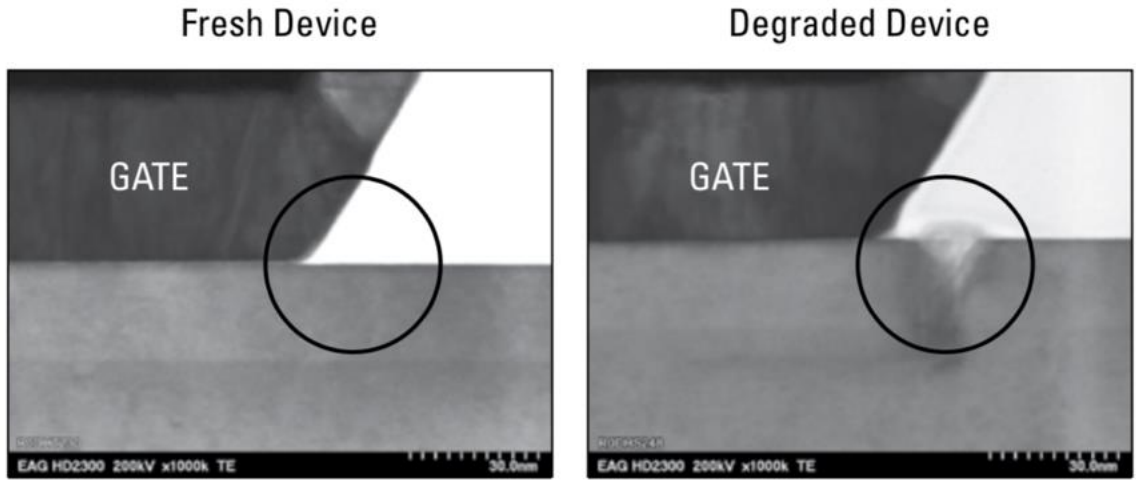


Figure 7. Mechanical degradation at the drain-edge of the gate of an AlGaIn/GaN HEMT [2].

To mechanically explain the acute physical degradation observed at the drain-edge of the gate, three classifications of stress effects have been described: operational inverse-piezoelectric (IPE), operational thermoelastic, and residual (independent of operation) stress effects [10, 16, 17]. Although Raman spectroscopy has been demonstrated capable of distinguishing operational thermoelastic stress by conducting measurements under a constant electric field [16], it is difficult to directly measure IPE stress effects near the drain-edge of the gate from RF HEMTs during high field conditions due to the restricted line of sight from the gate field plate and due to active device degradation during measurements [10]. Experimental investigation of AlGaIn/GaN HEMT degradation physics during RF operating conditions is also constrained by the limited temporal

resolution of present techniques. However, experimental Raman spectroscopy-derived residual stress results have demonstrated that substrate-induced residual stress (accumulated from wafer fabrication) in the AlGaIn/GaN heterostructure is a decisive contributor to device reliability under high bias conditions [10]. Moreover, transient electro-thermo-mechanical finite element modelling has revealed the presence of large tensile IPE and thermoelastic stresses near the drain-edge of the gate and a large stress gradient between the drain-edge of the gate and the edge of the gate field plate as shown in Figure 8 [9]. The highly concentrated tensile stress in the AlGaIn layer near the drain-edge of the gate demonstrated by the electro-thermo-mechanical FEM [9] compounded with highly tensile residual stresses near metallization patterns as measured in literature [18] are likely to increase the chance of mechanical degradation at the drain-edge of the gate as shown in Figure 7. Therefore, mitigating excessive residual tensile stresses accumulated in the AlGaIn/GaN heterostructure during GaN-on-substrate fabrication is critical for maximizing RF HEMT device reliability.

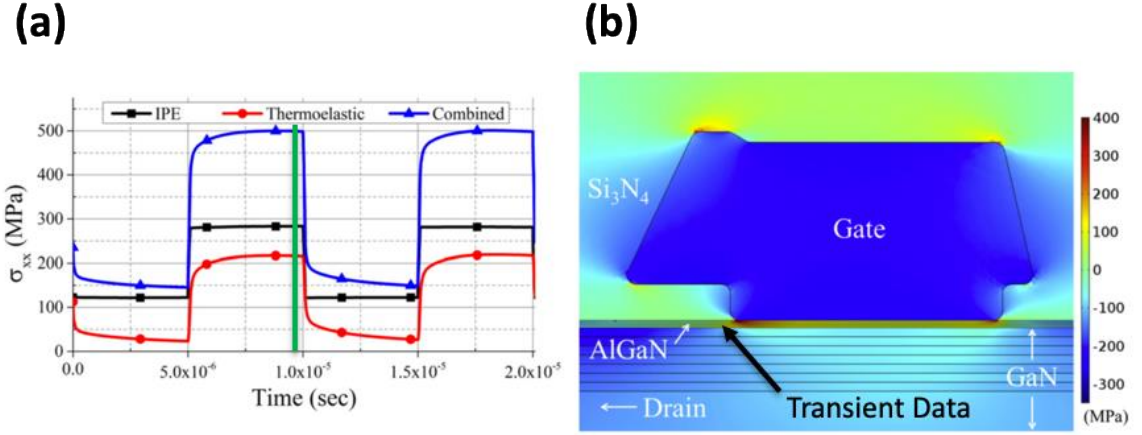


Figure 8. (a) Transient electro-thermo-mechanical FEM stress results reported in literature [9] from a 5×1 nm area within the AlGaN layer near the drain-side of the gate of AlGaN/GaN HEMT as depicted in (b). (b) 2D stress map before the end of the first ON state as indicated with the vertical line (green) in (a). [9]

1.3 Advanced Thermal Management Solutions

1.3.1 Diamond for Passive Heat Spreading

Over the years, AlGaN/GaN HEMT development has experienced tremendous growth and advancement [3, 19-21]. The more recent advancements in material growth, processing technologies, device architecture, and reliability testing have propelled AlGaN/GaN HEMTs to the forefront of high-power RF applications [3, 22]. However, despite the rapid maturation of electrical device performance, thermal management is the most prominent developmental bottleneck limiting device performance [23, 24]. Although the complex degradation mechanisms present during high-power and high-frequency operation of AlGaN/GaN HEMTs have yet to be fully understood [9], it is clear that excessive device self-heating is detrimental to device performance and reliability and can even lead to device catastrophic failure [25, 26].

Acute self-heating localized in the active channel region of RF HEMT devices is particularly problematic because the device architectures optimal for high frequency operation result in extreme, highly-localized power densities ($\sim 10^5$ W/cm²) [27]. Therefore, to combat the rapid and highly concentrated hot spot formation in such devices, it is critical to place the cooling solution as close to the heat source (AlGaIn/GaN heterojunction on the drain-side edge of the gate [9, 24]) as possible. It is primarily for this reason that SiC ($k_{SiC} \approx 380 - 450$ W/mK) is the dominant heteroepitaxial growth substrate material used by the RF GaN industry despite the high cost with respect to Si ($k_{Si} \approx 140$ W/mK) and sapphire ($k_{Sapphire} \approx 23$ W/mK) alternatives [28]. However, even with the 3x improvement over Si in thermal conductivity, RF power GaN-on-SiC HEMT devices are still limited by their intra-chip heat spreading capability and face severe limitations on power output and lifetime [29]. Therefore, to further enhance heat spreading near the heterojunction of AlGaIn/GaN HEMTs for high-power RF applications, chemical vapor deposited (CVD) diamond ($k_{diamond} \approx 2000$ W/mK) has been integrated to device epitaxial layers to leverage the proposed 5x improvement in thermal conductivity over SiC [29-31].

In recent efforts to assess the thermal performance benefits of GaN-on-diamond HEMT technology, experimental results produced by the Defense Advanced Research Project Agency (DARPA) Near Junction Thermal Transport (NJTT) program (2011-2014) have demonstrated a GaN-on-diamond HEMT device with a 2.7x reduction in thermal resistivity and a 3x increase in areal dissipation density as compared to a GaN-on-SiC HEMT device [32]. According to further investigation of the material and interface thermal properties of the reported GaN-on-diamond HEMT device performance, a relatively large TBR of 47.6 m²/GW measured at the GaN/diamond interface was determined to be the

most significant contributor to the device temperature rise [32]. Since the conclusion of the DARPA NJTT program, additional resources were dedicated in the form of another DARPA program for a deeper dive to understand (i) the merits of advanced measurement techniques for measuring the thermal properties of thin CVD diamond films and the thermal boundary resistance with its growth substrate, and (ii) the parameters that affect the variation of these thermal properties [33].

The experiments and analyses presented in this thesis were performed in support and as an extension of this DARPA Diamond Round Robin program [33] to characterize the thermal merit and structural feasibility of integrating polycrystalline diamond (PCD) to AlGaIn/GaN HEMT devices for superior thermal management. To accomplish this main objective, the following material and device characteristics have been evaluated:

- 1) The low in-plane thermal conductivity ($k_{||}$) of the highly disordered, near-interfacial nanocrystalline diamond (NCD) present in PCD directly grown on GaN;
- 2) The biaxial stress accumulated during the various GaN-on-diamond fabrication process alternatives;
- 3) The GaN/PCD thermal boundary resistance ($TBR_{GaN-PCD}$) resulting from the various GaN-on-diamond fabrication process alternatives; and
- 4) The operational AlGaIn/GaN power amplifier device self-heating resulting from implementing the various GaN-on-diamond fabrication process alternatives.

1.4 Research Overview

As discussed in Sections 1.1 and 1.3, the full potential of AlGaN/GaN HEMT devices is limited by excessively high junction temperatures caused by acute self-heating localized within the active channel regions. Since these transistor devices operate under cyclic conditions between an ON-state and an OFF-state, the rapid high-temperature thermal cycling induces a variety of complex degradation mechanisms that can eventually lead to device catastrophic failure. In order to achieve the high switching frequencies necessary for RF applications, HEMT devices must be designed with high local area density, a requirement that exacerbates the heat dissipation problem. Therefore, in order to dissipate the extreme, highly localized power densities up to $\sim 10^5$ W/m²K, CVD diamond ($k \sim 1400$ - 2000 W/mK) has been utilized as a substrate material alternative to Si ($k \sim 140$ W/mK) and SiC ($k \sim 380$ - 450 W/mK) to bring the cooling solution as close to the localized heat source as possible.

GaN-on-diamond wafers for HEMT devices can be fabricated in two ways: (i) epitaxially growing the AlGaN/GaN heterostructure on a single-crystal diamond substrate, or (ii) transferring a pre-grown AlGaN/GaN heterostructure to a polycrystalline diamond substrate. Due to the prohibitively high cost of single-crystal diamond substrates, the latter approach that utilizes polycrystalline diamond (PCD) is preferred. However, PCD growth begins from nano-sized diamond seeds that lead to degraded thermal properties within the first few microns of diamond crystal growth. Therefore, the combination of this low-thermal conductivity nanocrystalline diamond (NCD) and the highly resistive GaN-diamond interface have become the principal bottleneck for thermal transport away from the HEMT hot spot.

CHAPTER 2 presents two steady-state thermometry techniques that were used to measure the in-plane thermal conductivity of NCD thin films ($1 - 3 \mu\text{m}$) to understand the extent of thermal property degradation present in the initial microns of CVD polycrystalline diamond. The efficacy and practical limitations of using both TiO_2 particle-assisted Raman thermometry and electrical resistance thermometry to characterize the in-plane thermal conductivity of thin film materials such as NCD were established by developing a rigorous uncertainty analysis framework for such steady-state thermometry techniques. Once having validated the efficacy of both techniques, two comparative analyses were performed by measuring NCD thin film samples grown according to different growth conditions and thicknesses. The goal of these comparative analyses was to inform growth processes optimizing CVD growth methods for ideal thermal transport through the near-nucleation NCD of CVD polycrystalline diamond.

In CHAPTER 3, various samples of GaN-on-PCD wafers were examined using a stress metrology technique that utilizes Raman and photoluminescence (PL) spectroscopy to measure a through-thickness stress distribution within the GaN buffer layer of each GaN-on-diamond wafer sample. The GaN-on-PCD wafer samples were fabricated according to two alternative AlGaIn/GaN heterostructure transfer fabrication methods that all inherently lead to the development of a residual stress state throughout the GaN-on-PCD wafer. As discussed in Section 3.1, this residual stress state can degrade the material quality of the AlGaIn/GaN heterostructure and even lead to heterostructure fracture, conditions that are prohibitive of HEMT device functionality. Therefore, the goal of the comparative analyses of three-dimensional (3D) stress data measured from each GaN buffer layer was to identify the heterostructure transfer process alternatives that most effectively mitigate these residual

stresses to improve GaN-on-PCD material quality for the realization of commercially viable GaN-on-PCD HEMTs in high-power, high-frequency applications. Finally, the GaN-on-PCD fabrication process alternatives were compared by incorporating their effective thermal resistances into a comparative steady-state thermal finite element model (FEM) of an AlGaIn/GaN power amplifier. CHAPTER 4 summarizes the final conclusions of this work and proposes future work to further evaluate the reliability of GaN-on-PCD HEMT technology.

CHAPTER 2. THERMAL TRANSPORT IN PCD FILMS

2.1 Introduction

2.1.1 *Chemical Vapor Deposition*

Although diamonds are commonly acknowledged for their brilliant aesthetic appeal as gemstones, diamond as an engineering material has a remarkable range of outstanding physical properties. In its natural form, diamond is the hardest and stiffest known material, has the highest thermal conductivity at room temperature, is transparent over a wide range of wavelengths, and is inert to most chemical reagents [34]. However, naturally occurring diamond is practically useless for most engineering applications because of its high cost, scarcity, and limited form of stones and grit. Hence, over the past several decades a variety of techniques have been developed for growing different forms of synthetic diamond. One approach of diamond growth sought to reproduce the earth's natural processes via high-pressure and high-temperature (HPHT) and resulted in nanometer- and millimeter-sized single crystals that are commonly referred to as "industrial diamond" and used for cutting and machining applications [34]. However, to unlock the full potential of diamond's outstanding thermal and optoelectronic material properties, diamond must be grown in the form of a thin film.

Following a concurrent alternative approach to HPHT diamond growth, decades of research and experiments dedicated to understanding the reaction chemistry and kinetics of carbon-containing gas precursors localized above a solid deposition surface have led to the state-of-the-art implementations of diamond chemical vapor deposition (CVD). Although diamond CVD has been demonstrated using a number of different reactor varieties [34, 35], the diamond CVD process typically consists of the following features:

- 1) An abundant source of gas phase carbon-containing molecules (usually CH₄) diluted in excess of hydrogen (mixing ratio of ~1% vol. CH₄/H₂) in a low-pressure chamber (< 100 Torr);
- 2) A localized and energy-dense molecular excitation source used to activate precursor molecules thereby creating free radicals;
- 3) A deposition substrate heated to ~700 °C; and
- 4) Tunable reaction conditions, chemistry, and kinetics to enable growth process optimization and enhancement. [34]

Once the carbon-containing precursor molecules are activated to form highly reactive free radicals, a chain of localized reactions at the substrate surface cause carbon atoms to be chemisorbed onto the existing diamond crystal lattice [34]. This simplified process summary is illustrated in Figure 9. The process features that most clearly distinguish one diamond CVD method from another are (1) the molecular excitation source and (2) the deposition substrate material selection. The most common types diamond CVD techniques are shown in Figure 10 and have excitation sources that can be categorized as either thermal (hot filament) or electrical (microwave plasma) in nature. Depending on the specifications of the technique, the deposition substrate can either be an HPHT diamond crystal (homoepitaxial growth) or a non-diamond material such as silicon or molybdenum (heteroepitaxial growth). Additional details about the chemical and physical processes that govern the reaction kinetics of diamond CVD are beyond the scope of this work and can be found in literature [34].

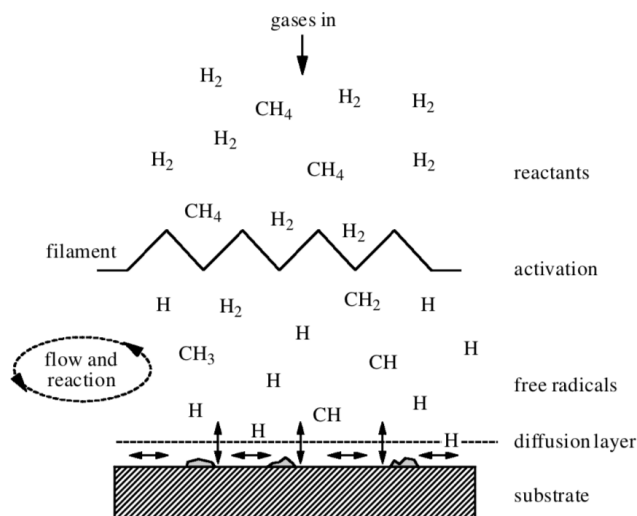


Figure 9. Schematic of the chemical and physical processes occurring during diamond CVD [34].

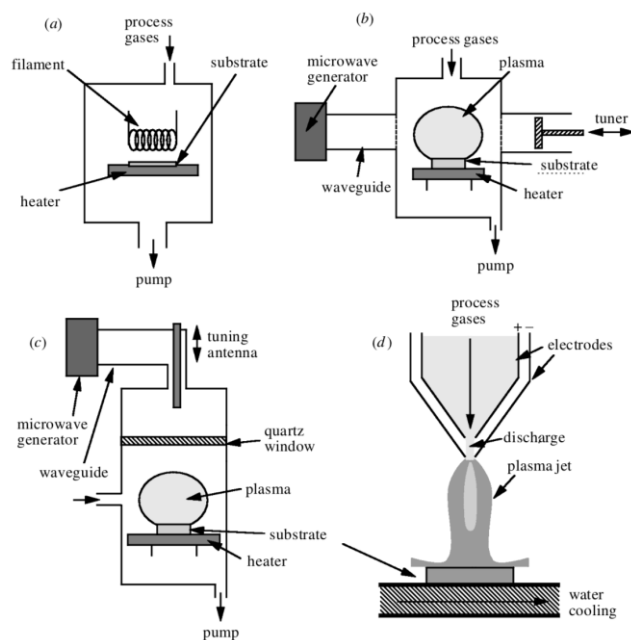


Figure 10. Examples of common types of diamond CVD reactor. (a) Hot filament, (b) “NIRIM-type” microwave plasma reactor [36], (c) “ASTEX-type” microwave plasma reactor [37], (d) DC arc jet (plasma torch). [34]

Hot filament CVD (HFCVD) is a relatively cheap and easy to use method that uses a metal (tungsten or tantalum) filament that is Joule-heated to temperatures exceeding 2200 °C to thermally excite precursor molecules and yields polycrystalline films of

reasonable quality at a rate of 1-10 $\mu\text{m/h}$. However, the extreme temperature of the hot filament leads to inevitable filament degradation that leads to diamond film contamination and constrains the maximum deposition time. Furthermore, the inherent thermal nature of the HFCVD process constrains process enhancement due to the limited variety of acceptable gas mixtures and limited population of reactive gas phase ions available for deposition-enhancing substrate biasing. [34]

Microwave plasma CVD (MWCVD) is a more expensive, yet more robust method that uses microwave power coupled into the reaction chamber via a dielectric window to create an electric discharge (plasma) that is localized at the substrate surface to create reactive species for diamond growth [34]. The absence of a destructible hot filament makes MWCVD processes inherently cleaner (less diamond contamination) than HFCVD. Further, MWCVD provides the most opportunity for tuning reaction conditions, chemistry, and kinetics by enabling higher excitation powers, wider diversity of gas mixtures (e.g. oxygen or nitrogen), and enhanced substrate biasing [34]. Hence, MWCVD is currently the most widely used method for diamond growth and has been demonstrated to be the most promising technology for reproducibly manufacturing single crystal with the size and structural quality required for application in ultrawide bandgap (UWBG) electronic and optoelectronic devices [4, 38].

Although the defect-free single crystal diamond (SCD) necessary for a variety of anticipated device applications [4] is currently driving the development of an assortment of homo- and heteroepitaxial growth methods [38], polycrystalline diamond (PCD) grown via heteroepitaxy has been shown to be sufficient for heat spreading and thermal management applications by demonstrating that PCD can achieve thermal conductivity

nearly equivalent to that of SCD [39]. However, these high PCD thermal conductivities are only possible in bulk, once significant layer thickness has been achieved. In contrast, thermal transport within the first few microns of PCD is dramatically reduced due to small grain size and the abundance of defects. Recent work [40] has shown that the presence of this nanocrystalline diamond (NCD) in the near-nucleation region of PCD significantly affects the thermal performance of HEMT devices. However, despite the less effective heat spreading, substantial peak operating temperature reduction is possible with sufficiently low GaN-diamond thermal boundary resistance [40]. Hence, the thermal management solutions presented and examined in this work demonstrate the compelling utility of PCD despite its growth and characterization challenges.

2.1.2 Thermal Characterization: Challenges and Motivation

The most prominent challenges involved in designing and demonstrating the effectiveness of an experimental technique and the accompanying analyses can be boiled down to two objectives: (1) establishing confidence in the measurement result and (2) bounding the practical limitations of the technique. The realization of these objectives is particularly important to achieve when measuring the temperature and thermal properties of micro- and nanoscale material systems. At these length scales, when the mean free paths of electrons and phonons become comparable to or larger than a material system's characteristic length, the electrical and thermal properties of solid materials can deviate from their bulk characteristics and experience any combination of inhomogeneity, anisotropy, sensitivity to crystallographic conditions, and other localized size effects. Further, temperature and thermal property measurement of micro- and nanoscale material systems often requires specific sample preparation, precise experimental setup, diligent

consideration of testing conditions, and complex analysis derived from any number of necessary assumptions. However, despite these practical challenges, several measurement techniques have been demonstrated to be capable of characterizing thermal transport in thin films with thicknesses on the order of 1 μm [41-46].

As one might expect, the most prominent of these techniques have been scrutinized by the technical community through publication and verification. For example, rigorous sensitivity and uncertainty analyses have been presented in literature to qualify optical techniques such as time domain thermorefectance (TDTR) [42, 45, 47] and frequency domain thermorefectance (FDTR) [44, 47]. In short, the efficacy of these optical techniques depends on precise electrical and optical configurations, physical vapor deposition of a metallization layer, and multi-parameter fitting to a multi-layer transient analytical solution to the heat equation. Alternative to these complex time- and frequency-dependent techniques, several implementations of a steady-state technique for measuring the thermal conductivity of suspended thin films have been presented in literature [41, 48-50]. The primary advantages of this steady-state technique [41] over transient alternatives for thermal conductivity characterization of thin films are that (i) thermal analysis is simplified excluding thermal diffusivity, and (ii) the technique is designed to distinguish the in-plane thermal conductivity of anisotropic thin films. However despite simplified analysis, similar implementations of this steady-state technique provide only limited uncertainty analysis and show substantial disagreement between reported in-plane thermal conductivities of near-identical samples [48-50]. Moreover, unlike the more established transient techniques, rigorous sensitivity and uncertainty analysis quantifying the limitations of this steady-state technique has not yet been demonstrated in literature.

Therefore, to demonstrate the efficacy and practical limitations of using steady-state thermometry techniques to characterize the in-plane thermal conductivity, k_{\parallel} , of thin film materials, we present the best practices and an explicit uncertainty analysis framework for resolving in-plane thermal conductivity via two independent steady-state thermometry techniques: Raman thermometry and electrical resistance thermometry (ERT). Further, we demonstrate the experimental conditions that permit the simplifying assumption of one-dimensional (1D) thermal conduction along the in-plane direction with minimal sacrifice to the accuracy of k_{\parallel} determination. We have validated our analysis methodology with experimental in-plane thermal conductivity results measured from highly disordered and anisotropic nanocrystalline diamond (NCD) thin films. In addition, two comparative analyses have been performed based on empirical in-plane thermal conductivity results measured from an assortment of six NCD suspended membrane samples. The goal of the comparative analyses is twofold: (i) to provide empirical evidence for directing CVD growth conditions modifications toward improving the structural quality and thermal properties of near-nucleation CVD diamond, and (ii) to determine thermal properties for the initial layer thicknesses of near-nucleation CVD diamond for applications in GaN-on-diamond high-power and high-frequency HEMT devices. Our experimental NCD thin film k_{\parallel} results have been compared to experimental results presented in literature that were measured from similar NCD thin films via spatially resolved TDTR [51] and particle-assisted Raman thermometry [52].

2.2 Sample Preparation and Design

Diamond growth begins by individual crystal nucleation from the NCD seeds until the crystals coalesce (within the first 20 nm of growth) into a continuous film with a

columnar grain structure that experiences an increasing lateral (in-plane) grain size [45]. Recent studies have shown that there is a strong correlation between the thickness dependent lateral grain size and the near-nucleation in-plane thermal conductivity of NCD thin films [45, 52]. Since the grain size evolution of NCD has been shown to largely depend on the microwave power density, substrate temperature, chamber pressure, and methane concentration during growth [53], the sets of samples measured and compared in this work were grown according to nearly identical growth conditions with the exception of the varied growth parameter of interest.

The NCD thin films examined in this work were grown to a thickness of 1 μm and 3 μm on 75 mm diameter and 200 μm thick silicon (Si) wafers via microwave plasma enhanced chemical vapor deposition (CVD). Prior to diamond growth, the silicon substrates were seeded with grain size homogeneous and chemically pure NCD powders for diamond crystal nucleation. Each diamond-on-Si wafer produced an array of 10 x 10 mm square die that were diced and processed into test structures that were specifically designed to test the accuracy and precision of performing in-plane thermal conductivity measurements using three techniques: Raman thermometry, electrical resistance thermometry (ERT), and time-domain thermoreflectance (TDTR), as shown in Figure 11. The test structures examined in this work are shown in Figure 12 and were located on the “common sample” die contained within the concentric circles depicted in Figure 11 that denote the wafer periphery. As shown in Figure 12, two membrane samples, denoted “a” and “b”, were contained on each common sample die along with two different test structures that were peripheral to this work. The fundamentals and experimental details of the former two techniques are presented in subsequent sections, however those of the latter

are beyond the scope of this work and have been reported in literature [45, 51] and presented in conference proceedings [54].

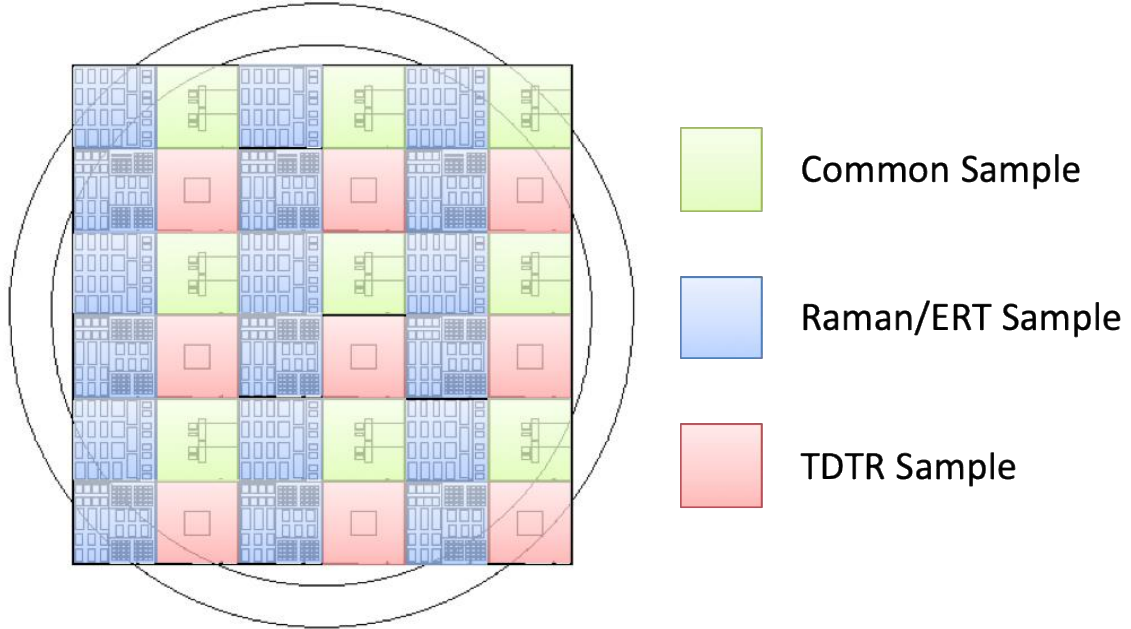


Figure 11. Schematic of the global coordinate system used to identify NCD samples distributed amongst the participating members of the DARPA Round Robin Program [33]. The concentric circles denote the wafer periphery. The outer circle indicates the wafer perimeter and the inner circle indicates the region of the wafer with uniform NCD film thickness. NCD film thickness non-uniformity within the inner circle was measured to be less than 1 % [49].

In-plane thermal conductivity measurement results from a total of six samples obtained using particle-assisted Raman thermometry and ERT are presented in this work. All samples taken from wafers 1 and 2 were grown according to similar growth conditions (2200 – 2300 W microwave power and 750 °C growth chamber temperature) to a thickness of 1 μm . However, samples 1a and 1b were grown from 4 nm nucleation seeds and samples 2a and 2b were grown from 40 nm nucleation seeds. Samples taken from wafers 3 and 4 were grown according to similar growth conditions (1400 W microwave power and 750

°C chamber temperature) to thicknesses of 1 and 3 μm , respectively. The thermal conductivity results for each sample are shown in Table 2.

Each sample was an NCD suspended membrane formed by back-etching a 400 x 2000 μm area of silicon substrate as depicted in Figure 12. To supply a controllable heat source and enable electrical measurements, 5 μm wide metal lines and contact pads were patterned onto the NCD films by depositing a 10 nm thick titanium (Ti) adhesion layer followed by 200 nm of gold (Au). Additionally, a thin film of aluminum (Al) measuring 90 nm in thickness was deposited on the backside of all the suspended membrane samples except sample 3 as a byproduct of a preprocessing step for the aforementioned TDTR measurements (not reported in our work) conducted on a neighboring suspended membrane. The metal center line was used as a resistive heater (Joule heating) to dissipate heat laterally (x-direction) to produce one-dimensional (1D) thermal conduction at the longitudinal (y-direction) center of the membrane and hence a linear temperature profile spanning the membrane width (see Figure 12). It is important to note that the 1D condition (non-negligible heat transfer in only the x-direction) is preserved by maintaining an isothermal condition along the membrane length (y-direction) and across the membrane thickness (z-direction). Parametric analysis using the representative finite element model described in Section 2.3.3 that has considered various suspended membrane dimensions (see Figure 22) demonstrates that the 1D condition holds in the center of the suspended membrane for the length-to-width aspect ratio of 5 selected for our suspended membrane design. For the dimensions of our samples (400 x 2000 μm), this 1D region shown in Figure 12 spans the full width of the membrane and is bounded in the y-direction by $\pm 250 \mu\text{m}$.

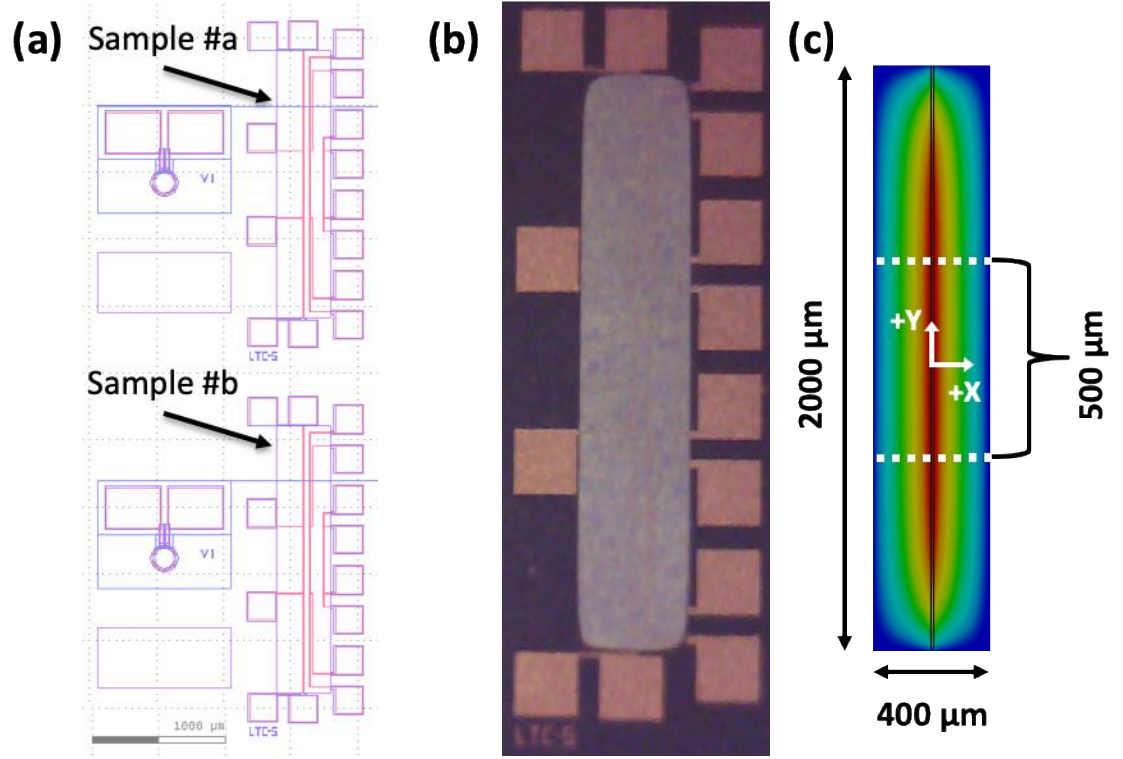


Figure 12. NCD suspended membrane sample (a) design, (b) microscope image, and (c) schematic taken from the FEM. The nominal dimensions of the suspended membrane perimeter and 1D region are shown.

2.3 Methodology for In-Plane Thermal Conductivity Characterization

Two independent steady-state thermometry techniques, particle-assisted Raman thermometry and electrical resistance thermometry (ERT), were used to measure the in-plane thermal conductivities of nanocrystalline diamond (NCD) suspended membrane samples fabricated according to two varieties of growth conditions. In order to distinguish an appreciable difference between the thermal conductivities of the two groups of samples, the measurement techniques and accompanying analyses must be capable of resolving thermal conductivity results within a reasonable measure of uncertainty, typically $\pm 10\%$. Accomplishing this task experimentally, however, proves difficult and requires careful consideration of physical conditions and model assumptions. Hence, we demonstrate the

efficacy of accurately resolving the in-plane thermal conductivity ($k_{||}$) of our NCD suspended membrane samples via particle-assisted Raman thermometry and ERT by introducing a steady-state heat source, physically confining thermal transport to the in-plane dimension, measuring the imposed temperature distribution, and fitting the experimental results to a numerical finite element model (FEM) as illustrated in Figure 13. The experimental setups for the particle-assisted Raman thermometry and ERT techniques are shown in Figure 14.

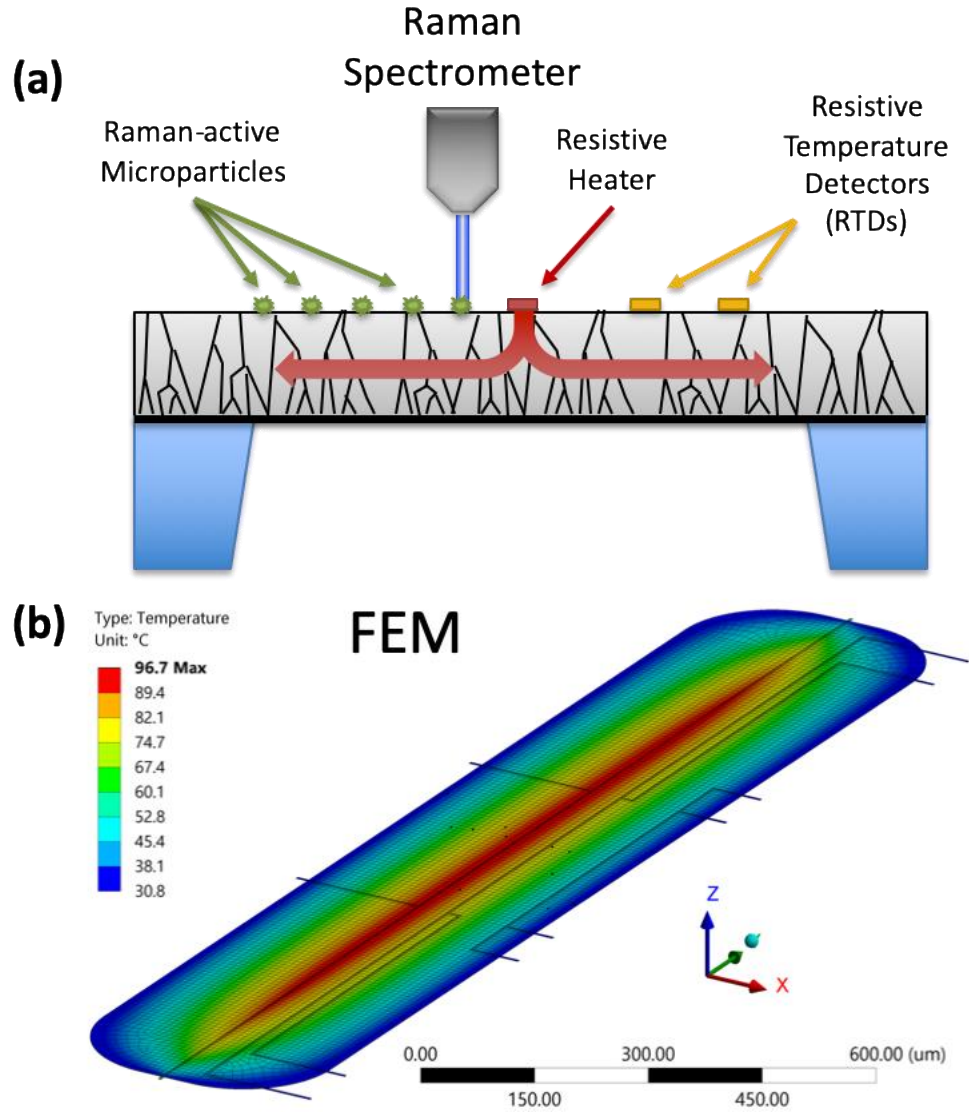
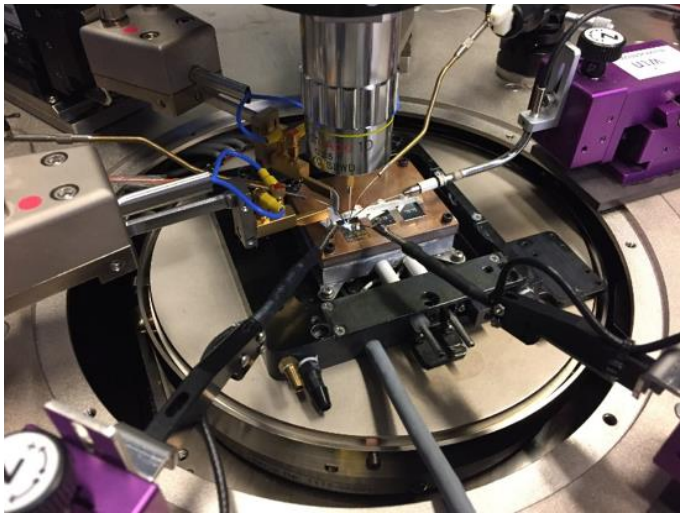
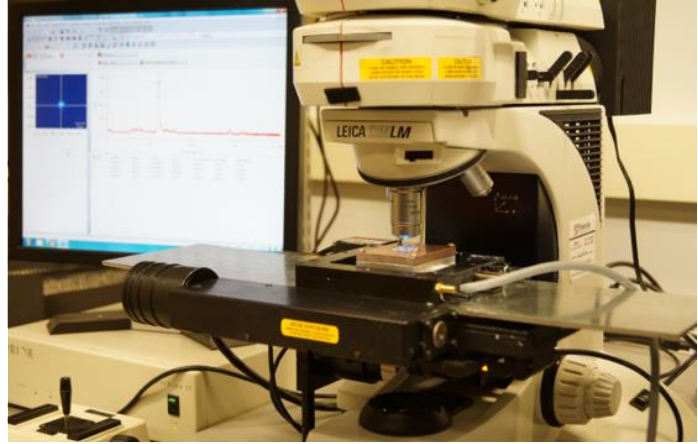


Figure 13. (a) Schematic of the steady-state thermometry techniques, particle-assisted Raman thermometry and electrical resistance thermometry (ERT), used to measure the suspended nanocrystalline diamond (NCD) membrane samples, and (b) the finite element model (FEM) used to extract the NCD in-plane thermal conductivity.

Particle-Assisted Raman Thermometry



Electrical Resistance Thermometry (ERT)

Figure 14. Experimental setups for the particle-assisted Raman thermometry and electrical resistance thermometry (ERT) techniques.

2.3.1 *Particle-Assisted Raman Thermometry*

Raman thermometry was used to measure the temperature distribution present across the NCD membrane samples when electrical power was supplied to the centerline resistive heater. Generally speaking, Raman thermometry is the application of Raman spectroscopy to perform high resolution ($\sim 3^\circ\text{C}$ and $\sim 1\ \mu\text{m}$ respectively) *in situ* temperature measurements. Raman spectroscopy is an extremely well established [5, 55, 56] optical characterization technique that, in brief, uses a monochromatic laser to probe the

vibrational energies of a material's molecular structure. When used to characterize semiconductors, the specific nature of the sampled vibrational spectrum, commonly referred to as the Raman spectrum, can be used to examine a wide variety of material properties including but not limited to crystal orientation, chemical composition, mechanical strain, and lattice temperature.

Literature [57] presents a comprehensive summary of the methods commonly used to perform Raman thermometry, i.e., correlate the Raman spectrum to lattice temperature, and compares the advantages and challenges inherent to each method. Each method examines one of three features of Raman spectrum peaks: intensity, linewidth or full width at half maximum (FWHM), or peak position. We elected to use the peak position method for Raman thermometry because of its intrinsic nature (insensitivity to spectrometer and laboratory conditions) and linear calibration relation. However, despite the experimental practicality of the peak position method, the Raman peak position, ω , is a measure of the frequency of molecular lattice vibrations, i.e., phonon frequency, and is therefore particularly sensitive to nonthermal biasing. For example, as a material experiences local or self-heating, the interatomic forces are typically altered by a combination of effects: (1) volumetric expansion that accompanies the increasing lattice temperature, and (2) thermoelastically induced strain. Since the frequency of molecular vibrations indiscriminately depends on the interatomic forces, a measure of peak position shift with respect to a reference condition, $\omega - \omega_0$, contains a combination of temperature and thermomechanical stress information. According to the conclusions of numerical error analysis presented in literature [58], thermomechanical induced errors in temperature measurements can invalidate thermal conductivity deductions through error propagation.

However, due to the material-specific nature of Raman thermometry, it is possible to altogether avoid thermomechanical signal biasing by probing the temperature of surface-deposited particles. Raman thermometry of surface-deposited temperature sensors has been demonstrated in literature using a variety of temperature sensor materials including diamond microparticles [59], silicon nanowires [41], titanium dioxide (TiO_2) [60], and hexagonal boron nitride (hBN) [50]. To identify the most suitable temperature sensor, it is paramount to consider the peak positions and relative intensities of the temperature sensor and suspended membrane Raman spectra. The Raman peaks of interest native to the membrane and temperature sensor materials should be clearly distinguished from one another by having disparate peak positions and sufficient signal-to-noise ratios. Consequently, diamond nanoparticles and silicon nanowires were inappropriate temperature sensors for our experiments characterizing CVD diamond grown on silicon substrates due to Raman peak superposition. Further, as illustrated in Figure 15, hBN was also ill-suited for our experiments due to the poor signal-to-noise ratio caused by the large diamond fluorescence background concomitant with our visible laser excitation (488 nm). It is of note that the poor Raman peak signal-to-noise ratio of hBN nanoparticles deposited on CVD diamond observed in our work can be resolved by performing the Raman thermometry using a near-UV (363.8 nm) excitation laser [50]. Therefore, TiO_2 particles were used as surface-deposited temperature sensors for Raman thermometry in our work. The TiO_2 particles were deposited onto the NCD suspended membrane samples by drop casting a suspension of a TiO_2 nanopowder (anatase phase, 99.9% purity and 32 nm average particle size) in isopropyl alcohol while maintaining a sample temperature of 85 °C (just above the boiling point of isopropyl alcohol) to accelerate evaporation.

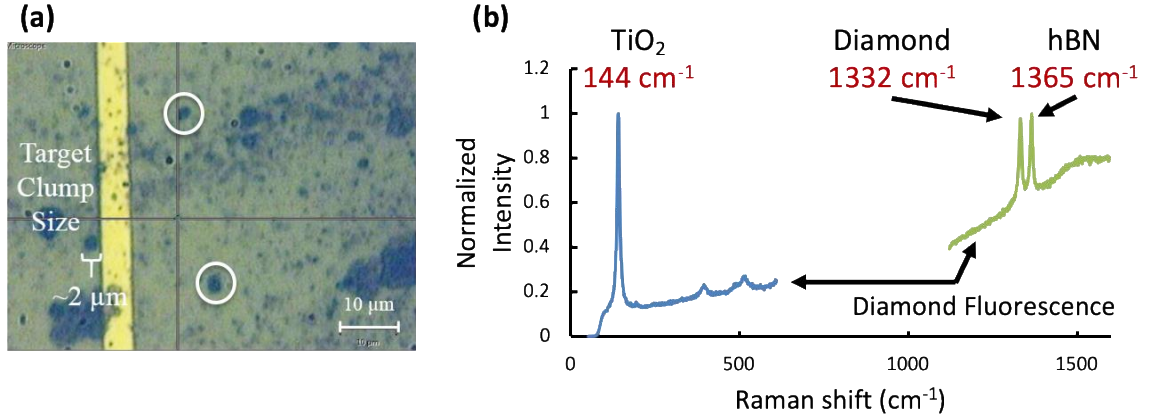


Figure 15. (a) Microscope image of TiO₂ nanoparticle aggregates. (b) Measured Raman spectra of TiO₂ and hBN particles deposited on NCD suspended membranes.

Hence, the surface-deposited TiO₂ nanoparticle aggregates (referred to as particles for simplicity) measuring between 1-2 μm in diameter and located within the 1D region were used as local temperature sensors for measuring the temperature distribution across the NCD membranes. Particles ideal for measurement are depicted in Figure 15. Two Keithley 2400 source meters were used to supply electrical power to and measure the resistance of the centerline heater, respectively. The contact resistances between the heater contact pads and the needle probes were nullified by making electrical measurements with a 4-point probe technique. The Raman thermometry measurements were collected using a Renishaw InVia Raman system with a 488 nm Ar⁺ excitation laser that was focused through a Leica 0.75 NA 100x objective to resolve a 0.79 μm theoretical diffraction limited laser focused spot size.

The temperature dependence of the strongest TiO₂ phonon mode frequency at 143 cm⁻¹ [61] was calibrated by measuring the Raman peak shift of a TiO₂ particle at a series of sample base temperature increments. For clarity, a single particle was measured throughout the full sequence of temperature increments by manually repositioning the XYZ

positioning stage to bring the target particle into focus between temperature increments. The resolution of the XYZ positioning stage was 0.1 μm in each direction, the accuracy of the stage mapping was calibrated using a Dual Axis Linear Scale Micrometer, and the stage mapping precision was measured to be 0.4 μm by calculating the 95% confidence interval of the statistical variation of the stage mapping calibration that was repeated 20 times. The sample base temperature was incremented from the reference condition (heater operation set point) of 30 $^{\circ}\text{C}$ to a maximum temperature of 150 $^{\circ}\text{C}$ using an INSTEC mk1000 thermal stage and temperature controller. A K-type thermocouple was securely mounted with thermal paste on the surface of the copper thermal stage and measured with a Fluke 54IIB Thermometer to obtain an accurate measure of the sample base temperature during calibration. For the temperature range of 30 – 150 $^{\circ}\text{C}$, the TiO_2 Raman peak shift dependence on temperature rise is linear and is quantified as a linear calibration coefficient, A_{Ti} with units $\text{cm}^{-1}/^{\circ}\text{C}$, according to

$$A_{Ti} = \frac{\omega - \omega_o}{T - T_o} \quad (2)$$

where ω and ω_o are the Raman peak positions measured at the incremented and reference condition thermal stage temperatures, respectively, and T and T_o are the incremented and reference condition sample base temperatures, respectively, as measured by the thermocouple. To ensure that A_{Ti} did not vary from particle to particle, calibrations were performed on particles deposited on several suspended membrane samples. Further, to ensure that calibrations were not subject to any systemic error resulting from particle measurement on a suspended membrane, a calibration was performed with a particle

deposited on a silicon carbide wafer fragment. The results of these five calibrations yielded an average value of $A_{Ti} = 0.0251 \pm 0.0009 \text{ cm}^{-1}/^{\circ}\text{C}$ that is in precise agreement with the literature value of $0.0245 \pm 0.0008 \text{ cm}^{-1}/^{\circ}\text{C}$ measured from anatase TiO_2 nanocrystals [61]. Further, the agreement between the measured calibrations confirm that A_{Ti} is independent of particle selection (among $\sim 1\text{-}2 \text{ }\mu\text{m}$ nanoparticle aggregates) and the deposition substrate.

The experiment for determining the in-plane thermal conductivity, $k_{||}$, of each suspended membrane sample was performed by holding the thermal stage at a 30°C reference condition, sourcing 200 mW of electrical power to the centerline heater and collecting Raman thermometry measurements from TiO_2 particles spanning the membrane width. Measured temperature, T_m , was calculated by evaluating Equation 2 where A_{Ti} , ω , ω_o , and T_o are now the known quantities. Each Raman thermometry measurement was comprised of 60 Raman spectrum acquisitions: 20 acquisitions at the reference condition *before* the power condition, 20 acquisitions *during* the power condition, and 20 acquisitions at the reference condition *after* the power condition. All of the acquired spectra were fit to a pseudo-Voigt function (linear combination of Gaussian-Lorentzian functions) to extract the peak position, intensity, and FWHM of each spectrum peak. In addition to the Raman thermometry measurements collected from the surface-deposited TiO_2 particles, a Raman thermometry measurement was collected from the silicon substrate on either side of the centerline heater. Direct measurement of the silicon substrate was possible because the excitation laser used (488 nm) transmits through the TiO_2 particles and NCD membrane due to their wide bandgaps [62, 63], and is absorbed by the silicon substrate with a shallow penetration depth of $\sim 0.5 \text{ }\mu\text{m}$ [56]. These auxiliary measurements of the silicon substrate

are useful for detecting any local temperature rise in the silicon substrate that is otherwise undetected by the thermocouple mounted on the surface of the thermal stage.

2.3.2 *Electrical Resistance Thermometry*

Electrical resistance thermometry (ERT) is a commonly used electro-thermal technique for measuring the temperature of an electrically conductive feature by probing the change in its electrical resistance with respect to a reference condition. This technique is capable of low uncertainty and high-resolution temperature measurements when the resistance temperature detector (RTD) is a metal with a linear resistance-temperature correlation within the temperature range of interest. Hence, ERT techniques are particularly useful when a metallic feature is used as a resistive heater (Joule heating) because the heater can be simultaneously used as an RTD. A well-established implementation of ERT that leverages this heater/sensor duality to measure the thermal conductivity of thin film materials is the 3-omega (3ω) technique [64]. While the differential 3ω technique (an extension of the traditional implementation) is appropriate for measuring the isotropic and low-magnitude ($k < 1$ W/mK) thermal conductivity of dielectric thin films, resolving the in-plane and high-magnitude ($k > 10$ W/mK) thermal conductivity of a thin film can be subject to high uncertainty ($\delta k > 25\%$) and requires careful consideration of limiting assumptions [43]. Therefore, to enable accurate characterization of our high thermal conductivity ($k > 10$ W/mK) NCD films, a direct current (DC) implementation of ERT is demonstrated in this work.

Alternative to Raman thermometry, (ERT) was used to measure the temperature distribution present when electrical power was supplied to the centerline resistive heater

by using the centerline heater and two off-center metal lines as RTDs. The off-center RTDs were present on the membrane samples to accommodate two independent measurements at lateral distances (positive x-direction) of 50 μm and 150 μm from the centerline heater (see Figure 16). A Keithley 2400 source meter was used to supply electrical power to the centerline heater and an Agilent 34410A 6 $\frac{1}{2}$ Digit Multimeter was used to measure the resistances of the off-center RTDs. All of the electrical measurements were collected via a 4-point probe technique (to mitigate contact resistances) on a Cascade Microtech Summit 11000 probe station. A total of eight needle probes were used for the ERT experiments; four probes connected to the Keithley source meter and dedicated to the centerline heater, and four probes connected to the Agilent Multimeter and dedicated to the two off-center RTDs.

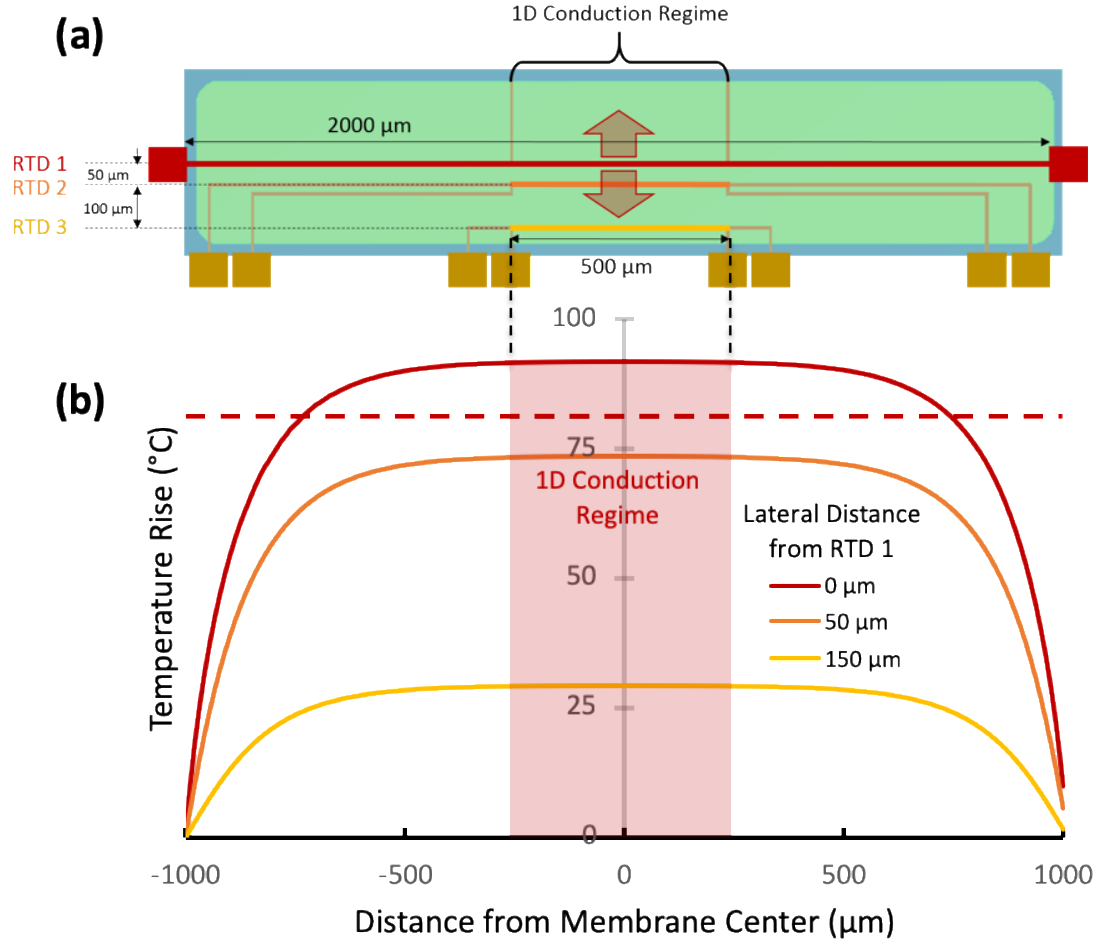


Figure 16. (a) Schematic of the NCD suspended membrane samples with dimensions of the metal lines used as RTDs. (b) Temperature rise along the length of the NCD suspended membrane calculated according to the FEM. Notice that the temperature rise measured from RTD 1 (dashed) is averaged across the entire membrane length and therefore is less than the isothermal maximum temperature present within the 1D Conduction Regime.

The procedure for calibrating the temperature dependence of the centerline heater and off-center RTD resistances was nearly the same as that described in Section 2.3.1 for calibrating the temperature dependence of the TiO_2 phonon mode frequency. The only difference between the procedures was the nature of the temperature sensor measurement, i.e. a resistance measurement of each RTD and a Raman measurement of a TiO_2 particle. For the temperature range of 30 – 150 $^{\circ}\text{C}$, the linear calibration coefficient of each RTD (centerline and off-center alike), A_R with units $^{\circ}\text{C}^{-1}$, was determined according to

$$A_R = \frac{\frac{R - R_o}{R_o}}{T - T_o} \quad (3)$$

where R and R_o are the resistances measured at the incremented and reference condition thermal stage temperatures, respectively, and T and T_o are the incremented and reference condition sample base temperatures, respectively, as measured by the thermocouple. It is significant to note that A_R for each RTD was evaluated as a *percent* change normalized by the resistance (RTD-specific) at the reference condition so that A_R is an intrinsic property calibration independent of the magnitude of the resistance (i.e. independent of the length of the RTD).

The experiment for determining $k_{||}$ of each suspended membrane sample via ERT was performed by using the same reference (30 °C) and power (200 mW) conditions as were used in the Raman thermometry experiment and measuring the resistances from each RTD. Measured temperature, T_m , was calculated by evaluating Equation 3 where A_R , R , R_o , and T_o are now the known quantities. The ERT measurements from all three RTDs were collected in dramatically less time than the Raman thermometry measurements from all of sampled TiO₂ particles. This reduction in measurement time was possible via ERT because (i) electrical measurements are nearly instantaneous whereas Raman measurements typically require between 1 – 20 seconds of acquisition time per spectral acquisition (20 spectral acquisitions per Raman measurement), and (ii) all of the RTDs could be measured nearly simultaneously during each reference condition (before and after the power condition) and during the power condition. The time-efficiency of these ERT measurements enabled experiments testing an array of power conditions. By extracting the

average membrane temperature for each power condition from the finite element model, the temperature dependence of $k_{||}$ was determined for membrane-averaged temperatures ranging between 35 – 70 °C and is presented in Section 2.5 (see Figure 21).

When performing ERT measurements in this configuration that sources electrical power across a linear heater geometry to approximate a constant heat flux condition, it is important to acknowledge the non-uniform temperature distribution present across the length of the centerline heater during the power condition. As reported in literature by a similar ERT [65] and otherwise demonstrated with our finite element model, the constant heat flux applied by the centerline heater during the power condition of our experiments creates a parabolic-like temperature profile across the suspended membrane that features a nearly isothermal plateau that determines the previously described 1D region (see Figure 16). Unlike the centerline heater, the off-center RTDs do not generate their own heat, are located within the 1D region, and therefore are uniform in temperature. However, the non-uniform temperature distribution across the centerline heater during the power condition is distinctly different from the uniform temperature achieved via global sample heating during calibration. This discrepancy practically means that the temperature measurement resolved from the centerline heater (RTD 1) is a weighted average that understates the temperature of the centerline heater present within the 1D region. Although the temperature measured from RTD 1 can be reasonably incorporated into a model-fitting routine for determining $k_{||}$ by sampling an equivalent RTD-averaged value from a thermal model, this approximation is subject to errors due to the approximation of Joule-heating inherent to a thermal model. To more accurately incorporate temperature measurements from RTD 1, a coupled electro-thermal FEM should be used to properly represent temperature dependent

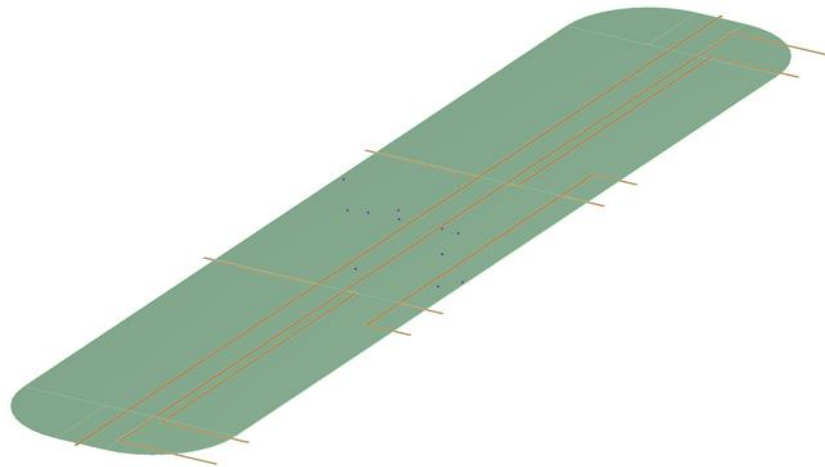
Joule-heating. Alternatively, an additional 4-point probe measurement can be used to measure the isothermal temperature of RTD 1 within the 1D region.

2.3.3 Steady-State Thermal Finite Element Model

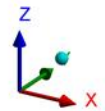
Since thermal conductivity is an intrinsic material property that is unable to be directly measured, a representative model must generate a theoretical temperature distribution that is a function of thermal conductivity to be used for direct comparison to our experimental Raman thermometry and ERT temperature measurements. Our theoretical model of the suspended membrane samples was a three-dimensional (3D) steady-state thermal finite element model (FEM) implemented in ANSYS. To ensure that the FEM approximation of each membrane geometry included any microfabrication imperfections, the membrane dimensions of each sample were verified via optical microscope images. To ensure the accuracy of the FEM, a standard mesh convergence analysis was performed that features local mesh refinement throughout the 1D region of the suspended membrane and achieved convergence ($< 1\%$ relative error) to a mesh-independent solution composed of nearly 300,000 quadratic elements. The FEM geometry and thermal results of sample 2a are shown in Figure 17.

Geometry

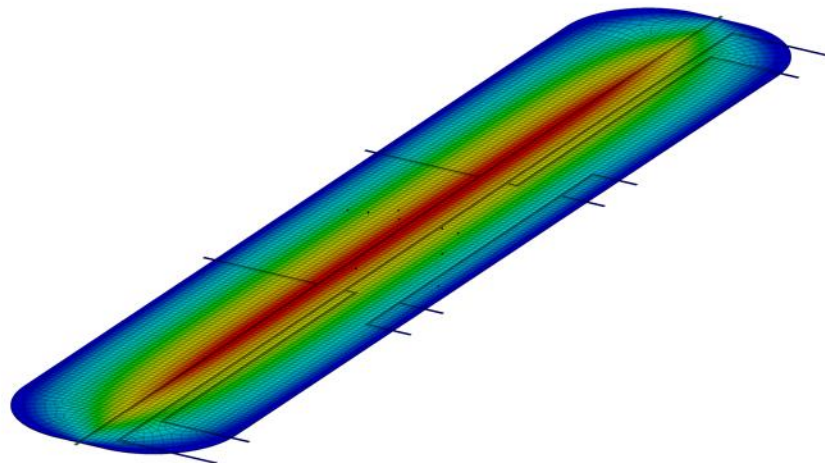
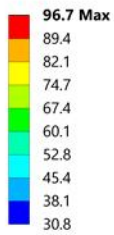
- CVD Diamond
- Gold
- TiO₂



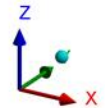
(a)



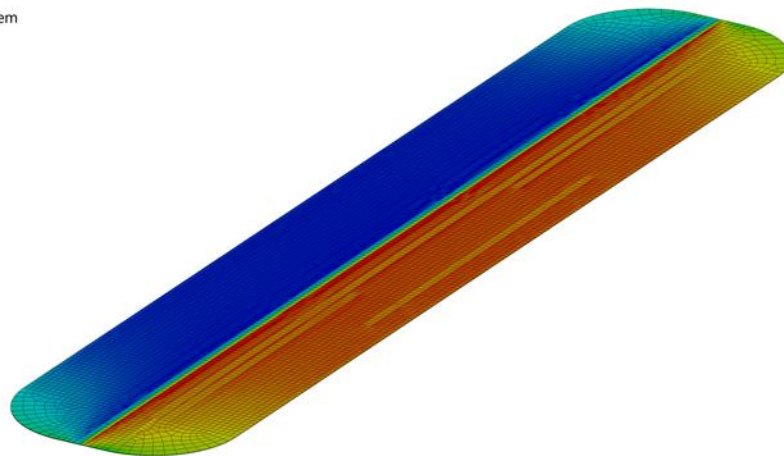
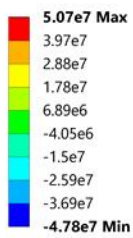
Temperature
Type: Temperature
Unit: °C
Time: 1
Custom Obsolete



(b)



Directional Heat Flux X Membrane
Type: Directional Heat Flux(X Axis)
Unit: pW/μm²
Global Coordinate System
Time: 1



(c)

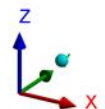


Figure 17. Finite element model (FEM) (a) geometry, (b) temperature map, and (c) x-directional heat flux map of an NCD suspended membrane sample (Sample B). The substrate and substrate-supported NCD film are not shown for visual clarity.

Temperature dependent thermal conductivities from literature were assumed for the silicon substrate [66], gold heater and RTDs [67], and aluminum thin films [67]. The thermal conductivity of the TiO_2 particles was assumed to be 0.51 W/mK [68] and literature has confirmed via Raman thermometry experiments that the contact resistance between surface-deposited temperature sensors and the underlying surface of interest is not relevant for steady-state measurements (timescales $> 10 \mu\text{s}$) [59]. The NCD films were assumed to be temperature independent and anisotropic with an anisotropy ratio, $\eta = k_{\perp}/k_{\parallel}$ of 2.8 [45] for the temperature range of 30 – 150 °C relevant to our experiments. The validity of the assumption of NCD thermal conductivity temperature independence is discussed in further detail in Section 2.4.4. The thermal boundary conductances (G) between the heater/RTD metal lines, NCD film, silicon substrate, and membrane-backside aluminum film were all measured via TDTR by Luke Yates and Zhe Cheng and are reported in Section 2.4.3 (see Table 1).

Due to the steady-state nature Raman thermometry and ERT techniques, careful consideration was given to the convective and radiative boundary condition assumptions. The convective boundary conditions at the upper surface of the NCD membrane and the heater/RTD metal lines were approximated by free convection above a hot flat plate in ambient air (22 °C). The convective boundary condition beneath the suspended membrane was approximated by free convection enclosed in a rectangular cavity heated from above that reduces to pure conduction through air due to the absence of advection. The theoretical formulations used to quantify convective heat transfer coefficients according to these

assumptions can readily be found in literature [67]. The radiative boundary conditions applied to the surfaces above and beneath the NCD membrane and the heater/RTD metal lines are approximated as diffuse, gray surfaces with an emissivity, ε , of 0.02 that is consistent with literature for NCD [69], and metallic thin films [70]. Convective and radiative losses from the TiO_2 particles were assumed to be negligible due their miniscule surface area.

2.4 Uncertainty and Error Analysis

To ensure a rigorous estimation of uncertainty in thermal conductivity, we have considered uncertainty contributions from (i) measures of accuracy, precision, and resolution of our empirical temperature measurements, and (ii) uncertainties of all auxiliary thermal and material properties determined for input to the representative FEM. We have propagated each of these primary sources of uncertainty to estimate the total in-plane thermal conductivity uncertainty by a combination of three uncertainty propagation methods: (i) Monte Carlo simulation (ii) analytical derivation, and (iii) sensitivity analysis. Analytical derivation was used to quantify temperature measurement uncertainties that were then propagated into an empirical in-plane thermal conductivity uncertainty estimation via Monte Carlo simulation. Sensitivity analysis of the FEM was performed to propagate the auxiliary FEM input parameter (geometry variables, interface conductances, etc.) uncertainties into a computational in-plane thermal conductivity uncertainty estimation. The overall in-plane thermal conductivity uncertainty, δk_{\parallel} , was estimated by combining the empirical and computational uncertainties via summation in quadrature according to

$$\delta k_{\parallel} = \sqrt{(\delta k_{\parallel}^{MC})^2 + (\delta k_{\parallel}^S)^2} \quad (4)$$

where $\delta k_{\parallel}^{MC}$ is the empirical Monte Carlo-based uncertainty in k_{\parallel} and δk_{\parallel}^S is the computational sensitivity-based uncertainty in k_{\parallel} . Furthermore, we have established an error-based criterion to determine the limiting experimental conditions that permit the simplifying assumption of 1D thermal conduction to drastically reduce the post-measurement analysis necessary for deducing k_{\parallel} .

2.4.1 Uncertainty: Monte Carlo Simulation

In order to deduce an empirical k_{\parallel} for the NCD suspended membrane, we must determine the theoretical (FEM input) NCD k_{\parallel} that yields a computed temperature distribution that best fits our experimental temperature data. We accomplished this parametric optimization through a Monte Carlo simulation executed in MATLAB. Monte Carlo (MC) simulation is an iterative stochastic method for solving optimization problems that is particularly useful for estimating the uncertainty of one or more unknown fitting parameters without knowing how experimental uncertainties will propagate nor how individual input uncertainties may be intercorrelated [71]. Although the full utility of MC simulation can be realized for solving multi-parameter optimization problems that fit experimental data to an analytical model such as those arising from thermoreflectance measurements [47], MC simulation is still advantageous for our single parameter fitting of k_{\parallel} because there exists no analytical means of propagating experimental temperature measurement uncertainties through an inherently numerical FEM. As illustrated in , our MC simulation propagated experimental temperature uncertainties into a MC-based

uncertainty of $k_{||}$, denoted as $\delta k_{||}^{MC}$, by assuming each experimental temperature measurement was normally distributed about its measured value according to its uncertainty, δT , and repeatedly fitting randomly sampled experimental data sets to FEM temperature solutions. The histogram of fitted $k_{||}$ results was then fit to a normal distribution from which the mean and 95% confidence interval were extracted to be the best-fit $k_{||}$ and its MC-based uncertainty ($k_{||}^{MC}$).

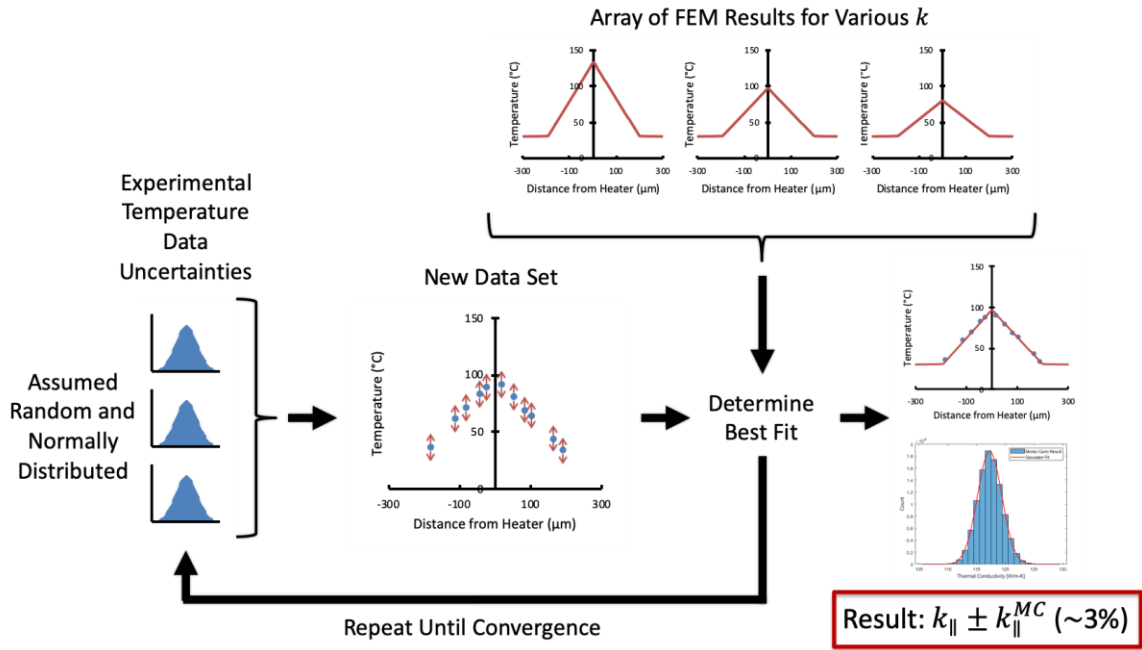


Figure 18. Flow chart summary of the Monte Carlo (MC) simulation implemented for determining the best-fit NCD in-plane thermal conductivity, $k_{||}$, and the MC-based uncertainty, $k_{||}^{MC}$. Experimental results shown in Table 2 demonstrate that $\delta k_{||}^{MC} \approx 3\%$ on average.

2.4.2 Uncertainty: Analytical Derivation

The experimental temperature uncertainty, δT , of each thermometry measurement that was input to the MC simulation for determining $k_{||}$ was resolved by analytically propagating the component measurement uncertainties attributed to the limited accuracy,

precision, and resolution inherent to each thermometry technique according to the following summations in quadrature:

$$\delta T_{exp}^{Raman} = \sqrt{\left(\frac{\partial T}{\partial A_{Ti}} \delta A_{Ti}\right)^2 + \left(\frac{\partial T}{\partial \omega} \delta \omega\right)^2 + \left(\frac{\partial T}{\partial \omega_o} \delta \omega_o\right)^2 + \left(\frac{\partial T}{\partial T_o} \delta T_o\right)^2} \quad (5)$$

for Raman thermometry and

$$\delta T_{exp}^{ERT} = \sqrt{\left(\frac{\partial T}{\partial A_R} \delta A_R\right)^2 + \left(\frac{\partial T}{\partial R} \delta R\right)^2 + \left(\frac{\partial T}{\partial R_o} \delta R_o\right)^2 + \left(\frac{\partial T}{\partial T_o} \delta T_o\right)^2} \quad (6)$$

for ERT, where the partial derivatives were evaluated by differentiating Equations 1 and 2 respectively.

Each of the calibration coefficient uncertainties, δA_{Ti} and δA_R , was attributed to the statistical error resulting from the linear regression of the calibration data and stochastic uncertainties associated with the calibration measurements. The statistical error, δA^{stat} , was quantified by the 95% confidence interval about the fitting parameter, A , resulting from linear regression. The stochastic uncertainties in the measured sample base temperatures and Raman peak positions were propagated into a calibration coefficient uncertainty, δA^{stoch} , by deducing A via MC simulation. Therefore, the total calibration coefficient uncertainties, δA_{Ti} and δA_R , were determined by summing the statistical and stochastic components in quadrature:

$$\delta A = \sqrt{(A^{stat})^2 + (A^{stoch})^2} \quad (7)$$

The peak position uncertainty, $\delta\omega$ (or $\delta\omega_o$), for each Raman measurement was attributed to the statistical precision of each measurement (consisting 20 and 40 acquisitions at the power and reference conditions respectively) and the stochastic uncertainty associated with the spectral resolution of the spectrometer. The statistical precision, $\delta\omega^{stat}$ (or $\delta\omega_o^{stat}$), of each measurement was quantified by the 95% confidence interval about the sample mean of the 20 (or 40) repeated acquisitions at the power (or reference) condition. The spectral resolution of the spectrometer, $\delta\omega^{res}$, was defined as the smallest change in peak position that can be detected by the spectrometer and was determined to be 0.24 cm^{-1} for our spectrometer configuration by inspecting a Raman spectrum acquisition of a TiO_2 particle. Furthermore, the stochastic uncertainty in peak position, $\delta\omega^{stoch}$ (or $\delta\omega_o^{stoch}$), not to be confused with $\delta\omega^{res}$, was defined as the uncertainty in peak position attributed to fitting a Raman spectrum acquisition to a pseudo-Voigt function by nonlinear regression. Hence, $\delta\omega^{stoch}$ (or $\delta\omega_o^{stoch}$) was quantified by assuming that each spectral datum of a Raman spectrum acquisition was normally distributed about its measured value according to $\delta\omega^{res}$, and thereby propagating $\delta\omega^{res}$ into $\delta\omega^{stoch}$ (or $\delta\omega_o^{stoch}$) by deducing peak position, ω (or ω_o), via MC simulation.

The resistance uncertainty, δR (or δR_o), for each ERT measurement was quantified as the measurement resolutions of the Keithley 2400 Sourcemeter and the Agilent 34410A 6 ½ Digit Multimeter. The sample base reference temperature uncertainty, δT_o , was quantified as the measurement resolution of the Fluke 54IIB Thermometer paired to a K-type thermocouple. The individual component relative uncertainties of the temperature

measurements from an exemplary Raman thermometry and ERT experiment are shown in Figure 19.

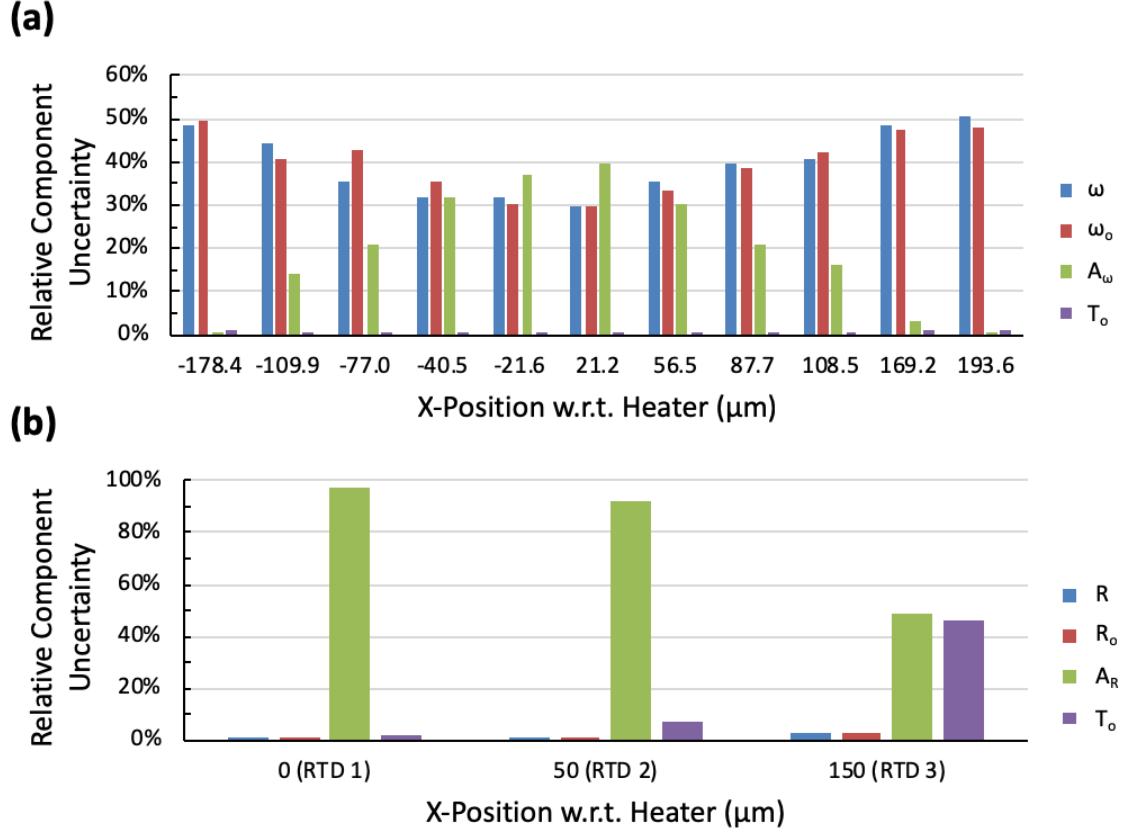


Figure 19. Individual component uncertainties (each component uncertainty = $\left(\frac{\partial T}{\partial p} \delta p\right)^2$ for component p) of exemplary TiO_2 particle-assisted Raman thermometry and ERT temperature measurements.

2.4.3 Uncertainty: Sensitivity Analysis

Beyond the primary utility of propagating experimental uncertainties, extending MC simulation to include stochastic sampling of FEM input parameter uncertainties (e.g. from other material properties, boundary conditions, etc.) is computationally impractical. The long simulation time typical of finite element analysis (~1 min or greater) would dramatically compound the iterative MC simulation time. Therefore, a more appropriate

alternative for approximating the propagated uncertainty contributions of the FEM input parameters is by means of sensitivity analysis.

Generally, sensitivity is an assessment of how strongly a model output result is affected by a small change to an input parameter and can be treated as an indirect measure of uncertainty. For our FEM, we defined sensitivity as an assessment of the relative change in the temperature rise resulting from a 5% relative change in an input parameter according to

$$S_p = \frac{\delta\Delta T / \Delta T}{\delta p / p} = \frac{\delta\Delta T / \Delta T}{0.05} \quad (8)$$

where S_p is the sensitivity to input parameter, p ; $\delta\Delta T / \Delta T$ is the relative change of output temperature rise, ΔT ; and $\delta p / p$ is the relative change of the input parameter, p . Assuming that the auxiliary input parameter uncertainties (not $\delta k_{||}$) are known and uncorrelated, the unknown fitting parameter uncertainty ($\delta k_{||}$) can be expressed in terms of the known parameter uncertainties by summation in quadrature [72] according to

$$\delta k_{||}^S = k_{||} \cdot \sqrt{\sum_p \left(\frac{S_p}{S_k} \frac{\delta p_{exp}}{p} \right)^2} \quad (9)$$

where $\delta k_{||}^S$ is the sensitivity-based uncertainty in $k_{||}$ propagated from the experimental input parameter uncertainties, δp_{exp} , and S_p and S_k are the sensitivities to the input parameters, p , and fitting parameter, $k_{||}$, respectively. Ideally, sensitivity to the fitting parameter should be high ($S_k > 0.2$ [44]) and sensitivity to the auxiliary input parameters should be low

($S_p < 0.05$ [44]) to obtain a reasonable propagated uncertainty ($\delta k_{\parallel}^S/k_{\parallel} < 10\%$). These ideal circumstances permit relatively high auxiliary input parameter uncertainties ($\delta p_{exp}/p \approx 25\%$) without affecting the propagated uncertainty [44].

The results of our sensitivity analysis of an NCD suspended membrane with backside-deposited aluminum are shown in Figure 20. The FEM input parameters explored in the sensitivity analysis are listed in Table 1. Since the sensitivities to η , G_1 , G_2 , G_3 , and T_b were found to be negligibly low across the k_{\parallel} domain, inaccurate or highly uncertain measurements of these input parameters only negligibly propagated to δk_{\parallel}^S . Further, since the sensitivity to ε was negligibly low and the sensitivity to h only became non-negligible at low thermal conductivities ($k_{\parallel} \leq 10$ W/mK), inaccuracies inherent to boundary condition approximations also only negligibly propagated to δk_{\parallel}^S . However, the high sensitivity to t_{NCD} indicated that precise measurement of the NCD suspended membrane thickness was critical for accurately resolving k_{\parallel} – a common requirement amongst thin film thermal property measurement techniques.

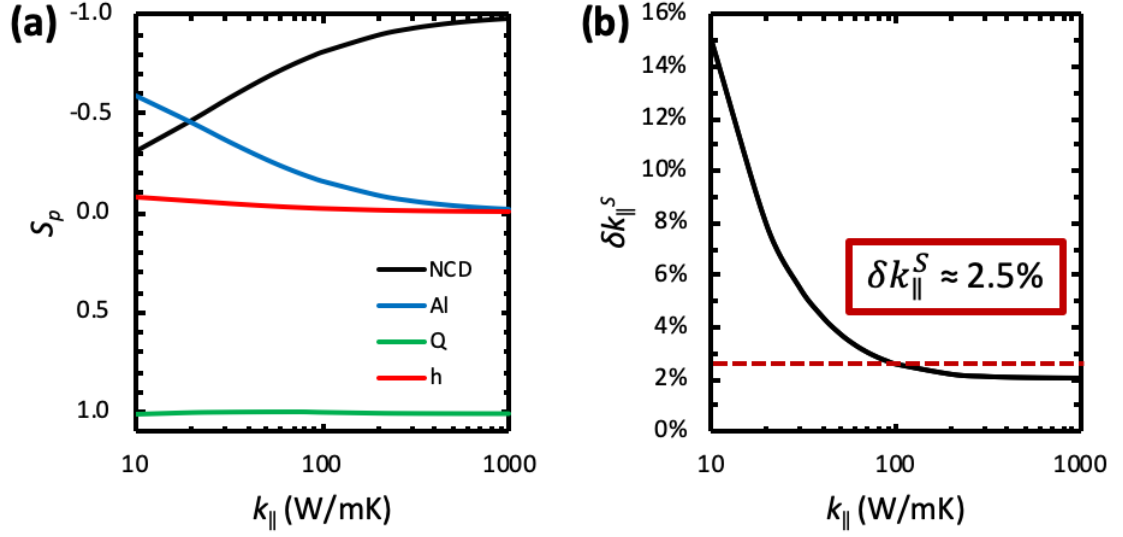


Figure 20. Sensitivity analysis results of an NCD suspended membrane with backside-deposited Al for which input parameters are listed in Table I. **(a)** Sensitivity as a function of (NCD) k_{\parallel} . The sensitivities to (NCD) k_{\parallel} and t_{NCD} are indistinguishable and shown as one curve (black). The sensitivities to k_{Al} and t_{Al} are indistinguishable and shown as one curve (blue). The sensitivities to η , G_1 , G_2 , G_3 , and T_b are negligibly low and omitted for clarity. **(b)** Sensitivity-based uncertainty in k_{\parallel} (δk_{\parallel}^S) as a function of k_{\parallel} demonstrates that $\delta k_{\parallel}^S \approx 2.5\%$ for our NCD samples.

Table 1. FEM parameters explored in the sensitivity analysis of a NCD suspended membrane with backside-deposited Al shown in Figure 20.

Parameter	Symbol	Nominal Value	Units	Relative Measurement Uncertainty
NCD in-plane thermal conductivity	$k_{ }$	10 – 1000	W/mK	See Figure 20
NCD thickness	t_{NCD}	1.0 ^a	μm	2% ^a
NCD anisotropy ratio ($k_{\perp}/k_{ }$)	η	2.8		5%
Al thermal conductivity	k_{Al}	200	W/mK	5%
Al thickness	t_{Al}	0.10 ^a	μm	6% ^a
NCD/Al interface conductance	G_1	147 ^b	MW/m ² K	12% ^b
NCD/Si interface conductance	G_2	70 ^b	MW/m ² K	20% ^b
RTD/NCD interface conductance	G_3	169 ^b	MW/m ² K	9% ^b
Input heating rate	Q	200.0	mW	0.1%
Sample base temperature	T_b	30.0	°C	20%
Convection coefficient	h	N/A	W/m ² K	5%
Thermal emissivity (NCD & RTD)	ε	0.02		5%

^aMeasured via transmission electron microscopy (TEM) by collaborators at UCLA

^bMeasured via TDTR by Luke Yates and Zhe Cheng

2.4.4 Error Analysis

Rigorous uncertainty estimation is an essential component for precise characterization of thin film thermal properties. However, even a perfectly accurate and precise experimental technique can lead to inaccurate thermal property results if the errors inherent to the comparative model are not carefully considered. The model errors relevant to deducing thermal conductivity according to the experimental methods presented in this work are those that arise from model assumptions that prevent perfect reproduction of the

temperature distribution present in experiment. The model assumptions that meet this criterion were those that involved boundary condition and material property assignments. Moreover, the only relevant boundary condition or material property assumption not considered via sensitivity analysis was the assumed temperature independence of NCD $k_{||}$. This assumption was particularly important to validate for the measurement techniques used in this work since the membrane-averaged $k_{||}$ determined required the presence of an uneven temperature distribution across the membrane. Therefore, to validate this assumption, the NCD $k_{||}$ temperature dependence of samples 1b, 2a, and 2b were measured via ERT according to methods presented in Section 2.5. An example of these temperature dependence results is presented in Figure 21 and demonstrates minimal NCD $k_{||}$ temperature dependence within the temperature range of 30 – 130 °C (maximum membrane temperatures did not exceed 130 °C). The increased uncertainties in $k_{||}$ measured at average membrane temperatures below 50 °C ($T_{avg} < 50$ °C or $\Delta T_{avg} < 20$ °C) were consistent with suspended membrane thermal conductivity uncertainty analysis results presented in literature [58] that observed excessive uncertainty in thermal conductivity determined from small temperature rises ($\Delta T < 20$ K). Furthermore, above average membrane temperatures of 50 °C ($T_{avg} > 50$ °C or $\Delta T_{avg} > 20$ °C), Figure 21 shows a slightly increasing $k_{||}$ with respect to T_{avg} that is consistent with experimental temperature dependent thermal conductivity results measured from NCD films reported in literature [73].

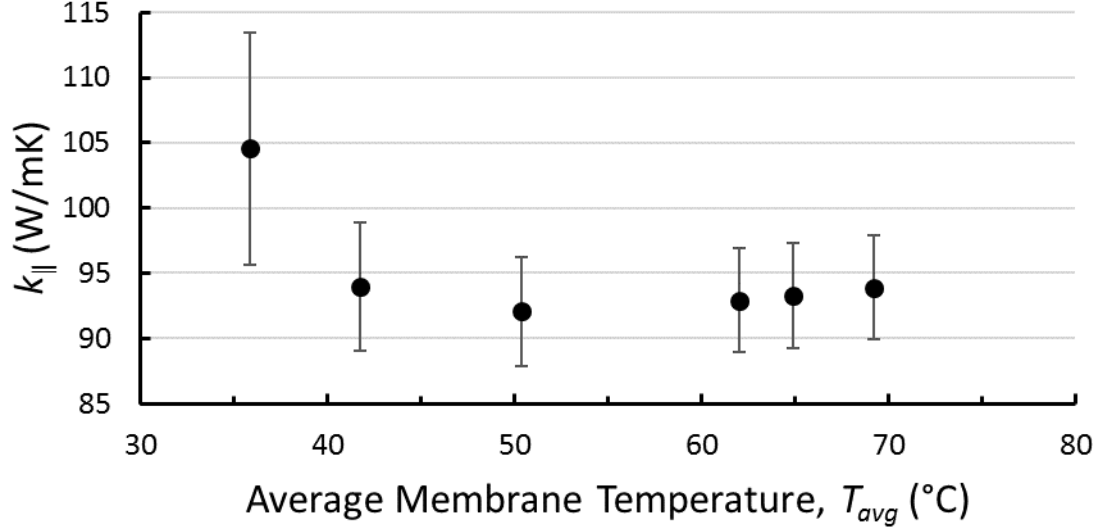


Figure 21. Temperature dependent thermal conductivity measurement results as a function of average membrane temperature calculated from the best-fit FEM from sample 1b. The vertical error bars represent the total in-plane thermal conductivity uncertainty, $\delta k_{||}$. The larger vertical error bars for $T_{avg} < 50$ °C indicate increased uncertainty due to an insufficient average temperature rise, $\Delta T_{avg} = T_{avg} - T_b$, where T_b is the sample base temperature.

In addition to enabling a rigorous assessment of model error, utilizing an FEM as the comparative model for deducing $k_{||}$ was particularly useful for accommodating the extraneous back-side aluminum thin film present on our suspended membrane samples. However, in the absence of extraneous thin film coatings, it is possible to drastically simplify post-measurement analysis by assuming 1D thermal conduction across the entire suspended membrane and applying Fourier’s law according to

$$k_{||}^{1D} = \frac{Q}{t \cdot L} \cdot \left(\frac{\Delta T}{\Delta x} \right)^{-1} \quad (10)$$

where $k_{||}^{1D}$ is the suspended membrane in-plane thermal conductivity (assuming 1D conduction), Q is the heating rate sourced from the centerline heater, t is the suspended membrane thickness, L is the centerline heater length, ΔT is the temperature rise sampled

from the upper surface of the 1D region, and Δx is the suspended membrane width. We have assessed the model error associated with making this 1D assumption independently of measurement uncertainty by performing a comparative analysis between the FEM and Fourier's law according to

$$\varepsilon_{1D} = \frac{k_{\parallel}^{1D} - k_{\parallel}^{FEM}}{k_{\parallel}^{FEM}} \quad (11)$$

where ε_{1D} is the 1D assumption model error, k_{\parallel}^{1D} is defined according to Equation 9 with ΔT sampled from FEM results, and k_{\parallel}^{FEM} is the true NCD in-plane thermal conductivity input to the FEM. The results of this comparative error analysis are presented in Figure 22 and demonstrate that deducing k_{\parallel} according to a simple 1D approximation results in less than 5% model error ($\varepsilon_{1D} < 5\%$) for NCD suspended membrane in-plane thermal conductivities of 90 W/mK and greater ($k_{\parallel} \geq 90$ W/mK) and for membrane dimensions with a length-to-width aspect ratio greater than 4.5. Results (not shown) have also demonstrated that NCD suspended membranes of thicknesses greater than 5 μm begin deviating from the 1D thermal transport condition by experiencing a temperature gradient through the thickness of the membrane sample.

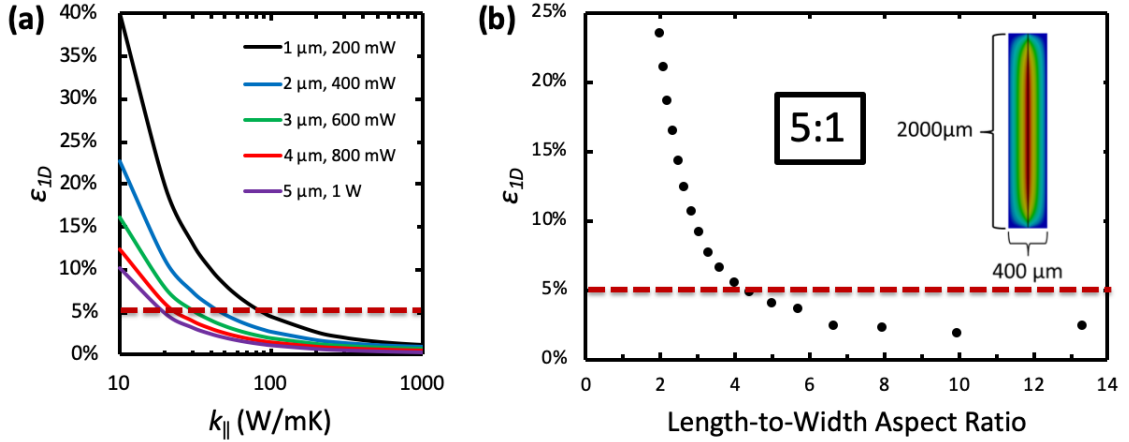


Figure 22. Comparative model error analysis between FEM and Fourier's law assuming 1D thermal conduction. The dashed line indicates the conditions that yield 1D assumption model error less than 5% ($\epsilon_{1D} < 5\%$) (a) 1D assumption model error (ϵ_{1D}) as a function of NCD in-plane thermal conductivity ($k_{||}$) input to the FEM. Linear power density along the centerline heater (Q/t in Equation 9) was held constant to maintain a nearly constant temperature rise (ΔT in Equation 9). (b) 1D assumption model error (ϵ_{1D}) as a function of length-to-width aspect ratio.

2.5 Experimental Results and Discussion

The experimental in-plane thermal conductivity results obtained for the NCD suspended membrane samples measured via Raman thermometry and ERT are presented in Table 2. The temperature profile measured from sample 2a via TiO_2 particle-assisted Raman thermometry and ERT is shown in Figure 23. As mentioned in Section 2.3.2, utilizing the temperature measured from the centerline heater (RTD 1) in the model fitting routine for determining $k_{||}^{ERT}$ resulted in greater overall uncertainty, $\delta k_{||}^{ERT}$, for most samples. Occasionally however, including temperature measured from RTD 1 resulted in lower overall uncertainty. This observation can be explained by the fact that a third temperature measurement is significantly more information useful for model fitting than two temperature measurements from RTDs 2 and 3. Considering using temperature measurements from all three RTDs or only RTDs 2 and 3, the fitting result of minimum

uncertainty was determined to be the best-fit k_{\parallel}^{ERT} . The histograms resulting from the MC simulations used to propagate the experimental temperature uncertainties from Raman thermometry and ERT measurements from sample 2a into MC-based uncertainties, $\delta k_{\parallel}^{MC}$, are shown Figure 24. As shown in Figure 21 and discussed in Section 2.4.4, the overall uncertainty measured via ERT, $\delta k_{\parallel}^{ERT}$, tended to increase and an unexplained measurement bias was observed from k_{\parallel}^{ERT} measurements obtained at average membrane temperatures below 50 °C ($T_{avg} < 50$ °C or $\Delta T_{avg} < 20$ °C). This challenge of resolving k_{\parallel} at low average membrane temperatures encountered using ERT can be overcome by using TiO₂ particle-assisted Raman thermometry as demonstrated experimentally with k_{\parallel}^{Raman} measurements from sample 4 shown in Figure 25. Alternatively, implementing the RTD 1 temperature measurement improvement discussed in Section 2.3.2 might improve k_{\parallel}^{ERT} measurement accuracy and uncertainty.

Table 2. Experimental in-plane thermal conductivity (k_{\parallel}) results obtained from TiO₂ particle-assisted Raman thermometry, ERT, and the 1D lateral thermal conduction approximation. A dash indicates data that was not measured and is otherwise unknown. The note of N/A indicates that the 1D thermal transport simplifying assumption is not applicable due to the presence of backside aluminum.

Sample	NCD Film Thickness (μm)	Nucleation Seed Size (nm)	k_{\parallel}^{Raman} (W/mK)	k_{\parallel}^{ERT} (W/mK)	k_{\parallel}^{1D} (W/mK)
1a	1.06 ± 0.02	4	99 ± 4 (4%)	-	N/A
1b			-	94 ± 4 (4%)	N/A
2a	1.06 ± 0.05	40	117 ± 5 (4%)	118 ± 4 (3%)	N/A
2b			-	118 ± 4 (3%)	N/A
3	1.01 ± 0.05	-	102 ± 5 (5%)	-	105
4	3.02 ± 0.15	-	157 ± 8 (5%)	-	N/A

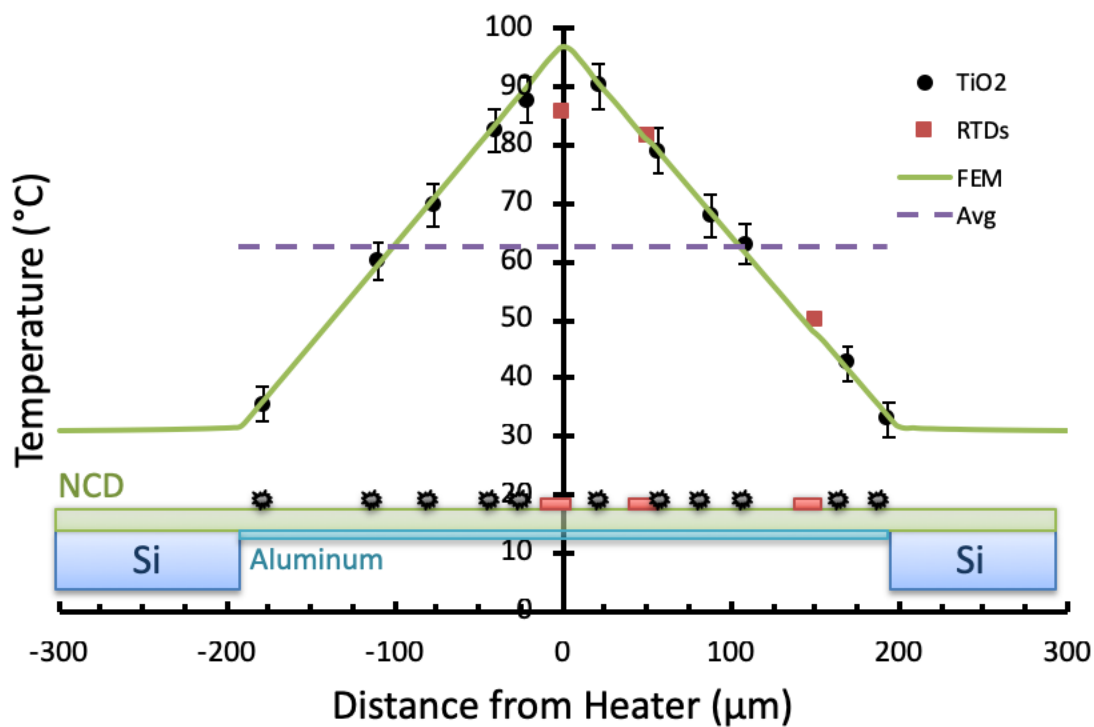


Figure 23. Temperature profile measured from sample 2a via TiO₂ particle-assisted Raman thermometry and electrical resistance thermometry (ERT) with 200 mW dissipated from the centerline heater (RTD 1). The independent steady-state thermometry techniques demonstrated precise agreement with the finite element model (FEM). The average membrane temperature, $T_{avg} = 62.8$ °C, calculated via the FEM is denoted by the dashed line. As discussed in Section 2.3.2, the temperature measured from RTD 1 understated the peak membrane temperature.

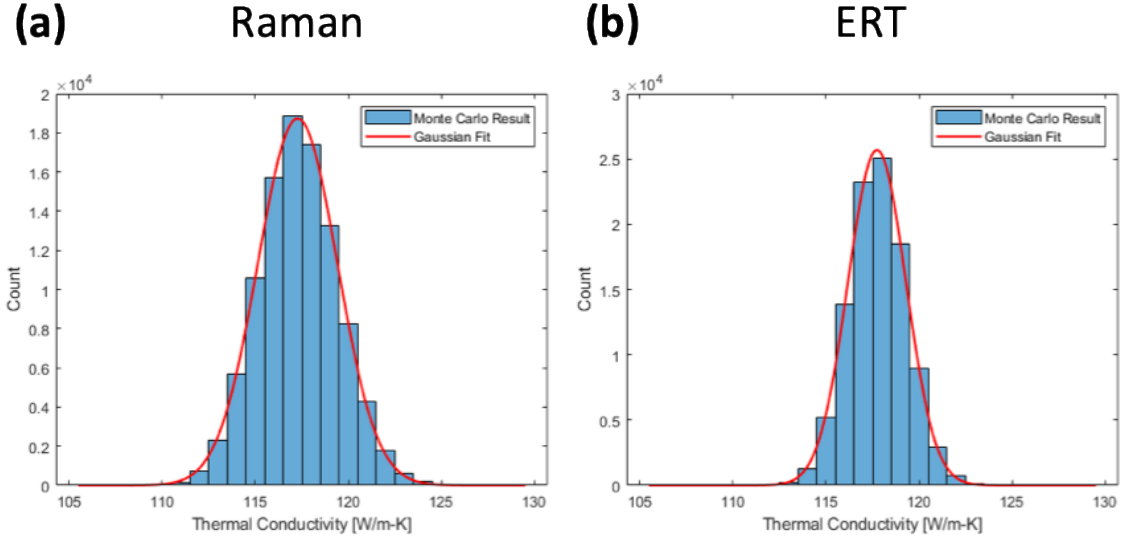


Figure 24. Histograms resulting from the MC simulations used to propagate the experimental temperature uncertainties from **(a)** Raman thermometry and **(b)** ERT measurements from sample 2a into MC-based uncertainties, $\delta k_{||}^{MC}$.

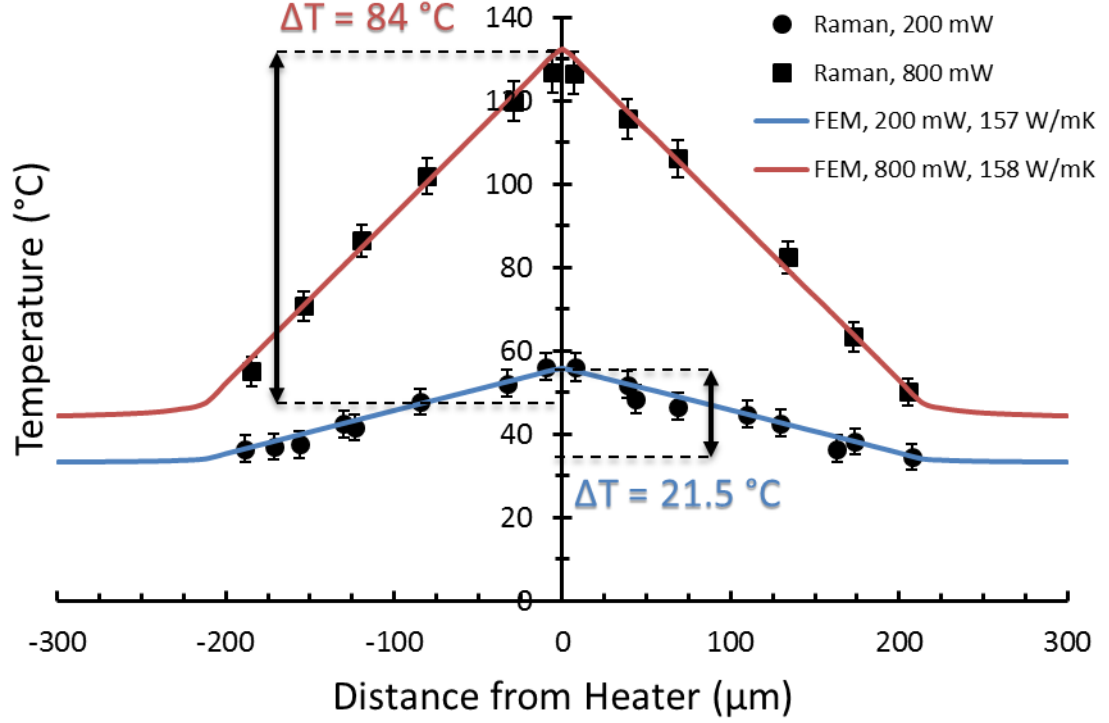


Figure 25. Temperature profile measured from sample 4 (3 μm) via TiO_2 particle- assisted Raman thermometry with 200 mW and 800 mW dissipated from the centerline heater. The $k_{\parallel}^{\text{Raman}}$ results of $157 \pm 8 \text{ W/mK}$ and $158 \pm 8 \text{ W/mK}$ measured with temperature rises of 21.5 $^{\circ}\text{C}$ and 84 $^{\circ}\text{C}$, respectively, demonstrate the possibility of resolving k_{\parallel} for low temperature rises via TiO_2 particle-assisted Raman thermometry.

The precise agreement between $k_{\parallel}^{\text{Raman}}$ and $k_{\parallel}^{\text{ERT}}$ measured from sample 2a demonstrates that the efficacy of both measurement techniques. Both measurement techniques have demonstrated the ability to resolve thermal conductivity with overall uncertainties less than 5% ($\delta k_{\parallel} \leq 5\%$), a result that is a substantial improvement upon the 11-15% overall uncertainty computed for in-plane thermal conductivity results measured from similar 1 μm diamond samples using TDTR [54]. Further, unlike results resolved from standard implementations of TDTR and FDTR, the in-plane thermal conductivity results resolved from both Raman thermometry and ERT are inherently membrane-averaged results. Recent work by Sood *et al.* has demonstrated the capability of spatially

mapping the thermal conductivity of large-grained boron-doped CVD diamond (average grain size $\sim 25\text{ }\mu\text{m}$) with a step size of $4\text{ }\mu\text{m}$ [51]. Although this technique is extremely useful for studying the local thermal environment of PCD at length scales comparable to PCD grain sizes, it is important for many applications to know the effective, spatially-averaged thermal conductivity of a material subject to a 1D heat flux. Sood *et al.* report that up to 35 independent TDTR measurements could be necessary to achieve a spatially averaged result that lies within $\pm 10\%$ of the global mean with a probability of $> 95\%$ (for a relative spatial variability of 30%), a proposition that entails prohibitively long measurement times using standard TDTR mapping implementations [51]. Although the TiO_2 particle-assisted Raman thermometry technique for measuring in-plane thermal conductivity of thin films is particularly time consuming, ERT requires a fraction of the time with little sacrifice to measurement accuracy and precision. Moreover, the error-based criterion developed to determine the limiting experimental conditions that permit the simplifying assumption of 1D thermal conduction permits drastically reduced post-measurement analysis necessary for deducing k_{\parallel} compared to alternative measurement techniques.

Although spatially resolved TDTR thermal conductivity mapping results measured from similar $1\text{ }\mu\text{m}$ NCD films published by Cheaito *et al.* demonstrate significant sensitivity to local variability within a membrane sample [74], the agreement in k_{\parallel} measured between membrane samples 1a and 1b and similarly between membrane samples 2a and 2b demonstrate low variability between adjacent membrane-averaged in-plane thermal conductivities. The k_{\parallel} results of $\sim 97\text{ W/mK}$ and $\sim 118\text{ W/mK}$ measured from wafer 1 (4 nm seeds) and wafer 2 (40 nm seeds), respectively, indicate that PCD grown from 40

nm nucleation seeds is more thermally conductive than PCD grown from 4 nm seeds, likely due to the larger grain size. These results are supported by a similar study reported in literature by Liu *et al.* that found that the size of diamond nucleation seeds plays an important role in the material microstructural and thermal properties and stability [75]. Liu *et al.* compared high-resolution SEM images of the GaN-diamond interface of GaN-on-diamond wafers fabricated by direct PCD growth (see Section 3.1.2 for process summary) from 30 nm and 100 nm nucleation seeds and concluded that 30 nm nucleation seeds prevented the formation of microscopic defects and voids [75]. Furthermore, the results of our comparative thermal conductivity analysis ($k_{\parallel}^{40nm} > k_{\parallel}^{4nm}$) indicates that an optimum nucleation seed size exists for optimal NCD k_{\parallel} .

The k_{\parallel} results of ~ 102 W/mK and ~ 157 W/mK measured from wafer 3 (~ 1 μ m) and wafer 4 (~ 3 μ m), respectively, are compared to literature values of PCD k_{\parallel} as a function of thickness [40] in Figure 26 and demonstrate reasonable agreement to the trend of previously reported results. The variation among measured and published values is not surprising since the grain size evolution and thereby in-plane thermal conductivity of NCD have been shown to largely depend on the CVD growth method and conditions [52, 53]. Prior work has demonstrated that a thermal conductivity gradient in the cross-plane direction can be deduced by using k_{\parallel} measurements of CVD diamond films of various thicknesses grown in a stepwise fashion [52]. Although such a thermal conductivity gradient is useful for constructing a more realistic GaN-on-diamond HEMT thermal model, a complete sample set of several thicknesses grown according to the same growth conditions must be used to accurately represent the thermal conductivity of a particular PCD substrate. Therefore in lieu of incorporating our k_{\parallel} results measured from samples 3

and 4 (1 and 3 μm respectively) into a thermal FEM, an effective (thickness-averaged) thermal conductivity measured in prior work [76] from one of the GaN-on-diamond samples presented in Section 3.3.1 (sample G1) has been used for comparative thermal analysis (see Section 3.4.2.3) to demonstrate the thermal consequences of the low-thermal conductivity near-nucleation NCD in polycrystalline CVD diamond.

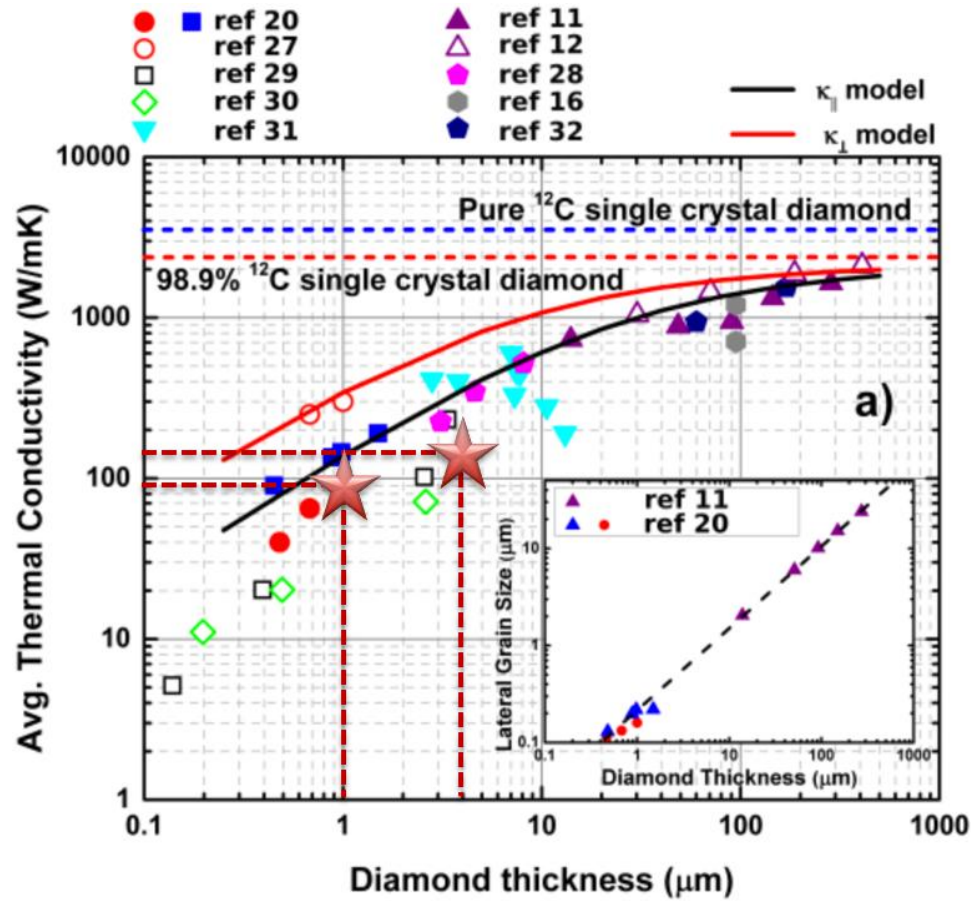


Figure 26. Values of $k_{||}$ measured from Samples 3 and 4 (stars) compared to values of $k_{||}$ as a function of thickness reported in literature [40].

2.6 Summary and Conclusions

In an effort to ensure a rigorous estimation of in-plane thermal conductivity and its overall uncertainty, an explicit uncertainty analysis framework has been developed for two

steady-state thermometry techniques: Raman thermometry and electrical resistance thermometry. The uncertainty analysis framework consisted of a combination of analytical, stochastic, and parametric analysis methods that considered uncertainty contributions from component experimental conditions and material properties. In addition, the best practices and experimental conditions that permit the simplifying assumption of 1D thermal conduction along the in-plane direction have been presented by establishing an error criterion. The analysis methodology and the accuracy and precision of the empirical in-plane thermal conductivity results was validated by measuring a single membrane sample with both steady-state thermometry techniques. The six nanocrystalline CVD diamond suspended membrane samples were organized into sample sets to perform two comparative analyses intended to provide insight for improving the quality and thermal properties of the initial near-nucleation layers of PCD diamond films for heat spreading applications in GaN-on-diamond HEMT device technology. One of the comparative analyses has revealed that 40 nm NCD nucleation seeds lead to higher thermal conductivity thin films than 4 nm nucleation seeds, a result that has been attributed to the mitigation of interfacial material defects and voiding. The other comparative analysis has assessed the initial progression of the thickness-dependent thermal conductivity gradient that results from nanocrystalline diamond grain coalescence within the first few microns of polycrystalline CVD diamond growth.

CHAPTER 3. PCD SUBSTRATE IMPLEMENTATION: GROWTH VS BONDING

3.1 Introduction to GaN-on-Diamond Fabrication

Although GaN-on-diamond technology is extremely attractive for addressing the high local heat densities generated by high-power RF AlGaIn/GaN HEMTs, achieving a high-quality interface between GaN and diamond is particularly challenging due to the large lattice and coefficient of thermal expansion (CTE) mismatches of 11% and 41% respectively. Hence, the formation of a coherent GaN-diamond interface requires the use of a transition layer or interface material that is typically disordered and thermally resistive. In addition to inherent thermal properties of the interface material, a combination of the following phonon scattering mechanisms (illustrated in Figure 27) have been used to describe the complex GaN-diamond thermal interface resistance: (i) scattering at interface material boundaries, (ii) scattering on point defects, dislocations, and other defects within interface material, and (iii) scattering by near-interfacial disorder in the GaN and diamond substrate [77]. Due to the complexity of these concurrent scattering mechanisms, the individual resistive contributions are typically lumped into a single effective thermal boundary resistance, TBR_{eff} , that is more easily measured and practical for device-level thermal analysis.

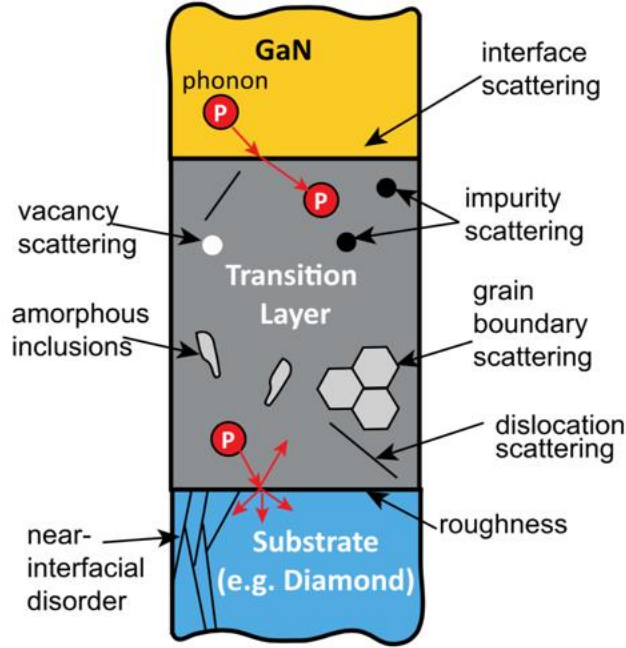


Figure 27. Summary of the phonon scattering mechanisms contributing to the thermal interface resistance in GaN-on-substrate composites. [77]

In general, there are two approaches to fabricating GaN-on-diamond composites for AlGaIn/GaN HEMT devices: (i) AlGaIn/GaN heteroepitaxy on a single-crystal diamond (SCD) substrate and (ii) transferring a pre-grown AlGaIn/GaN heterostructure to a polycrystalline diamond (PCD) substrate. Although the limited merits of GaN heteroepitaxy on SCD are presented in Section 3.1.1 for completeness, the present high cost and SCD wafer diameter limitations prohibit the application of this GaN-on-diamond approach. Hence, the comparative analysis presented in this work examines the predominant pre-grown AlGaIn/GaN heterostructure transfer technique alternatives: (i) direct growth and (ii) wafer bonding of a PCD substrate onto the GaN-side of an AlGaIn/GaN heterostructure.

3.1.1 AlGaN/GaN Heteroepitaxy on Single-Crystal Diamond

Short of its inherent lattice mismatch with GaN, single-crystal diamond is an ideal substrate material for the thermal management of high-power and high-frequency AlGaN/GaN HEMT applications due to its extremely high thermal conductivity at room temperature of 2200 W/mK [78]. Moreover, successful high-quality AlGaN/GaN heteroepitaxy on SCD substrates would circumvent the undesirable thermal conductivity depression that accompanies the near-nucleation NCD necessary for PCD growth demonstrated in CHAPTER 3. This thermal advantage has been demonstrated in literature via *in situ* infrared radiation (IR) thermography measurements of AlGaN/GaN HEMTs epitaxially grown on SCD (111) substrates via metal-organic vapor-phase epitaxy (MOVPE) [30, 79].

Hirama *et al.* demonstrate device thermal resistances (R_{th}) of 4.1 and 1.5 K·mm/W measured from HEMTs grown on Ib-type and IIa-type SCD substrates that were each reported to be the lowest R_{th} ever achieved [30, 79]. The lower R_{th} achieved on the latter HEMT devices was attributed to the higher thermal conductivity of IIa-type SCD over that of Ib-type SCD [30]. These R_{th} results obtained using SCD substrates suggest that the substrate thermal conductivity contributions to R_{th} have been maximized and hence further R_{th} reductions must come from improving the GaN thermal conductivity and the GaN-diamond TBR_{eff} . However, this GaN-on-diamond fabrication method of GaN heteroepitaxy on SCD substrates requires extensive use of thermally resistive strain-relief transition layers to accommodate for the large GaN-diamond lattice mismatch (11%) [79], a design strategy that is also employed for the even more poorly lattice-matched GaN-on-Si heteroepitaxial composite [80]. Without appropriate strain-relief, excessive wafer bow

and low-quality AlGaIn/GaN heterostructure can lead to poor electrical device performance or even be prohibitive for functioning HEMT devices [80-82]. Therefore, due to these thermally resistive yet mechanically necessary GaN-diamond interface transition layers and the high cost and limited diameter of SCD substrates, GaN-on-diamond methods that employ PCD are preferred for thermal management of high-power and high-frequency AlGaIn/GaN HEMT devices. PCD has become increasingly viable since wafers can now be grown in diameters larger than 3 in. while maintaining most of the thermal conductivity improvement (1000 – 2000 W/mK) depending on the diamond growth conditions [39, 82].

3.1.2 AlGaIn/GaN Heterostructure Transfer: PCD Growth and Bonding

The AlGaIn/GaN heterostructure transfer is a multi-step process that involves AlGaIn/GaN heteroepitaxy on conventional substrates (Si, SiC, or sapphire) to achieve optimal material quality and device integrity followed by the replacement of the epitaxial growth substrate with a high thermal conductivity PCD substrate. The general process steps for typical GaN-on-PCD heterostructure transfer processes are illustrated in Figure 28. and include: (i) industry standard AlGaIn/GaN heteroepitaxial growth on Si, SiC or sapphire, (ii) bonding of a temporary carrier wafer (Si, SiC or sapphire), (iii) removal of the growth substrate and interlayers, (iv) growth or bonding of the PCD substrate, and (v) removal of the temporary carrier wafer [29, 82, 83].

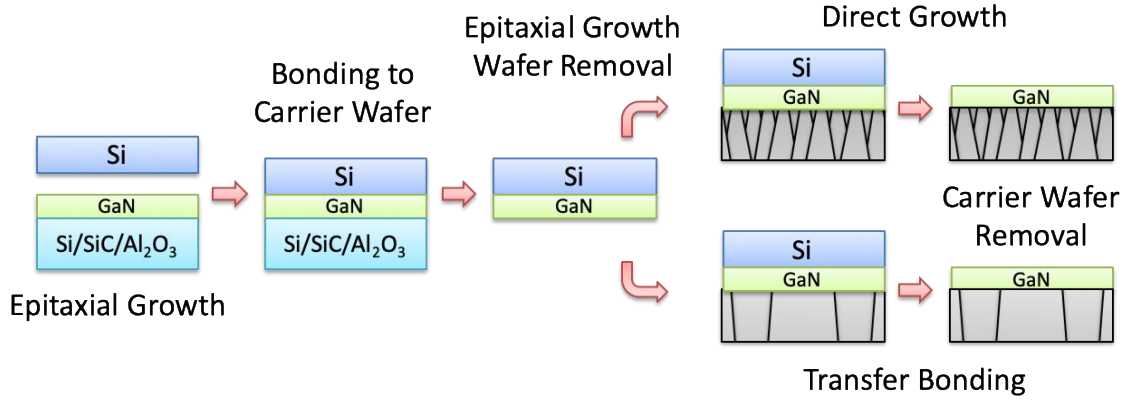


Figure 28. Schematic of typical GaN-on-diamond heterostructure transfer processes: direct growth and transfer bonding.

3.1.3 GaN-on-PCD Challenges: Thermal Boundary Resistance

In order to epitaxially grow PCD on GaN via CVD, a dielectric layer must first be deposited onto the exposed N-polar face of the GaN to accept diamond nucleation seeds and to protect the heterostructure from the hostile CVD diamond growth environment. The choice of low-thermal conductivity dielectric material, typically aluminum nitride (AlN) or silicon nitride (SiN), has been demonstrated in literature to be critical for optimizing the thermal transport across the GaN-PCD interface [28, 76, 84]. Sun *et al.* have shown that the GaN-PCD TBR_{eff} can be reduced by decreasing the thickness of the dielectric interlayer and report TBR_{eff} values within the range of 10 – 50 m²K/GW measured from interfaces with SiN interlayers of thicknesses between 20 – 100 nm [85]. Cho *et al.* measured the TBR_{eff} of GaN-PCD interfaces via time-domain thermoreflectance (TDTR) with SiN interlayers of thicknesses 22 and 31 nm supported with high resolution transmission electron microscopy (TEM) images and semiclassical phonon modeling to distinguish the most significant phonon scattering mechanisms depicted in Figure 27 [84]. Cho *et al.* report GaN-PCD TBR_{eff} values ranging from 17 – 32 m²K/GW and conclude that the SiN volume

resistance and phonon scattering on near-interfacial defects in the GaN and PCD are the predominant contributors to the GaN-PCD TBR_{eff} [84]. Moreover, Yates *et al.* demonstrated the importance of the GaN-diamond interface morphology by pairing TBR_{eff} measurements via TDTR with high resolution scanning electron microscopy (SEM) and TEM images [28]. Having considered GaN-diamond interfaces prepared with a nominal 5 nm SiN interlayer, a nominal 5 nm AlN interlayer, and no interlayer, Yates *et al.* found that the 5 nm SiN interlayer was the best choice of dielectric interlayer material with a TBR_{eff} of $9.5 \pm 3.8/-1.7 \text{ m}^2\text{K/GW}$ due to the smooth and ordered interface transition between the GaN and PCD [28].

It is also important to note that the material selection and quality of the GaN-PCD interlayer has been considered for its ability to enhance interfacial thermal transport beyond its utility as a protective coating and CVD seeding template. Although additional detail can be found in literature [86, 87], the general concept of enhancing interfacial thermal transport involves the insertion of a thin interlayer between dissimilar solids to activate or enable intermediate phonon vibrations within the interlayer to facilitate thermal transport from one solid to the other in a way that is otherwise unavailable without the phonon bridging interlayer. In accordance with the aforementioned GaN-PCD interfacial analysis presented by Yates *et al.* [28], the lowest GaN-PCD TBRs reported to date ($\sim 5 - 10 \text{ m}^2\text{K/GW}$) have been achieved primarily through optimizing the ordered transition within the interface as opposed to the effects of coupling phonon modes [28].

A particularly attractive alternative to growing PCD onto the AlGaIn/GaN heterostructure is to attach a pre-grown, free-standing PCD substrate wafer to the AlGaIn/GaN heterostructure. This transfer bonding solution for achieving GaN-on-PCD

HEMT wafers is attractive because the AlGaIn/GaN heterostructure and PCD substrate can be grown and processed separately before wafer bonding. This capability is thermally advantageous because, unlike grown GaN-on-PCD wafers, it is possible to remove the highly disordered and thermally resistive nucleation layers of the AlGaIn/GaN heterostructure and the PCD diamond before bonding. Chao *et al.* have presented thermal characterization and analysis of GaN-on-PCD HEMTs fabricated according to a low-temperature transfer bonding technique that leverages this capability of removing the thermally resistive GaN and PCD nucleation layers [29]. Chao *et al.* report a GaN-PCD TBR_{eff} of $34 \pm 5 \text{ m}^2\text{K/GW}$ and PCD thermal conductivity of 2160 W/mK that were measured via TDTR. For comparison, thermal characterization and analysis of GaN-on-PCD wafers fabricated by direct growth of PCD presented in literature report a GaN-PCD TBR_{eff} of $\sim 29 \text{ m}^2\text{K/GW}$ (average of room temperature measurements from two samples) and a thickness-averaged PCD thermal conductivity of $\sim 1300 \cdot (T/300\text{K})^{-0.9} \text{ W/mK}$ that were measured via a transient thermoreflectance technique [76]. Although both the AlGaIn/GaN heterostructure transfer alternatives share an approximately equal TBR_{eff} , the bonded GaN-on-PCD implementation has achieved superior thermal spreading within $1 \text{ }\mu\text{m}$ of the channel hot spot of a GaN-on-PCD RF power amplifier as demonstrated in Section 3.4.2.

3.1.4 GaN-on-PCD Challenges: Material Quality and Residual Stress

Although PCD growth on GaN with thin dielectric interlayers [28, 88] and PCD bonding to GaN using thin adhesion layers [29, 82] have proven to yield promising GaN-diamond TBR_{eff} reduction approaching the theoretical limit of $3 \text{ m}^2\text{K/GW}$ predicted by the diffuse mismatch model (DMM) for a perfect GaN-diamond interface [77], high-temperature ($\sim 700 \text{ }^\circ\text{C}$) heterostructure transfer processes such as CVD diamond growth or

various transfer bonding procedures induce mechanical strain and stress within the AlGaIn/GaN heterostructure as the GaN-PCD composite cools to room temperature. The resulting AlGaIn/GaN heterostructure material quality must be evaluated to ensure optimal HEMT device functionality. The residual stresses present in the GaN-PCD composite at room temperature (cooled from an elevated temperature) are primarily caused by the CTE mismatches between adjacent materials as illustrated in Figure 29. For the case of a thin epitaxial film of high CTE interfaced with a thick substrate of low CTE ($L_{epi} \ll L_{sub}$ and $CTE_{epi} > CTE_{sub}$) that is cooling down, the epitaxial film tends to contract more than the substrate that constrains biaxial deformation at the interface. Hence, the epitaxial film experiences biaxial tensile stress, the substrate experiences biaxial compressive stress, and the epi-substrate composite tends to develop a negative wafer bow (concave-up).

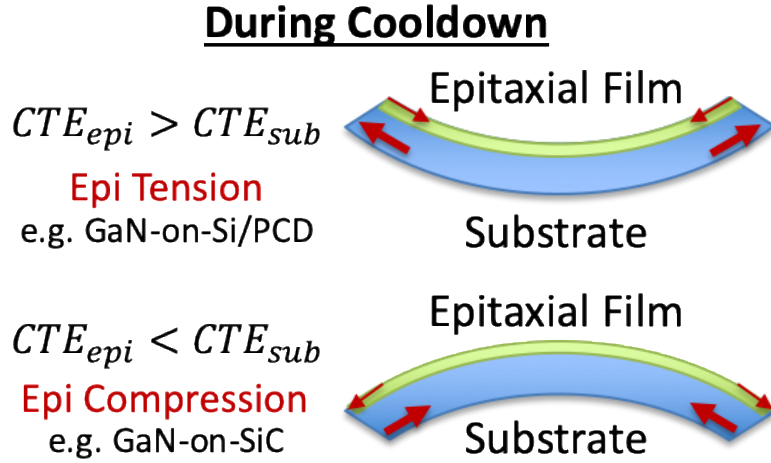


Figure 29. Schematic illustrating the accumulated strain and stress developed in epi-substrate composites during cooldown processes as a result of CTE mismatch. Cooldown processes tend to cause GaN-on-Si and GaN-on-PCD wafers to develop biaxial tension in the GaN and biaxial compression in the substrate (concave-up wafer bow) since the CTE of GaN is greater than that of Si and PCD ($CTE_{GaN} > CTE_{PCD}$) as shown in Figure 30.

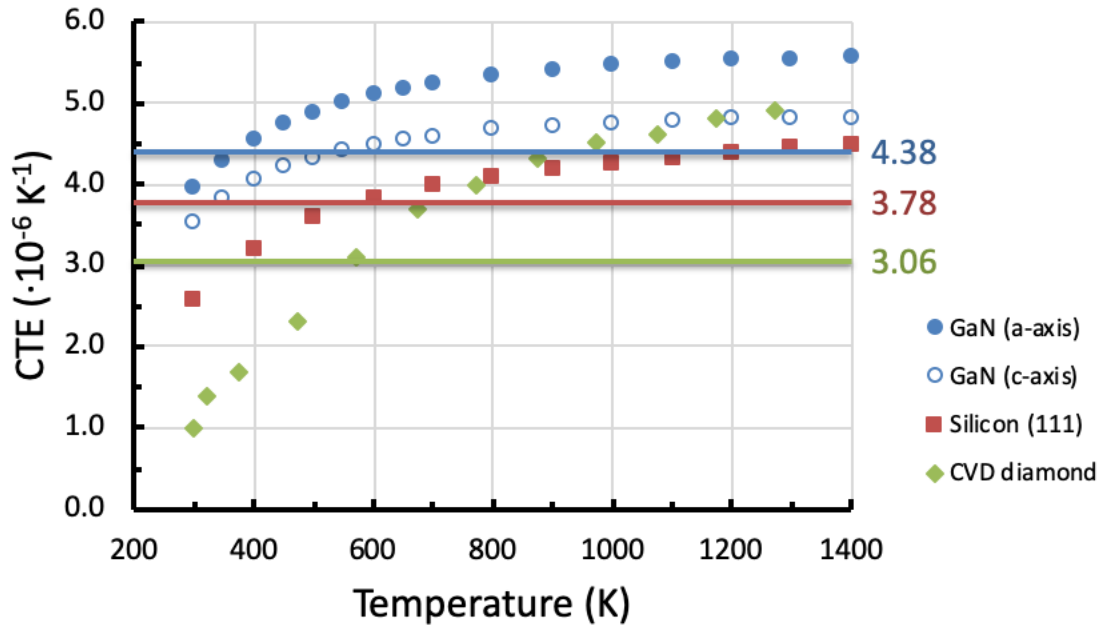


Figure 30. Coefficients of thermal expansion (CTEs) of GaN [89], silicon (111) [90], and CVD diamond [90]. The horizontal lines denote temperature independent CTEs that result from averaging the temperature dependent CTEs ranging from 300 K (RT) to 800 K.

To illustrate the damaging effects of this CTE mismatch-induced strain and stress, Francis *et al.* report wafer bow measurements as large as 300 μm at room temperature for 2-inch Si-GaN-PCD composites fabricated by transfer bonding immediately prior to the removal of the sacrificial Si carrier wafer [82]. Wafer bow of this magnitude is substantially larger than the typical requirements of modern semiconductor products that stipulate less than 40 μm of wafer bow for wafers 300 mm in diameter [90]. However, Francis *et al.* have successfully produced GaN-on-PCD HEMT wafers up to 4 inches in diameter with wafer bows less than 100 μm by implementing process improvements to mitigate fracture initiation from non-uniformities and substrate defects [82]. Francis *et al.* found that the most significant sources of non-uniformity and substrate defects in their transfer bonding process were attributed to (i) residual strain in the original GaN-on-Si growth wafer (for AlGaIn/GaN heteroepitaxy), (ii) stresses induced by adhesion layers used for carrier wafer and diamond substrate attachment, and (iii) defects created in the AlGaIn/GaN heterostructure or carrier wafer during growth substrate removal (a combination of etching and grinding) [82]. Since the stress and strain accumulated during this cool-down processing step have been observed to be the predominant cause of GaN-on-PCD wafer fracture, mitigation of these stresses is critical for the realization of commercially viable GaN-on-diamond HEMTs in high-power, high-frequency applications.

Although thermomechanical modeling can be an effective tool for qualitative analysis of the stress and strain accumulated as a result of GaN-on-PCD HEMT fabrication processes, quantitative experimental measurements are necessary to accurately inspect the near-interface structural and mechanical integrity of the AlGaIn/GaN heterostructure. Advanced experimental methods such as SEM/TEM [75] and customized piezoelectric

force loading tests [91] have provided valuable qualitative insight about the interfacial structural and mechanical integrity of GaN-on-PCD composites. Furthermore, non-invasive and non-destructive Raman spectroscopy and photoluminescence experiments have been demonstrated capable of performing quantitative three dimensional (3D) biaxial stress mapping of epitaxial GaN layers to detect stress variations within AlGaIn/GaN heterostructures [18, 92]. Therefore, Raman and PL spectroscopy have been utilized in this work to perform comparative stress analyses among various GaN-on-PCD heterostructure transfer implementations.

3.2 Stress Metrology Techniques

3.2.1 Stress Metrology via Raman Spectroscopy

Raman spectroscopy, briefly introduced in Section 2.3.1, is particularly useful for characterizing temperature and mechanical stress of semiconductor heterostructures because each material's Raman spectrum is selectively sensitive to its own discrete vibrational modes that are intrinsically dependent on the strain state of the material. Hence, due to this material-specific nature and the capability of high (sub-micron) spatial resolution, Micro-Raman spectroscopy is a highly effective optical characterization technique for performing *in situ* temperature and mechanical stress measurements within the channels of AlGaIn/GaN HEMTs. In this work, all of the Raman characterization of GaN was performed in the backscattering configuration (i.e. normal to the basal plane or c-axis of the GaN heterostructure) with the laser beam incident on the (0001) surface of the GaN. In this configuration, the detectable zone-center optical phonon modes predicted by group theory for hexagonal wurtzite GaN (space group C_{6v}^4) are $E_2(\text{low})$ at $\sim 142 \text{ cm}^{-1}$,

$E_2(\text{high})$ at $\sim 568 \text{ cm}^{-1}$, and $A_1(\text{LO})$ at $\sim 735 \text{ cm}^{-1}$ [93]. As illustrated in Figure 31, the $E_2(\text{high})$ and $A_1(\text{LO})$ phonon modes of GaN correspond to atomic oscillations in the c-plane and along the c-axis of the GaN crystal lattice, respectively. In agreement with intuition, the $E_2(\text{high})$ mode frequency is much more sensitive to biaxial lattice strain (in the c-plane) than the $A_1(\text{LO})$ mode frequency [94]. The details of the complex atomic interactions and strain analysis that explain this result are presented in literature [94-97]. This distinction between the intrinsic nature of these phonon mode oscillations is significant because it enables simultaneous observation of two distinct kinds of information in response to the same temperature or biaxial strain stimulus. An example of GaN's Raman response to increased temperature and tensile biaxial strain is shown in Figure 32. Generally, an increase in temperature leads to a red shift in peak position (decreasing phonon frequency), peak linewidth broadening, and peak intensity reduction, while a decrease in temperature leads to a blue shift (increasing phonon frequency), linewidth narrowing, and intensity elevation. Similarly, tensile biaxial stress leads to red shift, while compressive biaxial stress leads to blue shift. For clarity, the terms “red shift” and “blue shift” are commonly accepted to describe a decrease in optical frequency towards the red colors of the visual spectrum and an increase in optical frequency towards the blue colors of visual spectrum, respectively.

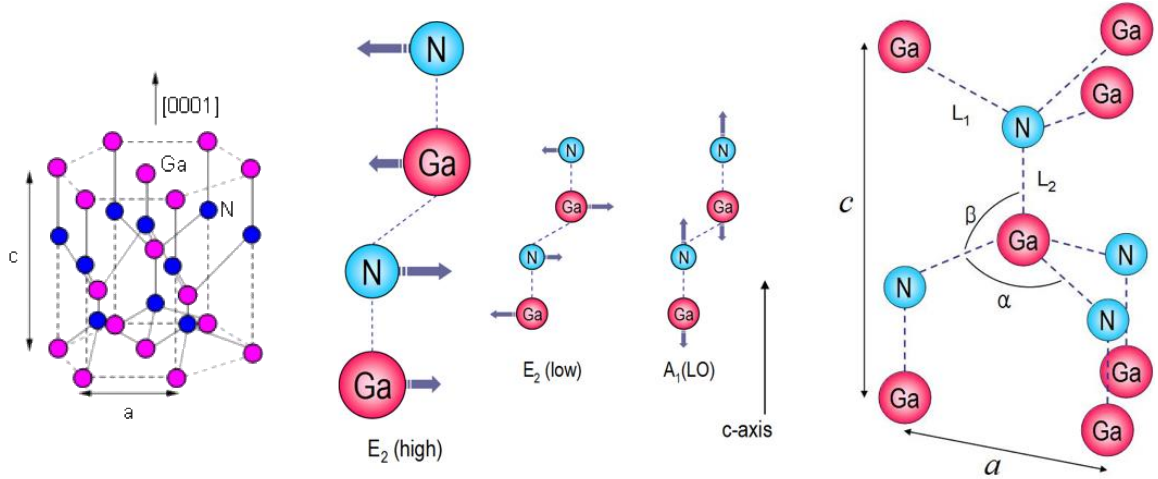


Figure 31. Crystal structure of, graphical illustration of the atomic vibration modes in, and tetrahedral bonding arrangement within hexagonal wurtzite GaN (left to right). [97]

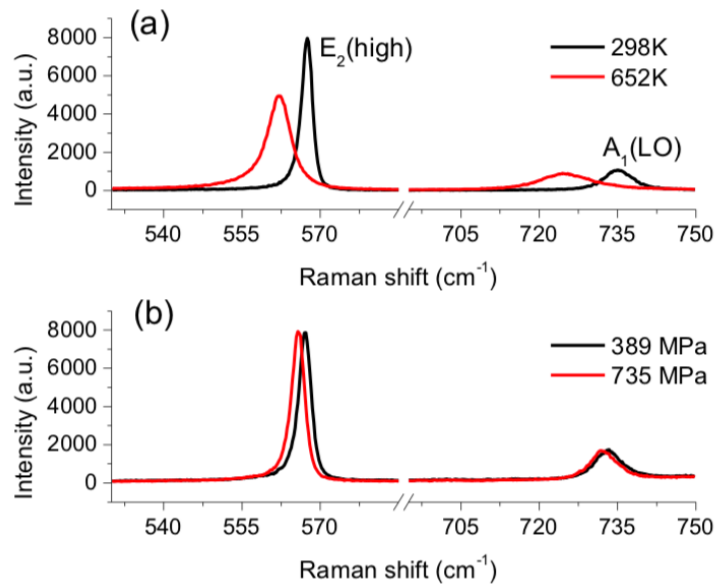


Figure 32. (a) Raman response to isothermal heating of a bulk GaN substrate, and (b) Raman response to tensile stress applied to a GaN/6H-SiC template. [97]

As presented in Section 2.3.1, the peak position method of Raman thermometry is typically used for temperature measurement due to its intrinsic nature (i.e. measurement with respect to a reference condition) and its linear calibration relation for device operating temperatures. Although using surface-deposited temperature sensors is an effective way to

circumvent thermomechanical signal biasing for temperature measurement, several methods have been presented in literature that utilize multispectral features of GaN's Raman spectrum to decouple temperature and biaxial stress without using an auxiliary material [17, 98-100]. The one stipulation required of this method is that the evolved stress in the GaN must be biaxial in the basal plane (c-plane). However, this prerequisite is often of little consequence since the stress state of thin film devices is commonly biaxial [100]. It is also important to note that stress measurements via Raman spectroscopy performed in this work represent through-thickness averages since our excitation wavelength of 532 nm is below the bandgap energy of GaN (~ 3.418 eV [18] or ~ 363 nm).

Single-peak position or linewidth-based techniques require time-consuming and error-prone temperature calibrations at each point of measurement to ensure best results. The linear two-peak fit method enables improved accuracy and time-efficiency because it utilizes the intrinsic character of the dissimilar peak position shifts of the $E_2(\text{high})$ and $A_1(\text{LO})$ phonon modes of GaN to simultaneously measure operating temperature and thermoelastic stress without a temperature calibration process. To enable calibration-free measurements, Choi *et al.* have experimentally determined the relations between temperature/stress and the frequency shifts of the $E_2(\text{high})$ and $A_1(\text{LO})$ phonon modes of GaN (see Table 3) [18, 100]. Hence, the operational temperature, T , and induced thermoelastic stress, σ , can be determined by measuring the $E_2(\text{high})$ and $A_1(\text{LO})$ peak position shifts ($\Delta\omega = \omega - \omega_o$) according to

$$(\omega - \omega_o)_{E2(\text{high})} = A_{E2(\text{high})} \cdot (T - T_o) + K_{E2(\text{high})} \cdot \sigma \quad (12)$$

and

$$(\omega - \omega_o)_{A1(LO)} = A_{A1(LO)} \cdot (T - T_o) + K_{A1(LO)} \cdot \sigma \quad (13)$$

where each ω is a measured operating condition Raman peak position, each ω_o is a measured reference (pinched OFF) condition peak position, T_o is the measured reference (pinched OFF) condition temperature, and each A and K are the linear temperature- and stress-phonon frequency relation conversion coefficients, respectively, shown in Table 3 [100]. The uncertainty of each conversion coefficient is a 95% confidence interval determined as a result of error propagation [100]. It is important to note that the reference condition used for characterizing operating temperature and thermoelastic stress must be the pinched OFF state to properly decouple these thermal effects from the electric field and inverse piezoelectric effects that are also present during device operation [16, 101].

Moreover, it is also possible to measure the residual stress state of GaN HEMT devices or GaN thin films using an adaptation of Equation 12 that requires (i) the absence of both an imposed temperature rise ($T - T_o$) and electric field (HEMT device in the zero bias state), and (ii) an accurate measure of the strain-free reference phonon frequency, $\omega_{o,sf}$, according to

$$(\omega - \omega_{o,sf})_{E2(high)} = K_{E2(high)} \cdot \sigma \quad (14)$$

Although Choi *et al.* demonstrate that Equation 13 can also be adapted to accomplish an equivalent result [18], the $E_2(\text{high})$ phonon frequency is the most suitable for residual biaxial stress measurement because it is more sensitive to biaxial stress and has a much higher Raman signal to noise ratio than the $A_1(\text{LO})$ phonon frequency (see Figure 32).

Table 3. Linear temperature and biaxial stress conversion coefficients and strain-free reference peak positions for Raman spectroscopy and photoluminescence (PL) determined from literature. The conversion coefficient subscripts denote the spectrum peak indicated in the first column. All measurement uncertainties (abbreviated as ‘Unc’) were derived from 95% confidence intervals.

Spectrum Peak	Conversion Coefficient				Strain-Free Reference	
	Temperature, A_{sp}		Biaxial Stress, K_{sp}			
	Value \pm Unc	Units	Value \pm Unc	Units	Value \pm Unc	Units
E ₂ (high)	-0.0150 \pm 0.0001 ^a	cm ⁻¹ /°C	-3.09 \pm 0.41 ^b	cm ⁻¹ /GPa	568.15 \pm 0.13 ^b	cm ⁻¹
A ₁ (LO)	-0.0281 \pm 0.0001 ^a	cm ⁻¹ /°C	-2.14 \pm 0.28 ^b	cm ⁻¹ /GPa	733.94 \pm 0.09 ^b	cm ⁻¹
PL	-		-0.0176 \pm 0.0025 ^b	eV/GPa	3.4180 \pm 0.0008 ^b	eV

^aReference [100]

^bReference [18]

3.2.2 Stress Measurement via Photoluminescence Spectroscopy

Photoluminescence is an optical emission phenomenon that is caused by the excitation and subsequent relaxation of electrons within a material in response to the absorption of photons. Photoluminescence processes in semiconductor materials occur when photons with energy exceeding the bandgap energy of the semiconductor material cause electrons to transition between the conduction and valence bands, resulting in photon emission. Since the most common electron-hole recombination that occurs in semiconductors is the interband transition of minimum energy, i.e. the bandgap energy, it is possible to directly measure the band gap of semiconductors. This process is illustrated in Figure 33 for direct and indirect bandgap semiconductor materials. Since GaN is a direct bandgap material whose bandgap energy is highly sensitive to the state of strain, photoluminescence can be used to probe the residual stress state of GaN films [18].

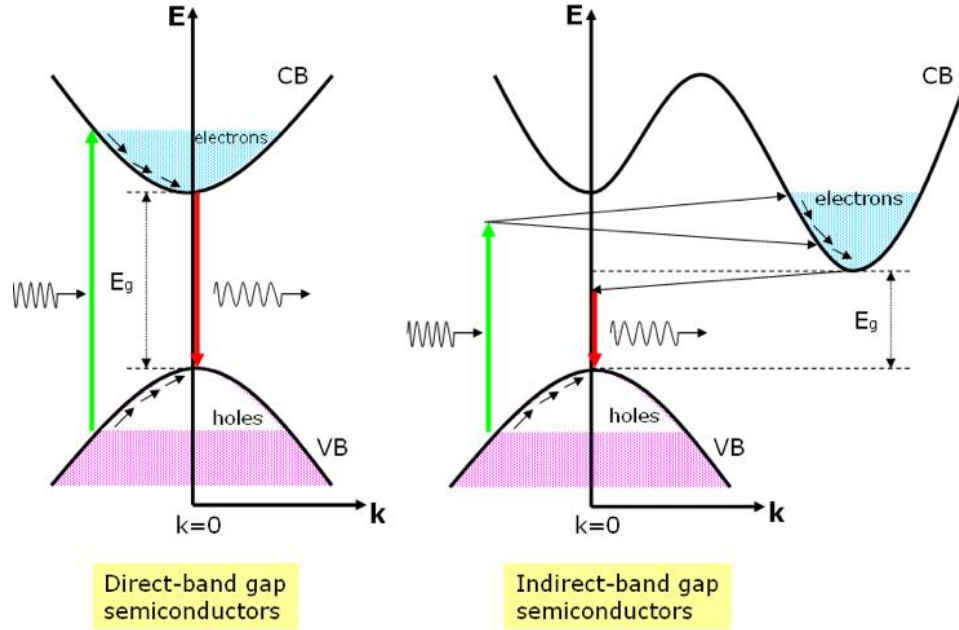


Figure 33. Photoluminescence processes in direct bandgap and indirect bandgap semiconductors. Electrons and holes created by absorption of photons are illustrated as the shaded states in the conduction band and the empty states in the valence band, respectively. Photon absorption and emission processes are illustrated by vertical arrows according to energy and momentum conservation rules. For indirect bandgap semiconductors, photon absorption and emission requires phonon absorption or emission to conserve momentum. [97]

Hence, similar to Raman spectroscopy, photoluminescence spectroscopy is a local, noncontact, and non-destructive optical characterization technique with high lateral resolution ($\sim 1 \mu\text{m}$) that is suitable for measuring the state of mechanical stress of GaN thin films and within the channels of AlGaIn/GaN HEMTs [18, 102]. As illustrated in Figure 34, tensile stress induces a red shift (decreasing bandgap energy) while compressive stress induces a blue shift (increasing bandgap energy) in the PL peak position. However, unlike the through-thickness average (of thicknesses on the order of 1-2 μm) probed with a sub-bandgap laser via Raman stress measurements, PL requires an above-bandgap laser as an excitation source that results in a near-surface stress measurement due the laser light absorption in the GaN. The photon penetration depth of the 325 nm laser used in this work

is on the order of 80-90 nm in GaN [103]. To correlate shifts in the bandgap energy of GaN via the PL peak position ($\Delta E = E - E_o$) to the biaxial stress in a GaN film, σ , the following linear correlation has been observed and reported in literature [18]:

$$E - E_o = K_{PL} \cdot \sigma \quad (15)$$

where E is the measured PL peak energy, E_o is the strain-free PL peak energy at room temperature, and K_{PL} is the PL biaxial stress conversion coefficient shown in Table 3. The PL stress conversion coefficient and strain-free reference peak energy were determined by Choi *et al.* using a 325 nm He-Cd laser with a 3 μ W laser power incident on the GaN samples to minimize laser induced local heating [18]. Although minimal sample heating was still detectable at this laser power, further power reduction is impractical for GaN sample characterization due to excessive signal accumulation times. However, Choi *et al.* observed that the small PL peak shift induced by local heating at this laser power maintained a constant value and is implicitly included in the empirically determined strain-free PL peak energy, E_o [18]. Therefore, it is critical to replicate this power condition to ensure accuracy of stress results obtained using their published K_{PL} and E_o . Moreover, stress measurements on GaN devices under voltage bias using this E_o may lead to inaccurate results due to non-stress-related PL peak energy biasing [18].

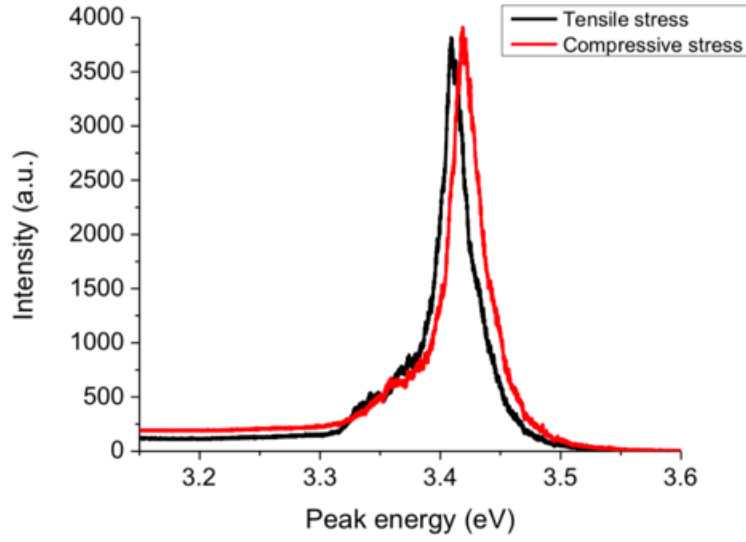


Figure 34. Room temperature PL spectra of GaN epitaxial films under tensile (GaN/6H-SiC) and compressive (GaN/4H-SiC) stress. [97]

3.3 Sample Details and Experimental Apparatus

3.3.1 Sample Details

The four GaN-on-PCD samples examined in this work are shown in Figure 35 were taken from a total of wafers fabricated according the two pre-grown AlGaIn/GaN heterostructure transfer technique alternatives: (i) direct growth (wafers G1 and G2) and (ii) wafer bonding (wafer B) of a PCD substrate onto the GaN-side of an AlGaIn/GaN heterostructure. The final material composition details of wafers G1, G2, and B are illustrated in Figure 36.

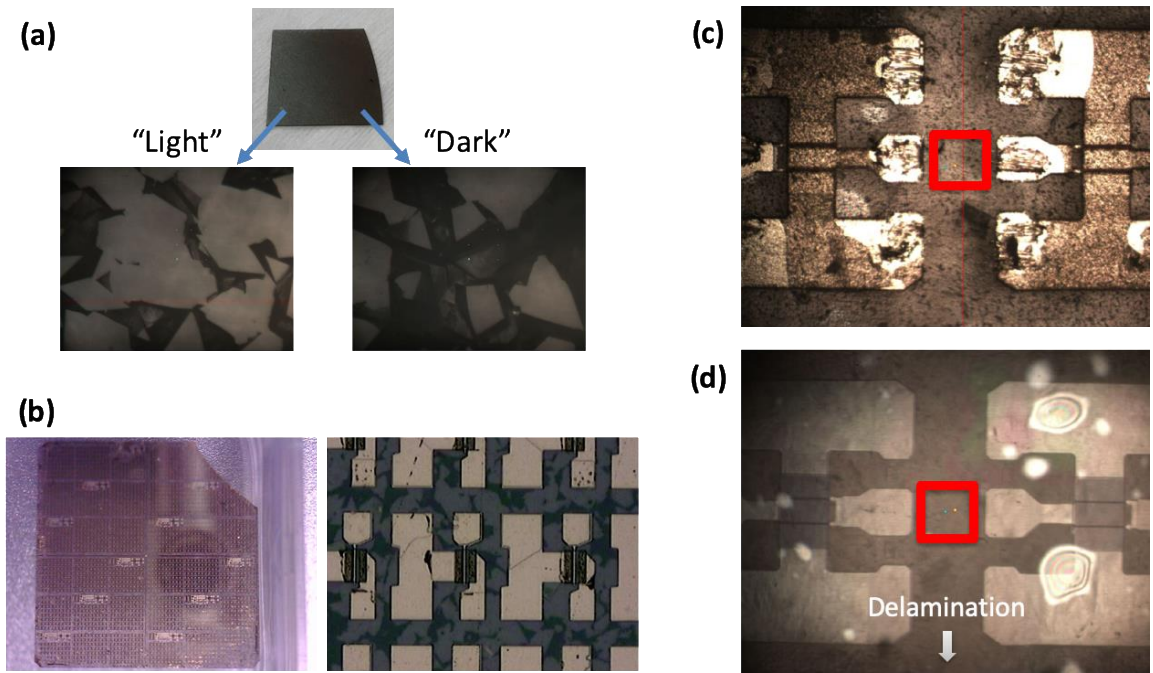


Figure 35. Microscope images of the (a) bare and (b) HEMT-processed die from wafer G2 and the (c) topside and (d) backside of approximate region measured located between adjacent HEMT devices on wafer B. Stress measurements collected from the G2 bare die were collected on a “light” region away from the wafer periphery. The location of the delamination that is shown in Figure 44 is denoted in (d).

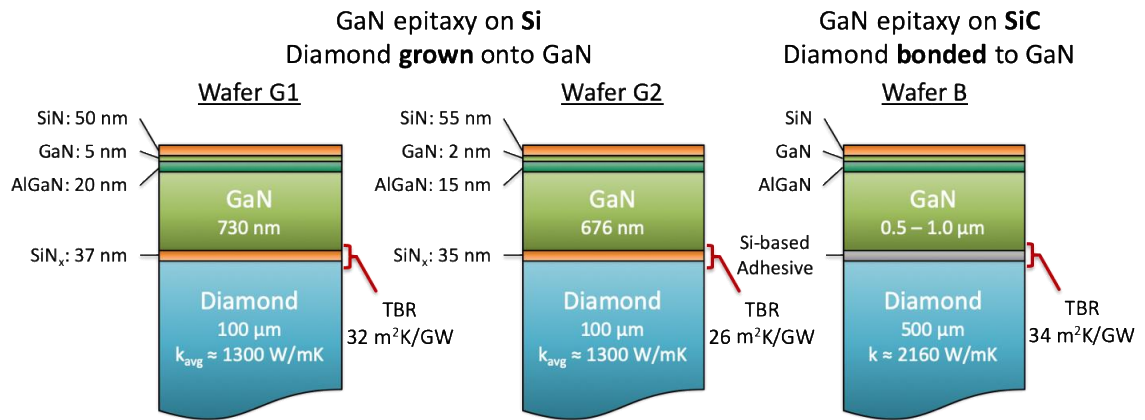


Figure 36. Material composition details of the grown GaN-on-PCD wafers G1 and G2, and the bonded GaN-on-PCD wafer B.

Wafer G1 was a 75 mm GaN-on-PCD wafer prepared by Element Six that was fabricated according to a direct growth heterostructure transfer technique that has been the

subject of several prior thermal and structural studies presented in literature [76, 92, 104]. First, the 755 nm thick $\text{Al}_{0.26}\text{Ga}_{0.74}\text{N}/\text{GaN}$ heterostructure was grown on Si (111) via metal-organic chemical vapor deposition (MOCVD). Next, a 50 nm layer of silicon nitride (SiN) was deposited on the exposed heterostructure as a protective adhesion layer for bonding the GaN-on-Si composite to a temporary Si carrier wafer. Then the Si (111) growth substrate and transition layers were then removed and a 37 nm amorphous silicon nitride (SiN_x) adhesion layer was deposited to facilitate diamond seeding and subsequent PCD growth via MWCVD to a substrate thickness of 100 μm . Finally, the temporary Si carrier was removed to produce the completed GaN-on-diamond composite depicted in Figure 36.

Wafer G2 was a second 75 mm GaN-on-PCD wafer prepared by Element Six that was fabricated according to a similar direct growth heterostructure transfer technique that underwent proprietary process improvements to eliminate voids that were detected at the GaN-PCD interface of wafer G1. Two 16 x 16 mm diced wafer fragments from wafer G2 were examined in this work. The first sample taken from wafer G2 was a bare (unprocessed) die and the second sample taken from wafer G2 was processed into HEMT test devices ($L_G = 3 \mu\text{m}$, $L_{GD} = 10 \mu\text{m}$, $W_G = 75 \mu\text{m}$) by the U.S. Naval Research Laboratory (NRL) utilizing standard processing techniques that are detailed in literature [105].

Wafer B was a 1 inch (~25 mm) GaN-on-PCD wafer prepared and processed into HEMT test devices by BAE Systems that was fabricated according to a low-temperature wafer bonding heterostructure transfer technique that has been reported in literature [29]. This device-first process began with device fabrication on GaN-on-SiC epitaxial wafers as a part of a standard dual field-plate GaN device process [106]. The completed GaN-on-SiC device wafer was then bonded to a temporary carrier wafer to facilitate removal of the SiC

growth substrate via a plasma etch process selective to GaN [29]. The subsequently exposed bottom surface of the AlGaIn/GaN heterostructure was further etched and chemical-mechanical polished to less than 1 nm RMS surface roughness in preparation for wafer bonding [29]. The low-temperature bond was achieved by depositing a thin layer of Si-based bonding adhesive to the polished GaN and free-standing PCD surfaces, mating the prepared surfaces at room temperature, and curing the adhesive bond layer at a (proprietary) temperature below 150 °C [29]. Finally, the temporary carrier wafer was removed to complete the bonded GaN-on-diamond HEMT device wafer.

3.3.2 Experimental Apparatus

The Raman and PL spectroscopy measurements of residual stress in the GaN epitaxial films were performed using a Horiba Jobin Yvon LabRAM HR800 spectrometer system. A 532 nm diode-pumped solid-state laser and a 325 nm He-Cd laser were used as excitation sources for the Raman and PL measurements, respectively. The 532 nm and 325 nm laser powers incident on the measurement samples were adjusted via a series of neutral density filters to 25 mW and 3 μ W respectively. Localized sample heating caused by laser light absorption was averted using the 532 nm laser since its excitation energy is below the bandgap of GaN and diamond. Although the excitation energy provided by the 325 nm laser is above the bandgap of GaN, the reduced laser power minimized localized sample heating as discussed in the preceding Section 3.2.2. An Olympus LMPlanFl 50x LWD objective (NA = 0.50 and WD = 10.6 mm) was used with the 532 nm laser for Raman measurements and a Thorlabs LMU-39x-NUV objective (NA = 0.50, WD = 2 mm) was used with the 325 nm laser for PL measurements. The theoretical diffraction limited laser

focused spot sizes were 1.3 μm and 0.79 μm for the Raman (532 nm) and PL (325 nm) measurements, respectively, determined according to

$$d = \frac{1.22\lambda}{NA} \quad (16)$$

where d is the spot size (diameter), λ is the laser wavelength, and NA is the numerical aperture of the microscope objective [97].

Prior to Raman and PL measurements, the spectrometer was calibrated at room temperature with a piece of bulk 4H-SiC by establishing the $E_2(\text{PO})$ phonon frequency ($\sim 777 \text{ cm}^{-1}$) [107] as a reference with nominal value of $776.599 \pm 0.001 \text{ cm}^{-1}$, as was done by Choi *et al.* [18] in their procedure to derive the biaxial stress-phonon frequency correlation implemented in this work. Furthermore, it is prohibitively difficult to acquire the commonly used Si phonon frequency ($\sim 522 \text{ cm}^{-1}$) [108] with sufficient signal to noise ratio when the laser powers of the 532 nm and 325 nm lasers used in this work are properly derated to prevent localized absorptive laser heating. Raman and PL measurements were fit to a pseudo-Voigt function (linear combination of Gaussian-Lorentzian functions) to extract the peak position, intensity, and FWHM of each spectrum peak. Although each Raman spectrum peak of interest can be fitted with a single peak, the full line shape of the near-edge emission of the GaN PL spectrum [93] must be fitted with multiple peaks to properly determine the peak position corresponding to the GaN bandgap energy as illustrated in Figure 37. The best estimate of each spectral feature (peak position, FWHM and intensity) and its uncertainty were determined as the sample mean and 95% confidence interval about the sample mean calculated from a sample size of 20 spectrum acquisitions.

Data acquisition times were adjusted to obtain consistent Raman and PL intensity counts of ~8000 and ~4000 respectively. Intensity reduction below half of these targets was indicative of unreliable data due to insufficient signal to noise intensity ratio.

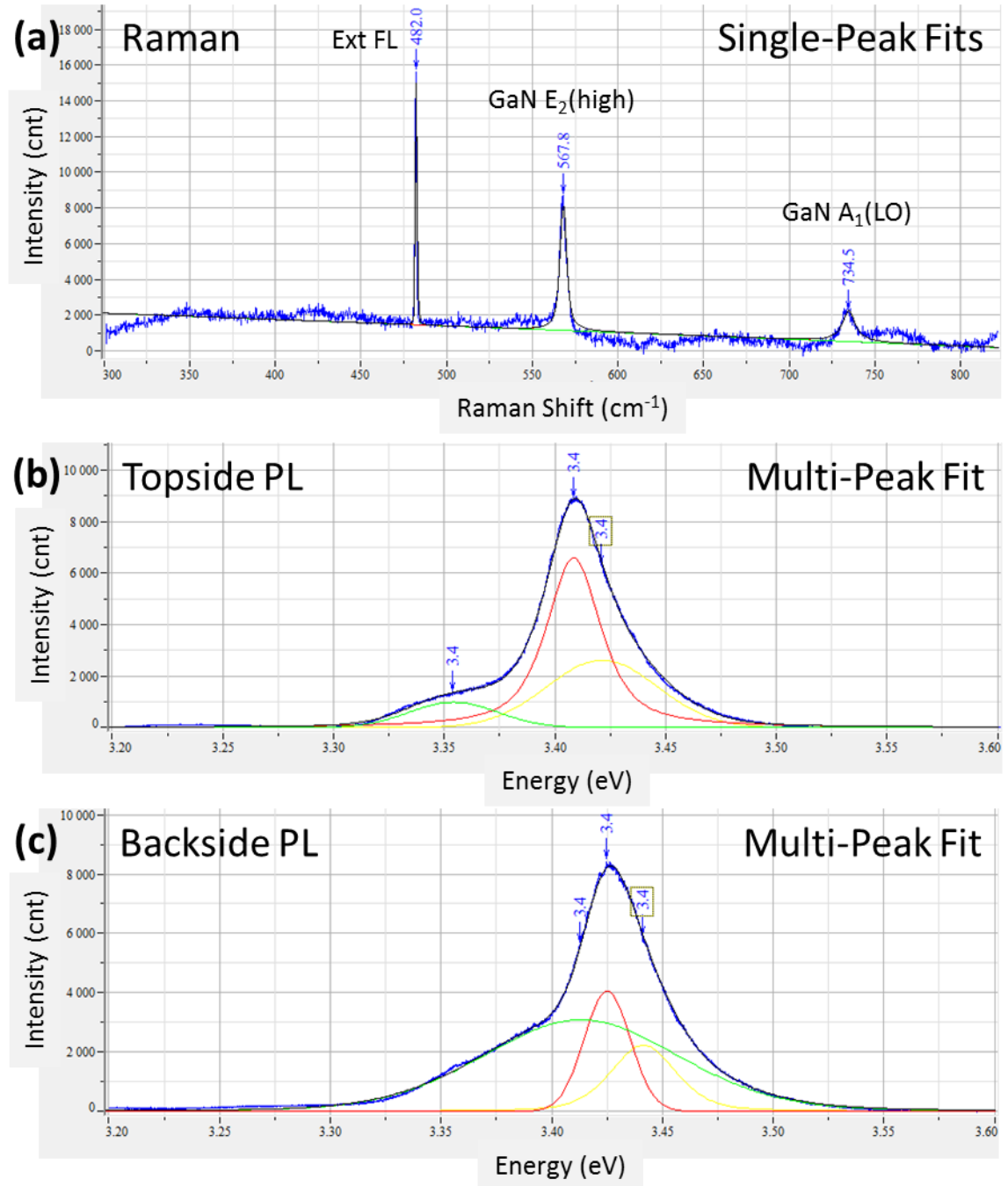


Figure 37. (a) Raman, (b) topside PL, and (c) backside PL measured from the GaN buffer layer within the gate-drain access region of the GaN-on-diamond HEMT from wafer G2. Each Raman peak was fitted with a single pseudo-Voigt line shape, whereas each PL peak was fitted with multiple (three) pseudo-Voigt line shapes.

The spectrometer was configured for both lasers to maximize spectral resolution while maintaining reasonable acquisition time according to the following specifications:

an 800 mm focal length, a 100 μm confocal hole size, an 1800 groove/mm diffraction grating, and a liquid N_2 cooled charged-coupled device (CCD) detector with 2048 x 5000 pixels. This spectrometer configuration resulted in spectrometer resolutions of $0.28 \text{ cm}^{-1}/\text{pixel}$ and $0.82 \text{ cm}^{-1}/\text{pixel}$ ($1.0 \times 10^{-4} \text{ eV}/\text{pixel}$) of the CCD for the 532 nm and 325 nm lasers, respectively. However, a significant consequence of this high-resolution configuration is the increased susceptibility of the spectrometer to systematic drift (error) caused by ambient room temperature fluctuations. To correct for this spectrometer drift, an external fluorescence source was used as a reference throughout the duration of the Raman measurements. When the spectrometer is configured to measure Raman shifts from the 532 nm excitation wavelength, the constant, spectrometer-independent fluorescence peak is visible at $\sim 482 \text{ cm}^{-1}$ (see Figure 37). Monitoring the shift of this external fluorescence peak enables a direct measurement of the spectrometer drift in time. Hence, by measuring the Raman shifts of the GaN $\text{E}_2(\text{high})$ and $\text{A}_1(\text{LO})$ phonon frequencies and the external fluorescence simultaneously, it is possible to accurately account for and correct spectrometer drift that evolves throughout the duration of a Raman experiment. Figure 38 illustrates the spectrometer drift accumulated throughout ~ 8 hours of Raman measurements of the 4H-SiC reference sample. Spectrometer drift correction is not required for PL measurements since the magnitude of typical spectrometer drift ($< 0.3 \text{ cm}^{-1}$ or $4 \times 10^{-5} \text{ eV}$) is negligible with respect to the strain-free bandgap of GaN ($E_o = 3.4180 \pm 0.0008 \text{ eV}$) the extended spectral range used for PL measurements of GaN (3.15 – 3.6 eV). To ensure spectrometer drift accumulated throughout PL spatial mapping measurements lasting up to ~ 12 hrs depending on the spatial sampling density, the residual stress of a bulk GaN substrate was measured via PL immediately before and after each PL spatial mapping

measurement. These precautionary bulk GaN reference measurements were precisely self-consistent (within typical PL measurement uncertainty of ± 50 MPa).

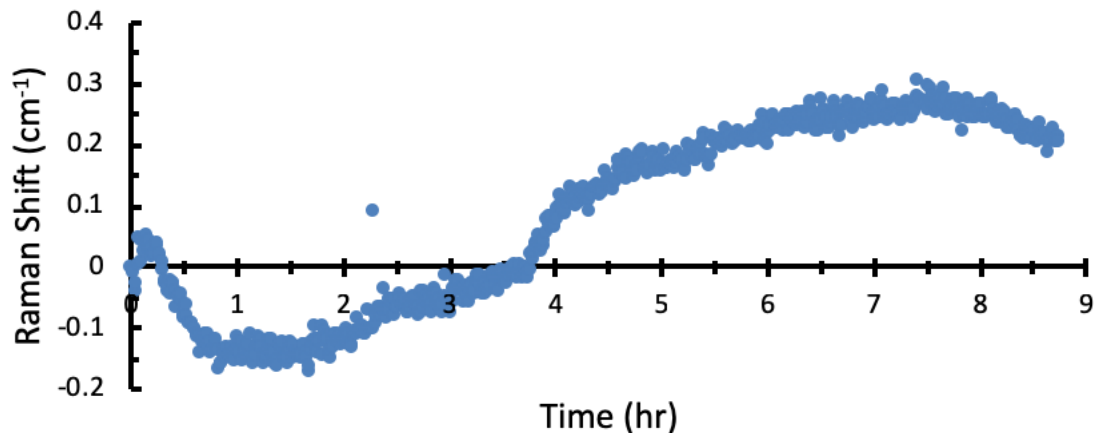


Figure 38. Spectrometer drift accumulated throughout ~8 hours of Raman measurements of the 4H-SiC reference sample used for system calibration.

3.4 Results and Discussion

3.4.1 3D Stress Mapping of GaN

A comparative analysis between GaN-on-diamond wafers fabricated according to different heterostructure transfer methods was performed to investigate the through-thickness variations of the residual biaxial stress state in the AlGaIn/GaN heterostructure accumulated by each wafer fabrication process. This was accomplished by examining the residual stress of the GaN buffer layer of each AlGaIn/GaN heterostructure using a combination of the Raman and PL stress metrology techniques introduced in Section 3.2.

Since GaN is transparent to the 532 nm laser used for the Raman measurements, the residual stress measurements derived from the Raman spectrum of the GaN buffer layer are averages of the residual stress state through the full thickness of the GaN buffer layer

(~730 – 1000 nm). On the other hand, GaN is opaque to the 325 nm laser used for the PL measurements with a penetration depth of 80 – 90 nm. Therefore, the residual stress measurements derived from the PL spectrum of the GaN buffer layer are near-surface averages of the residual stress state through the first 80-90 nm of GaN. Furthermore, since high quality diamond is transparent to the 325 nm laser used for the PL measurements it was possible to measure the near-surface residual stress state on the diamond-side of the GaN buffer layer. Hence, as illustrated in Figure 39, the combination of topside PL, topside Raman, and backside PL measurements enabled characterization of the residual stresses in the GaN buffer layer near the AlGaIn-GaN interface (denoted as the *top* value), throughout the GaN (denoted as the *avg* value), and near the GaN-diamond interface (denoted as the *back* value).

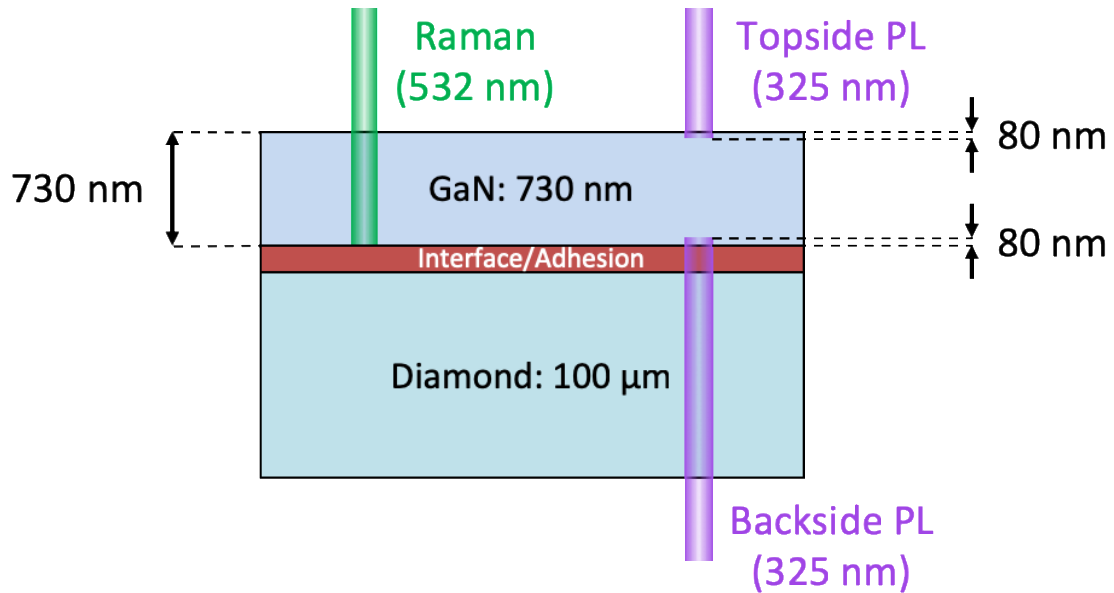


Figure 39. Schematic of Raman and photoluminescence stress metrology technique.

The stress measurement results collected from wafers G1, G2, and B are summarized in Figure 40. Each Raman and PL stress result collected from wafers G2 (bare

die) and B is a spatially-averaged mean value calculated from a 2D mapping of a $50 \times 50 \mu\text{m}$ area in the basal plane incremented by $5 \mu\text{m}$ (total of 25 measurements). The error bars about each stress result is the spatially-averaged mean value of the 25 individual stress measurement uncertainties. Each individual stress measurement uncertainty (of the 25-measurement map) was determined by applying the analytical propagation method described in Section 2.4.2 applied to Equations 13 and 14 for Raman and PL measurements (see Section 3.3.2), respectively. The spatial variability measured within each $50 \times 50 \mu\text{m}$ area was nearly equal to each spatially-averaged mean uncertainty. Unlike the stress results collected from wafers G2 and B, the Raman stress result from wafer G1 is a spatially-averaged mean value calculated from 14 measurements spanning the entire 75 mm wafer distributed according to Figure 41, and each PL stress result from wafer G1 was measured from a single location at the wafer center as shown in Figure 41. The Raman and PL measurements collected from wafer G1 are unpublished measurements performed by Georgia Tech graduate student, Luke Yates.

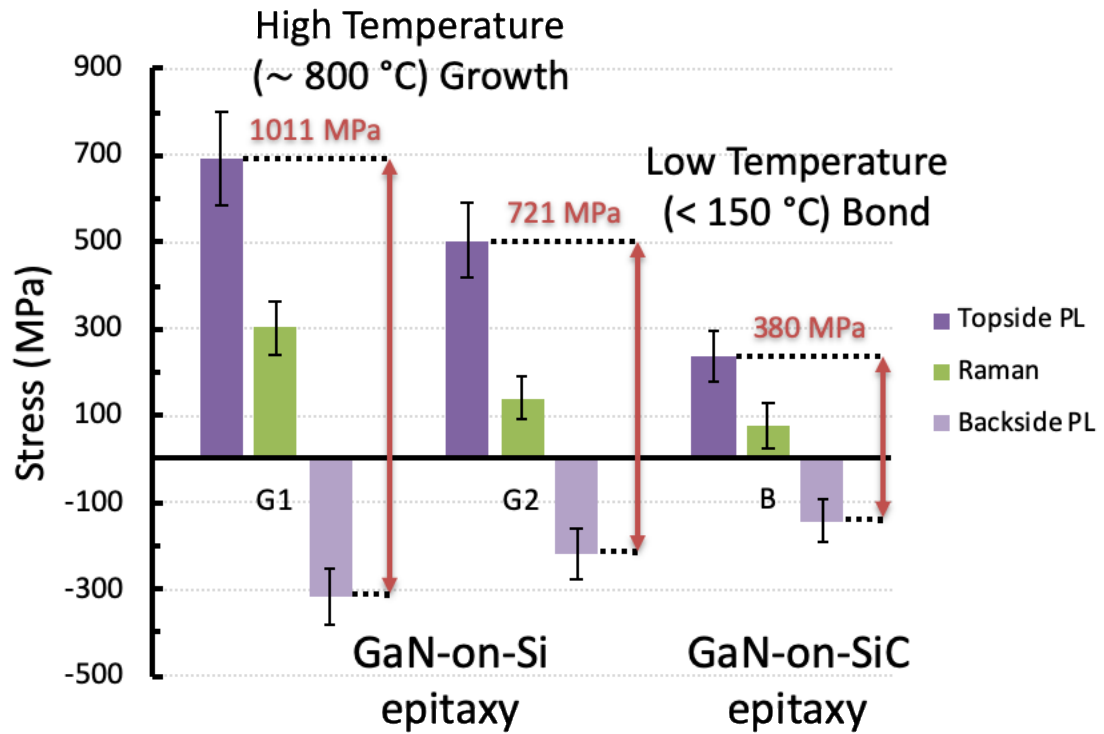


Figure 40. Residual biaxial stress in the GaN buffer layer of AlGaIn/GaN heterostructures of GaN-on-diamond wafers G1, G2, and B measured via Raman and PL spectroscopy. The red data labels correspond to the magnitude of the stress gradient measured across the GaN layer of each wafer sample.

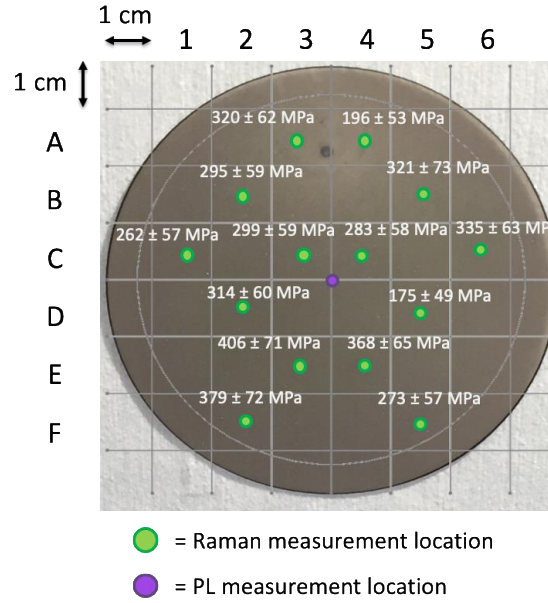


Figure 41. Wafer G1 Raman and PL measurement locations for assessing cross-wafer stress uniformity.

The stress measurement results collected from the HEMT-processed die taken from wafer G2 are shown in Figure 42 and were in precise agreement to the stress results measured from the bare die from wafer G2 (see Figure 40). Similar to the bare die, each Raman and PL stress result collected from the HEMT-processed die is a spatially-averaged mean value calculated from a 2D mapping of the 5 x 60 μm (length x width) gate-drain access region shown in Figure 35 incremented by 1 and 5 μm along the gate-drain length and width respectively. Figure 42 also illustrates the spatial variability measured within the 5 x 60 μm gate-drain access region. It was observed that the quality of the backside PL stress results depended on the diamond grain orientation at the point of measurement. As observed in Figure 43, the measurement results with diminished PL intensity correlate with measurements collected from regions of the sample that appear dark when illuminated by white light. These dark regions have been considered to be regions where the incident light is not effectively backscattered, thereby limiting the ability to detect PL emissions.

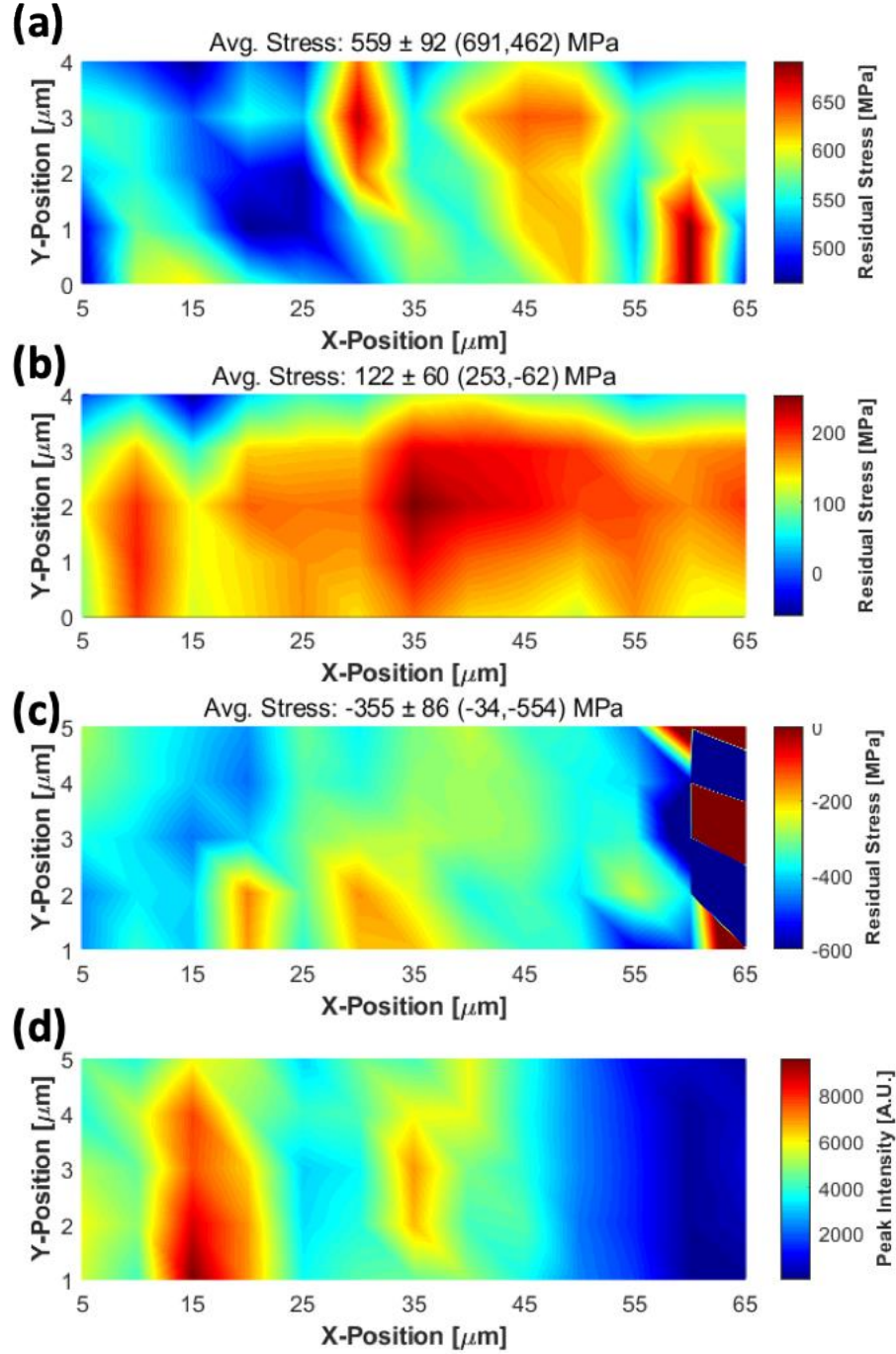


Figure 42. Spatial maps of the (a) topside PL stress, (b) Raman stress, and (c) backside PL stress and (d) peak intensity measured from the GaN buffer layer located within the gate-drain access region of a GaN-on-diamond HEMT from wafer G2 shown in Figure 35. The stress extrema shown in the right side of (c) are artifacts of insufficient PL peak intensity as shown in (d). The annotations above (a), (b), and (c) indicate the spatially-averaged mean \pm uncertainty (max, min).

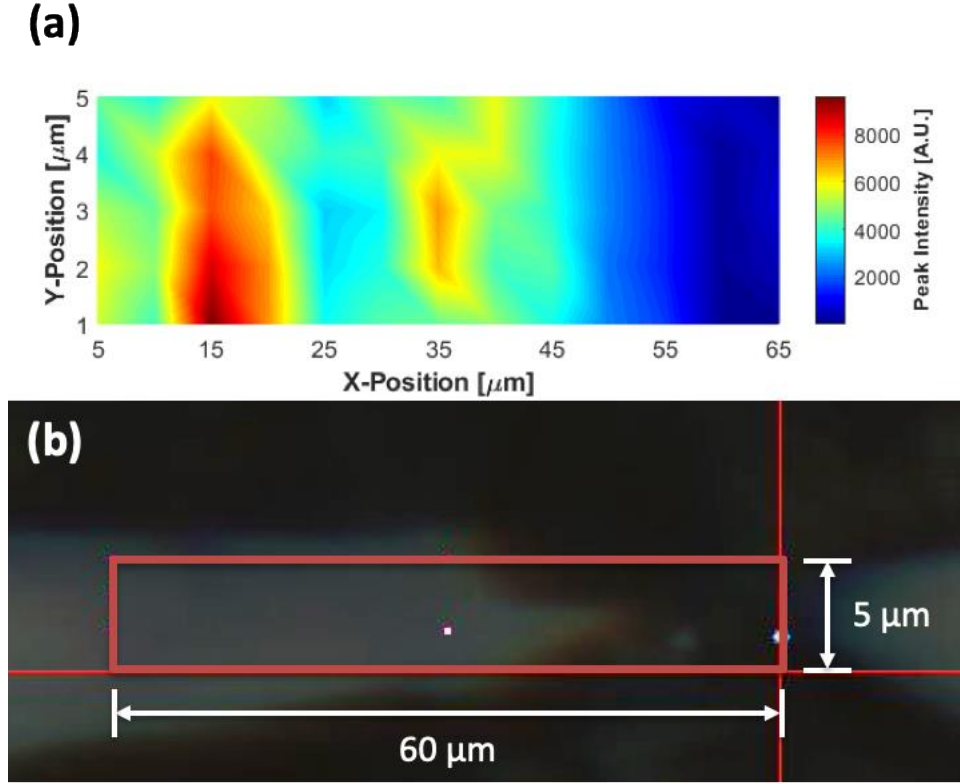


Figure 43. (a) Spatial map of the backside PL peak intensity and (b) microscope image of the backside of the 5 x 60 μm gate-drain access region (boxed) when illuminated by white light.

In addition, a localized delamination at the transfer bonded GaN/PCD interface that was visible on wafer B was examined via the Raman and PL stress metrology techniques. The stress measurements across the delamination were collected from a line scan spanning 200 μm as illustrated in Figure 44 and incremented by 10 μm (21 measurement locations). The stress and uncertainty results collected from each measurement location are the mean value and 95% confidence interval calculated from 10 repeated acquisitions. The Raman and PL stress measurement results from this line scan are shown in Figure 44 and demonstrate that the presence of the delamination has significant effects on the stress state of the GaN, namely increasing the magnitude of the through-thickness stress gradient. GaN/PCD interface delamination near active HEMT channels would likely exacerbate

material degradation due to the localized stress concentration. Furthermore, GaN/PCD interface delamination would also severely diminish heat dissipation, compounding thermal management and reliability challenges facing AlGaN/GaN HEMTs used in high-power RF electronics.

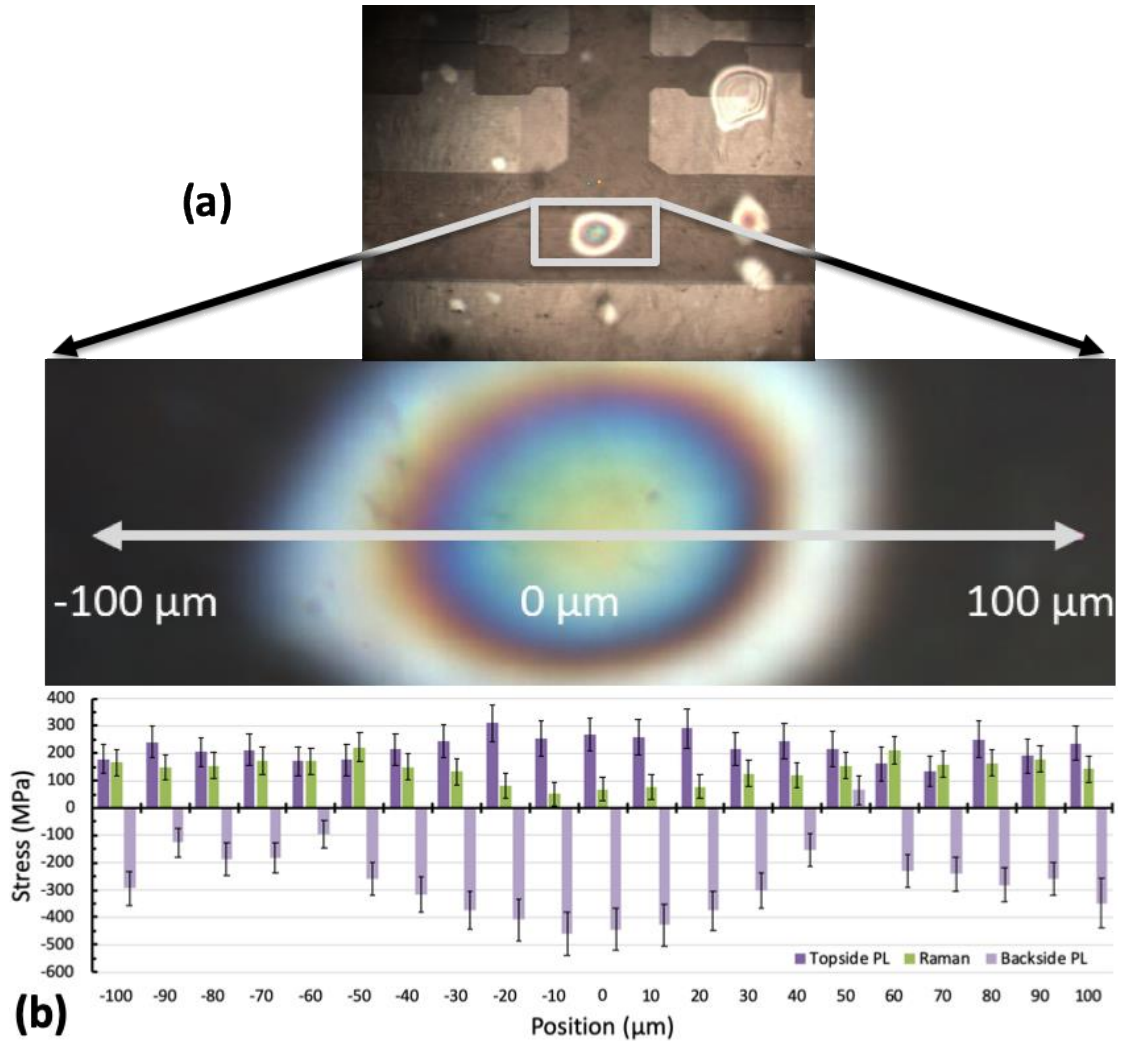


Figure 44. (a) Microscope images of the delamination at the transfer bonded GaN/PCD interface of wafer B captured from the backside of the wafer. Raman and PL stress measurements across the delamination were collected along the 200 μm line annotation. Note that the delamination is just beyond the field of view captured in the microscope images of the same devices shown in Figure 35. (b) Raman and PL stress measurement results of the delamination line scan.

The Raman stress results collected from wafer G1 demonstrated reasonable cross-wafer uniformity with a spatially-averaged mean and standard deviation of 302 ± 64 MPa that are in close agreement with literature that reported a spatially-averaged mean and standard deviation of 320 ± 100 MPa according to similar Raman stress mapping measurements collected from the same exact GaN-on-diamond wafer using a 514.5 nm

laser [92]. As shown in Figure 40, the topside and backside PL stress results measured from all three wafers indicate the presence of a topside to backside transition from tensile to compressive stress across each GaN buffer layer thickness that are all approximately 730 nm thick. Since the main difference between wafers G1 and G2 was the heterostructure transfer process improvement intended to mitigate voiding and near-interface defects, it follows that the improved interface quality resulted in a reduction in the residual stress magnitude throughout the GaN layer. It is also of note that the residual stresses measured from wafer B were significantly lower in magnitude than those measured from wafers G1 and G2. Although causality has been considered in the ensuing discussion, it is difficult to distinguish whether the GaN-on-SiC heterostructure epitaxy or the low temperature wafer bond is responsible for this result. In addition, the decreasing trend in the magnitude of the residual stresses observed from the progression of GaN-on-PCD wafers G1 to G2 to B is particularly interesting since the substrate induced residual stress in the GaN layer of AlGaIn/GaN HEMTs has been demonstrated to be a decisive factor that impacts device reliability under high bias conditions [10]. Therefore, in order to further develop GaN-on-PCD processes for optimal HEMT device performance, it is critical to identify the most structurally adverse process steps.

Due to the multistep process for fabricating GaN-on-PCD wafers that involves several temperature excursions during sequential heteroepitaxy and/or wafer bonding, accurately distinguishing the component sources of the final accumulated residual stress state is not straightforward and would ideally involve GaN stress measurements after every significant process step. Since the stress measurements presented in this work were only able to be performed after GaN-on-PCD wafer fabrication was completed, we lean on

comparative analyses between wafer samples G1, G2, and B to elucidate means for improving GaN-on-PCD processes. Given the presumption that the predominant residual stress in each GaN-on-PCD wafer was accumulated during a combination of (i) the heteroepitaxy of the AlGaIn/GaN heterostructure and (ii) the cool-down step following PCD growth or bonding and before the removal of the temporary carrier wafer, it follows that the accumulated stress state of the thin GaN layer is comprised of (i) the intrinsic stress state developed during the GaN heteroepitaxy and (ii) the thermal stresses evolved during the cool-down step due to CTE-mismatched interfaces.

In prior work that examined the cross-wafer uniformity and vertical stress gradient within the GaN buffer layer of wafer G1 via 3D Raman stress mapping [104], the vertical stress gradient was attributed to stress relaxation along the GaN epitaxial growth direction caused by threading dislocations formed during GaN heteroepitaxy. Hancock *et al.* verified the presence of a higher density of threading dislocations along the backside (GaN-diamond) of the GaN than along the topside (AlGaIn-GaN) with TEM images as shown in Figure 45 and incorporated the dislocations into an FEM by introducing a scaling factor that reduced the un-strained elastic modulus of GaN to simulate relaxation effects [104]. Although stress relaxation in the GaN during heteroepitaxy on the original silicon (111) substrate has sufficiently explained the tensile stress relaxation observed in wafer G1, the same explanation fails to account for the transition beyond the stress-free equilibrium to a state of compressive stress that we have observed from the same wafer G1. Moreover, since compressive stress was measured in GaN that was originally grown on both Si (wafers G1 and G2) and SiC (wafer B), it follows that the compressive stress was accumulated after GaN epitaxy and therefore during heterostructure transfer processes, namely the cool-down

step following direct growth of or wafer bonding to PCD and before the removal of the temporary carrier wafer.

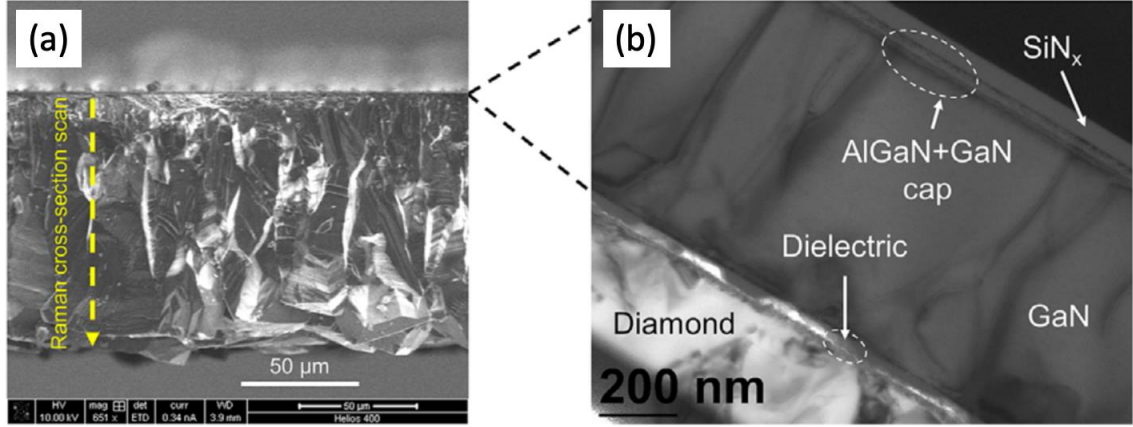


Figure 45. (a) SEM image of cleaved GaN-on-diamond wafer G1 and (b) TEM image of the wafer G1 cross-section at the GaN-diamond interface as published in literature [92]. The higher dislocation density along the backside (GaN-diamond) of the GaN can clearly be seen in (b).

Although it is possible to coarsely simulate the effects of thermal expansion at each major step of the AlGaIn/GaN heterostructure transfer process, such models are limited in their ability to capture near interface structural mechanics and often explicitly exclude changes to interface structure that occur during intermediate processing steps such as etching and polishing. For example, the FEM developed by Hancock *et al.* incorporated stress relaxation effects and temperature dependent CTEs in an attempt to recreate the predominant effects of thermal expansion [104]. Although the results of their FEM demonstrated reasonable agreement with the average and topside experimental stress results via Raman and PL spectroscopy respectively, their backside UV Raman and PL stress results of the GaN near the GaN-PCD interface did not match compressive stress in the diamond predicted by their model as shown in [92]. In addition, the model is necessarily limited to distinguishing only two distinct stress states within the GaN layer

[92]. In fact, the backside PL stress result of -316 ± 63 MPa in the GaN near the GaN-PCD interface presented in this work has demonstrated better agreement with the compressive stress in the diamond predicted by their FEM (-500 MPa) than their measured value of 50 ± 190 MPa as illustrated in Figure 46 [92]. Therefore, due to the FEM's structural simplicity and the limited experimental stress data measured at intermediate process steps, only general trends that follow idealized thermal stress theory in multilayered structures can be deduced from such an FEM. The primary advantage of an FEM over analytical theory is the ability to include the temperature dependent CTEs of GaN, silicon, and CVD diamond that are shown in Figure 30 and have been demonstrated necessary for sensible model results [109, 110]. Additional discussion of the complexities that accompany finite element modeling PCD growth on silicon (111) and AlGaIn/GaN heterostructures can be found in literature [109, 110]. Therefore, despite the shortcomings of existing efforts to incorporate the complex multistep AlGaIn/GaN heterostructure transfer processes for GaN-on-diamond fabrication into a comprehensive FEM, the efficacy and utility of 3D stress mapping via Raman and PL spectroscopy have been demonstrated by experimental results from three distinct GaN-on-PCD wafers.

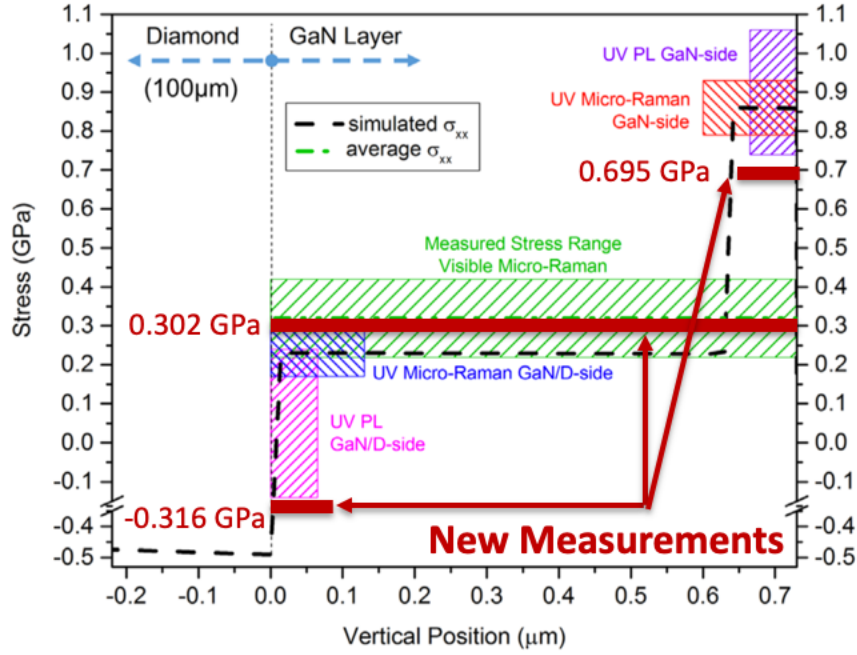


Figure 46. Experimental and finite element simulation stress results as a function of vertical position along the cross-section of wafer G1 published by Hancock *et al.* [92]. New Raman and PL stress measurements presented in this work are superimposed in red over the literature data.

3.4.2 Steady-State Thermal Modeling: PCD Substrates Compared

In order to illustrate the thermal merits of the advanced GaN-on-PCD fabrication techniques presented in this work, a comparative analysis has been performed using a steady-state thermal FEM of a typical high-power, high-frequency AlGaIn/GaN HEMT device. The steady-state thermal analysis that follows consists of (i) the simplifying assumptions necessary to incorporate a TriQuint TGA2814 GaN-on-SiC power amplifier into a steady-state thermal FEM in Section 3.4.2.1, (ii) the validation procedure used to appropriately reference the steady-state operating temperature of the TGA2814 power amplifier reported by the manufacturer, and (iii) the results of the comparative thermal resistance analysis that illustrates the thermal performance benefits of the direct growth and wafer bonded GaN-on-PCD implementations.

3.4.2.1 Model Details and Assumptions

The FEM consisted of a TriQuint TGA2814 GaN-on-SiC power amplifier (GPA) that was mounted to a molybdenum-copper (Mo/Cu) composite heat sink via a eutectic gold/tin (Au//Sn) solder alloy. This GPA is an electrical circuit used in RF communications that operates in high power conditions and whose functional units are AlGaIn/GaN HEMTs. Figure 47 along with additional manufacturer-specified data for TGA2814 were used as the basis for the FEM geometry and boundary conditions [111]. The full dimensions of the GPA were 5.41 x 5.19 x 0.1 mm and the substrate, die-attach, and Mo/Cu heat sink layer thicknesses were 100 μm , 38 μm , and 508 μm respectively [111]. The assumed ambient boundary conditions were free convection ($h = 5 \text{ W/mK}$) and black body radiation ($\varepsilon = 1$) from the exposed surfaces (top of the geometry). A constant temperature (Dirichlet) boundary condition was imposed at the bottom surface of the Mo/Cu base of the FEM. The magnitude of this constant temperature boundary condition was maintained at 22 °C for the comparative analysis and raised to 85 °C for the model validation analysis to match the device manufacturer specifications. The TGA2814 shown in Figure 47 has been incorporated into a FEM by making the following assumptions:

- 1) The arrays of HEMTs (outlined in Figure 47) have been treated as rectangular heat sources that are responsible for the heat dissipation resulting from device operation. Heat dissipation was uniformly sourced to the rectangular regions via surface heat flows. This assumption has been shown in literature to be valid under fully-open channel operating conditions for moderate drain bias since Joule-heating is uniform [65, 112].

- 2) Heat dissipation was distributed uniformly according to total channel length, a summation of all individual channel lengths. The number of active channels and their respective channel lengths were approximated by counting and visual inspection respectively from Figure 47. According to these approximations, 15.5% of the heat dissipation was attributed to Region 1 (R1) and the remaining 84.5% of the heat dissipation was attributed to Region 2 (R2).
- 3) The GaN and substrate layers were assumed to be 1 μm and 100 μm in thickness. SiC is the substrate material of the TGA2814 GPA, however grown and bonded PCD were alternatives considered in the comparative analysis in Section 3.4.2.3.
- 4) The thermal conductivity of materials and GaN-substrate thermal boundary resistances (TBR_{eff}) were taken from literature and are listed in Table 4.
- 5) Half-symmetry was employed about the ZX plane (shown in Figure 47) to reduce the computational domain. Hence, the heat dissipation conditions input to the FEM were also half of their full-scale values.

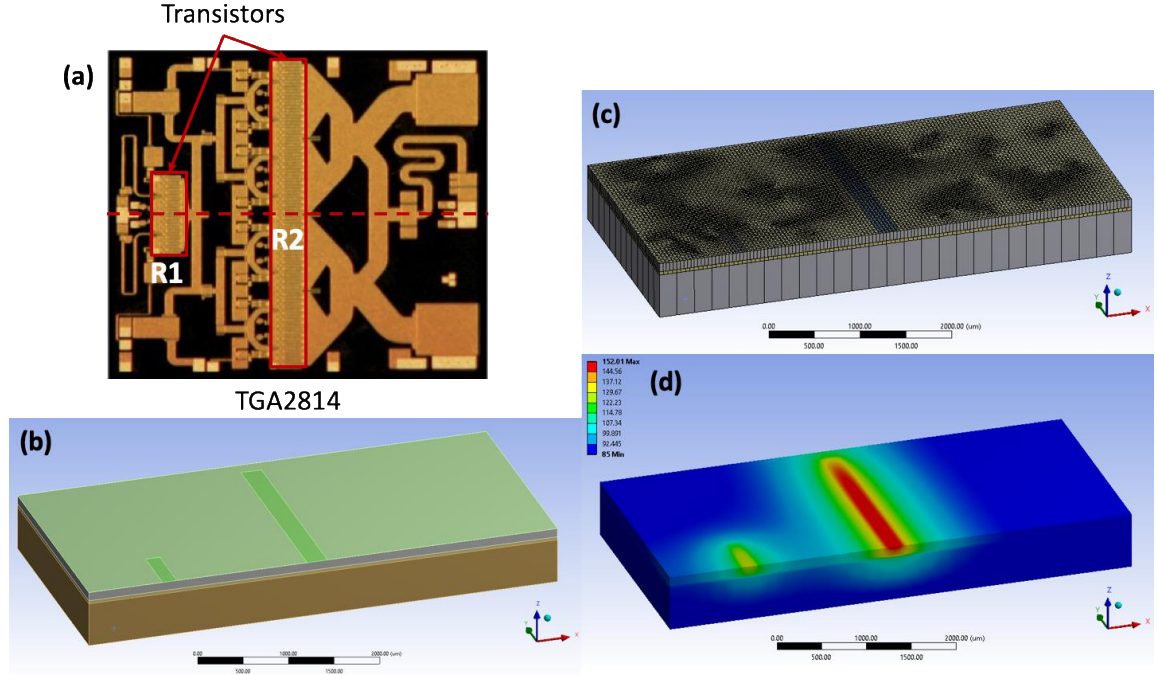


Figure 47. (a) Top-view of TriQuint TGA2814 GPA with active channel regions R1 and R2. (b) FEM geometry of GPA mounted on Mo/Cu heat sink. (c) Converged finite element mesh of GPA FEM. (d) Example of temperature distribution across the GPA FEM.

Table 4. Thermal conductivity of materials and GaN-substrate thermal boundary resistances (TBR_{eff}) used in the FEM of the GPA.

Material	Thermal Conductivity (W/mK)	GaN-Substrate TBR (m^2K/GW)
GaN ^a	$150(T/300)^{-1.4}$	-
SiC ^{a,b}	$420(T/300)^{-1.4}$	20
Grown PCD ^c	$1300(T/300)^{-0.9}$	29
Bonded PCD ^d	$2160(T/300)^{-0.9}$	34
Mo/Cu (20/80)	164	-
Au-Sn Solder	57	-

^aReference [66]

^bReference [40]

^cReference [76]

^dReference [29]

The FEM was meshed with a predominantly hexahedral mesh that only permitted tetrahedral elements to alleviate poor hexahedral aspect ratios where necessary. Mesh refinement was accomplished by assigning local mesh sizing controls, namely edge and body sizing. A mesh convergence analysis was performed by reducing the magnitude of the local mesh sizing controls to ensure the mesh near the heat sources was sufficiently refined and to optimize computational simulation time. The results of this mesh convergence analysis are shown in and demonstrate convergence of the device maximum temperature and illustrate the simulation times achieved for each mesh refinement. Although linear elements were appropriate for the linear heat diffusion in this FEM, quadratic elements were used for additional accuracy since simulation time remained sufficiently low.

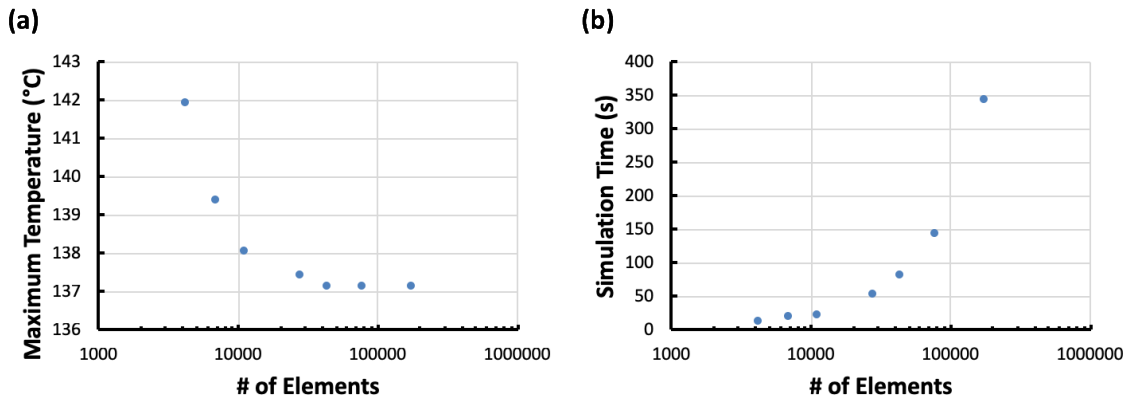


Figure 48. (a) Mesh convergence of maximum device temperature with respect to the number of quadratic elements. (b) Simulation times for each mesh refinement of the mesh convergence analysis.

3.4.2.2 Model Validation

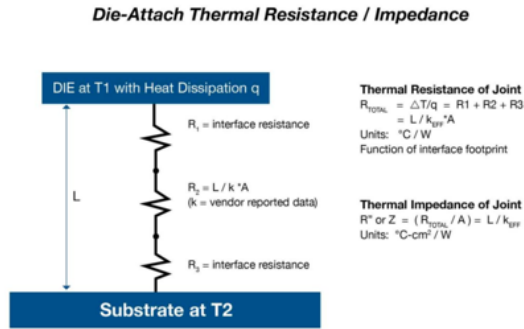
The FEM validation of the TGA2814 GPA was performed by comparing the maximum device temperature calculated from the simulation to the experimental

conditions reported by the manufacturer [111]. According to manufacturer experimental test results, the GPA was operated at electrical conditions that dissipated 59 W of output power while mounted to a 20 mils (508 μm) Mo/Cu base plate by a 1.5 mil (38 μm) Au/Sn solder die-attach layer. The maximum device temperature was measured to be 152 $^{\circ}\text{C}$, thus yielding a device total thermal resistance of 1.14 $^{\circ}\text{C}/\text{W}$. However by comparison, when the bulk thermal conductivity of the Au/Sn solder of 57 W/mK was input into the FEM, a maximum device temperature was simulated to be 136.5 $^{\circ}\text{C}$, approximately 15 $^{\circ}\text{C}$ lower than the experimental maximum temperature reported by the manufacturer. However, this discrepancy (shown in Figure 50) should be expected when performing modeling with the bulk material thermal conductivity of Au/Sn solder.

Typical of most die-attach materials, Au/Sn solder has been observed in literature to incur significant voiding and otherwise incomplete surface adhesion within the bond layer [113]. The thermal resistance from interfacial resistances, voiding, and other bond layer imperfections; the interfacial resistances between the bond layer and its adjoining material surfaces; and the intrinsic bond layer resistance (thermal conductivity divided by layer thickness) can all be lumped into one effective die-attach layer impedance as illustrated in Figure 49. An equivalent analysis performed by the device manufacturer demonstrates that an effective die-attach layer impedance may be extrapolated from FEM simulation by parameterizing the bond layer impedance as illustrated in Figure 49 [114]. In accordance with this analysis from literature, the interfaces conductances on either side of the bond layer were assumed to be infinite (zero resistance) and as such all of the layer impedance was lumped into the Au/Sn layer thermal conductivity. This effective layer thermal conductivity was parameterized in the FEM to determine the effective Au/Sn

thermal conductivity that corresponds to the experimental device maximum temperature of 152 °C. The results of this analysis are shown in Figure 50 and have concluded in an effective Au/Sn thermal conductivity of 15.6 W/mK that was used in the subsequent comparative analysis.

(a)



(b)

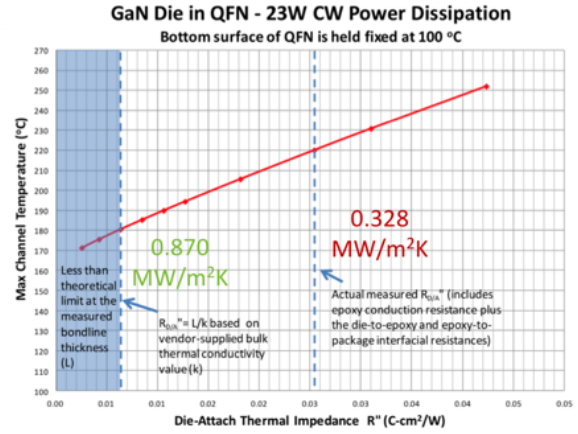


Figure 49. (a) Die-attach thermal resistance/impedance analysis schematic. (b) Effective die-attach impedance analysis published in literature. [114]

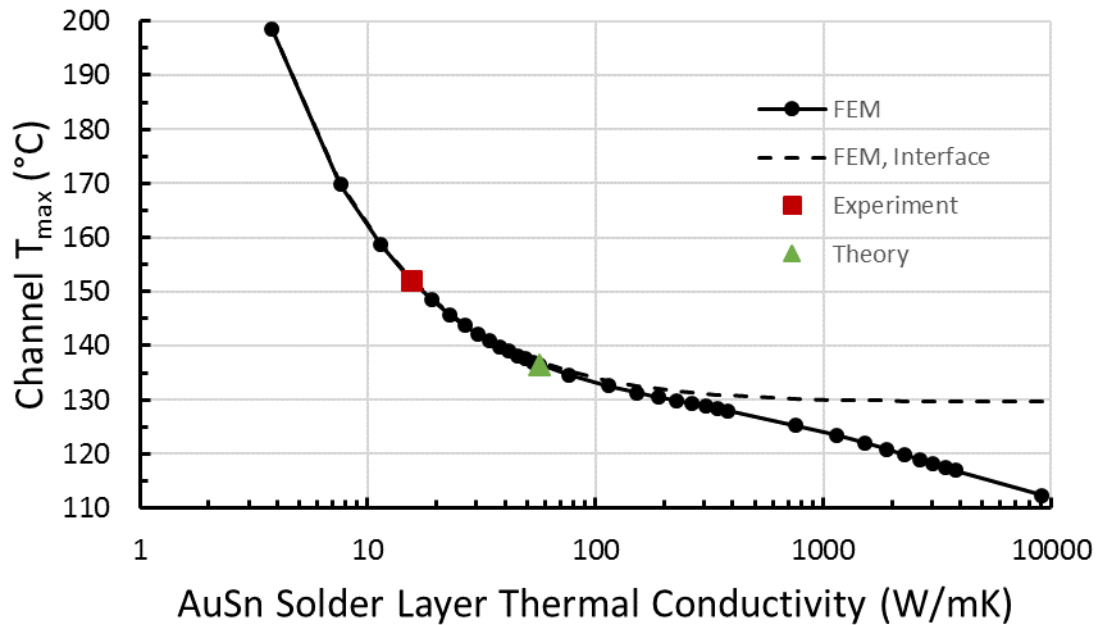


Figure 50. Effective die-attach thermal conductivity analysis performed by the parameterization of the Au/Sn solder thermal conductivity. The dashed line represents a model alternative in which the die-attach layer was removed and the total layer/interface impedance was treated as a single interface resistance. This idealization serves as a reference condition to illustrate the thermal management advantages from lateral heat spreading that are possible using high thermal conductivity interface layers.

3.4.2.3 Comparative Analysis

Having validated the physics and modelling assumptions of the steady-state thermal FEM, a comparative analysis was performed by parameterizing the heat dissipated by the GPA for three different GaN-on-substrate configurations: GaN on SiC (as manufactured), GaN-on-PCD via direct growth, and GaN-on-PCD via wafer bonding. As shown in Figure 51, the enhanced heat spreading through the highly conductive PCD substrates is critical for maintaining reasonable maximum channel temperatures for high-power applications. Furthermore, wafer bonding a high quality PCD substrate that has been pre-processed to remove the low-thermal conductivity nanocrystalline diamond (NCD) examined in CHAPTER 2 enables additional peak channel temperature reductions for high-power operating conditions (greater than 100 W or 7.5 W/mm). Considering the maximum operating temperature of the TGA2814 that is constrained by the maximum power density of 6.25 W/mm, the directly grown PCD substrate offers 11.25 W/mm (1.8x) of power density and the transfer bonded PCD offers 14 W/mm (2.24x) of power density.

Although our thermal FEM analysis has treated the thermal conductivity of the grown PCD substrate as homogeneous and isotropic, more extensive FEM thermal modelling presented in literature [40] has considered the thermal effects of the PCD anisotropy and cross-plane inhomogeneity. While considering an inhomogeneous and anisotropic thermal conductivity provided a more realistic cross-plane temperature distribution through the PCD substrate, the same peak channel temperature was achieved using an effective isotropic thermal conductivity of 1250 W/mK (at 300 K) as illustrated in Figure 52 [40]. Therefore, it is reasonable to assume a homogeneous and isotropic thermal conductivity of 1300 W/mK (at 300 K) as measured in literature [76] for the grown

PCD substrate considered in our analysis. Furthermore, additional improvements to the quality and structural integrity of low-temperature bonding technologies that reduce the GaN-PCD interface TBR_{eff} will extend the thermal gains possible for GaN-on-PCD HEMT technology.

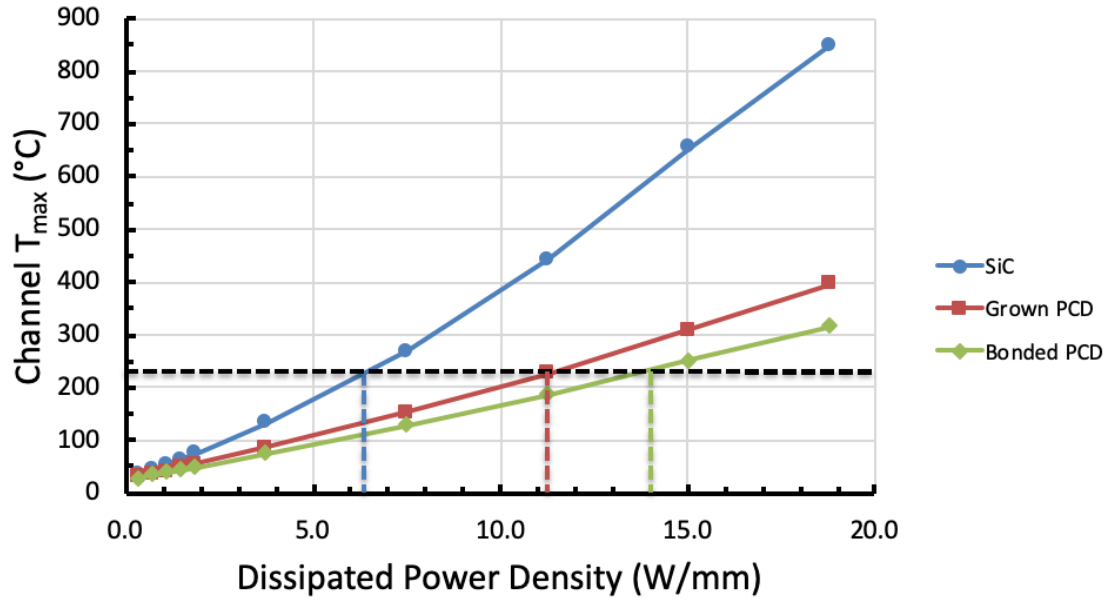


Figure 51. Temperature rise as a function of dissipated power density for each GaN-on-PCD implementation alternative to GaN-on-SiC. The horizontal (black) dashed line indicates the maximum operating temperature (for maximum power density of 6.25 W/mm).

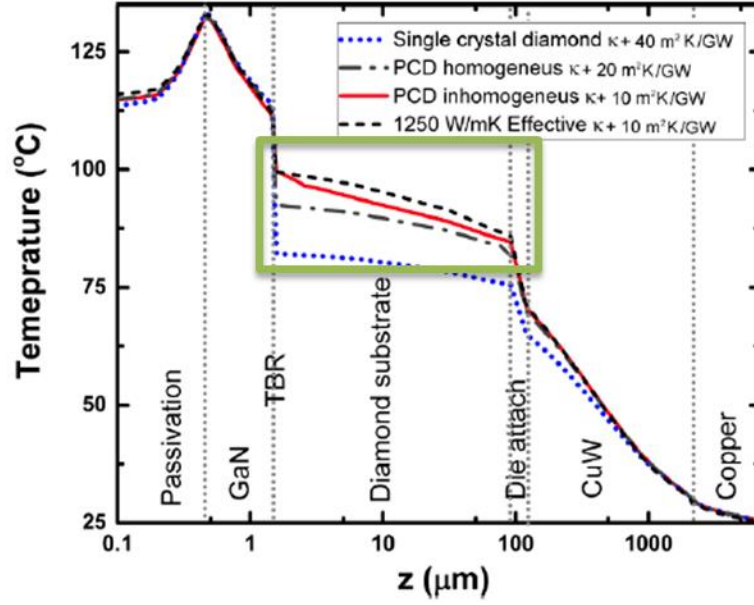


Figure 52. Steady-state thermal finite element analysis of an AlGaIn/GaN high-power amplifier device reproduced from literature [40] that shows the cross-plane temperature distribution through the device, substrate, and package for polycrystalline diamond thermal conductivities subject to various assumptions. Assuming an effective isotropic thermal conductivity of 1250 W/mK (at 300 K) (dashed black) yields the same peak channel temperature result as considering a (cross-plane) inhomogeneous and anisotropic thermal conductivity.

3.5 Summary and Conclusions

The three-dimensional (3D) stress distribution of three GaN-on-PCD wafers were measured via Raman and PL spectroscopy stress metrology techniques. Two wafers (G1 and G2) were fabricated by directly growing PCD onto the backside of AlGaIn/GaN heterostructures in place of the silicon (111) growth substrates, and one wafer (B) was fabricated by wafer bonding a pre-grown high quality PCD substrate to the backside of an AlGaIn/GaN heterostructure in place of the SiC growth substrate. The topside and backside PL stress results measured from all three wafers indicated the presence of a topside to backside transition from tensile to compressive stress across each GaN buffer layer thickness that were all approximately 730 nm thick. In addition, a decreasing trend was

found in the magnitude of the residual stresses observed from the progression of GaN-on-PCD wafers G1 to G2 to B. The heterostructure transfer process improvements implemented to improve interface quality between samples G1 and G2 resulted in the reduction of residual stress magnitude throughout the GaN layer of G2 with respect to G1. The precise agreement between the residual stresses measured from the bare and HEMT-processed die taken from wafer G2 demonstrates that the HEMT device fabrication processes did not significantly alter the residual stress state of the AlGaIn/GaN heterostructure. The magnitude of the residual stress throughout wafer B was observed to be significantly lower than those of wafers G1 and G2. However, it is not yet understood if the reduced residual stresses were caused by the less stress-inducing GaN-on-SiC epitaxy, the low-temperature bonding process, or a combination of both. Since prior work has demonstrated the residual stress state of the AlGaIn/GaN heterostructure to be a decisive factor that impacts HEMT device reliability under high bias conditions, an improved understanding of how particular process steps influence the magnitude of the substrate induced residual stress in the GaN layer of AlGaIn/GaN HEMTs is critical for ensuring optimal performance and reliability of GaN-on-PCD HEMT devices.

The most recent progress towards minimizing the GaN-diamond interface TBR_{eff} was summarized from literature and a steady-state thermal finite element model was used to demonstrate the thermal advantage gained by optimizing the near-interface PCD thermal conductivity through wafer bonding high quality bulk PCD without the initial NCD nucleation layers and further mitigating the GaN-diamond interface resistance.

CHAPTER 4. CONCLUSIONS AND FUTURE WORK

4.1 Research Summary

The combination of high critical breakdown field, high charge carrier saturation velocity, and large sheet charge density of AlGa_N/Ga_N heterostructures have enabled the development of AlGa_N/Ga_N HEMTs capable of high-power and high-frequency operation for RF applications such as wireless communication and advanced radar systems. AlGa_N/Ga_N HEMT technology has seen rapid development over recent years as a result of substrate and device heterostructure materials quality improvement, surface stabilization and passivation techniques development, and device and fabrication process engineering. However, despite superior performance over Si- and SiC-based MOSFET technologies, AlGa_N/Ga_N HEMT devices designed for RF applications have encountered inherent limitations due to highly localized self-heating that is harshly detrimental to device performance and reliability. To overcome these thermal management challenges, CVD diamond has been implemented as an alternative device substrate due to its extremely high thermal conductivity.

Although current Ga_N-on-PCD HEMT technology has demonstrated outstanding operating channel temperature reduction with minimal sacrifice to electrical performance with respect to Ga_N-on-SiC devices, the large thermal boundary resistance (TBR_{eff}) between the AlGa_N/Ga_N heterostructure and CVD diamond substrate has proven to be a critical bottleneck for heat removal from the micron-sized hot spot present during RF operation. Due to the combination of complex phonon scattering mechanisms at this highly disordered interface, the characterization of near-interface thermal properties has proven

difficult. Although several transient optical techniques have been demonstrated capable of resolving the thermal material and interface properties, such techniques require meticulous expertise and complex data analyses to resolve reliable results. Alternatively, simplified steady-state techniques have been recently developed to measure the in-plane thermal conductivity of thin nanocrystalline diamond films. However, the experimental results of obtained from these steady-state techniques lack consistency and a rigorous uncertainty estimation methodology. Since the magnitude of the in-plane thermal conductivity of the near-nucleation nanocrystalline diamond (NCD) present in PCD is a critical component of the GaN-diamond TBR, it is critical to establish the efficacy of accurate and reproducible in-plane thermal conductivity results obtained from such steady-state characterization techniques.

Therefore, in an effort to ensure a rigorous estimation of in-plane thermal conductivity and its overall uncertainty, an explicit uncertainty analysis framework has been developed in this work for two steady-state thermometry techniques: Raman thermometry and electrical resistance thermometry. Furthermore, the best practices and experimental conditions that permit the simplifying assumption of 1D thermal conduction along the in-plane direction have been presented. In addition, temperature dependent in-plane thermal conductivity measurements were demonstrated using electrical resistance thermometry to confirm the approximately temperature-independent nature of the suspended NCD membranes for moderate temperature excursions ($T_{max} - T_{min} < 130\text{ }^{\circ}\text{C}$). The in-plane thermal conductivity of six nanocrystalline CVD diamond suspended membrane samples organized into two sample sets were measured to perform comparative analyses intended to provide insight for improving the quality and thermal

properties of the initial near-nucleation layers of PCD films for heat spreading applications in GaN-on-PCD HEMT device technology.

Due to the diminished thermal transport near and across the GaN-PCD interface, various methods have been explored to improve the quality of the AlGaIn/GaN heterostructure, the PCD substrate, and the GaN-PCD interface. However, due to the high-temperature nature of many of these processes and the presence of CTE-mismatched interfaces, biaxial strain inevitably accumulates within the AlGaIn/GaN heterostructure that is intimately coupled to the electrical and structural integrity of the GaN-on-PCD HEMT devices. The recent development of optical techniques capable of accurate, reproduceable, and non-invasive biaxial stress measurements in GaN have led to the ability of resolving a through-thickness residual stress gradient within the GaN buffer layer of GaN-on-PCD HEMTs.

Therefore, in order to improve GaN-on-PCD processes for optimal HEMT device performance, the through-thickness residual stress distribution of three GaN-on-PCD wafers prepared according to different AlGaIn/GaN heterostructure transfer techniques was measured via Raman and PL spectroscopy. Two wafers were prepared by growing PCD directly on an AlGaIn/GaN heterostructure that was originally grown on Si (G1 and G2) and one wafer was prepared by low-temperature wafer bonding a pre-grown high-quality PCD substrate that was pre-processed to remove the low thermal conductivity nanocrystalline nucleation layer to an AlGaIn/GaN heterostructure that was originally epitaxially grown on SiC. The topside and backside PL stress results measured from all three wafers indicated the presence of a topside to backside transition from tensile to compressive stress across each GaN buffer layer thickness that were all approximately 730

nm thick and a decreasing trend was found in the magnitude of the residual stresses observed from the progression of GaN-on-PCD wafers G1 to G2 to B. In addition, the residual stress of the GaN buffer region of gate-drain access region of a HEMT processed on wafer G2 was measured to determine if the HEMT fabrication process affected the residual stress state of the heterostructure. The residual stress measured from the bare and HEMT-processed die from wafer G2 were in precise agreement. Although the magnitude of the residual stress throughout wafer B was observed to be significantly lower than those of wafers G1 and G2, it is not yet understood if the reduced residual stresses were caused by the less stress-inducing GaN-on-SiC epitaxy, the low-temperature bonding process, or a combination of both. In order to distinguish the residual stress effects of each process steps, residual stress measurements should be sampled in between subsequent process steps.

Finally, a steady-state thermal finite element model was used to demonstrate the thermal advantage gained by optimizing the near-interface PCD thermal conductivity through wafer bonding high quality bulk PCD without the initial NCD nucleation layers and further mitigating the GaN-PCD interface resistance. The comparative thermal modelling results have demonstrated the outstanding peak temperature reduction capable with present GaN-on-PCD technologies with respect to the high-power RF industry standard GaN-on-SiC technologies.

4.2 Future Work

Although wafer bonding high-quality PCD substrates to AlGaIn/GaN HEMT devices epitaxially grown on SiC has been determined to be the most thermally and

mechanically advantageous heterostructure transfer process solution to date, the optimum GaN-on-PCD heterostructure transfer solutions must also critically consider the long-term reliability of the GaN-PCD interface. Delamination or interfacial structural damage can critically degrade the ability to dissipate heat through the high thermal conductivity CVD diamond substrate. Therefore, the future success of GaN-on-PCD HEMT technology will critically depend the thermal, structural, and functional reliability of devices. Since it is now well known that the high-frequency operating conditions of RF high-power amplifiers introduces complex failure mechanisms that are absent and otherwise undetected by DC testing and modelling; transient thermal, structural, and electrical testing will be critical for commercializing highly reliable GaN-on-PCD HEMT technologies. Therefore, the next steps of the present work will involve *in situ* thermal characterization of GaN-on-PCD devices using transient thermoreflectance imaging (TTI) techniques [105, 115, 116] and the implementation of computationally efficient transient thermal modelling approaches [117] to advance our understanding of transient device failure mechanisms and, ultimately, to ensure the reliability of RF GaN-on-PCD HEMTs under high-power continuous- and pulse-mode operation. In addition, the through-thickness variations of the residual biaxial stress state in the AlGaN/GaN heterostructure accumulated by each wafer fabrication process for producing GaN-on-PCD wafers should be more comprehensively evaluated by performing Raman and PL stress measurements before and after each significant fabrication process step.

REFERENCES

1. Gurnett, K. and T. Adams, *Considerations for GaN-powered base stations*. III-Vs Review, 2006. **19**(7): p. 20-22.
2. Jimenez, J. and A. Moore, *GaN RF Technology for Dummies*. 2015.
3. Mishra, U.K., et al., *GaN-Based RF power devices and amplifiers*. Proceedings of the Ieee, 2008. **96**(2): p. 287-305.
4. Tsao, J., et al., *Ultrawide - Bandgap Semiconductors: Research Opportunities and Challenges*. Advanced Electronic Materials, 2018. **4**(1): p. 1600501.
5. Choi, S., et al., *The Analysis of Wide Band Gap Semiconductors Using Raman Spectroscopy*, in *Materials and Reliability Handbook for Semiconductor Optical and Electron Devices*, O. Ueda and S.J. Pearton, Editors. 2013, Springer New York: New York, NY. p. 545-582.
6. Ambacher, O., et al., *Two-dimensional electron gases induced by spontaneous and piezoelectric polarization charges in N- and Ga-face AlGaIn/GaN heterostructures*. Journal of Applied Physics, 1999. **85**(6): p. 3222-3233.
7. Brazzini, T., et al., *Hot-Electron Electroluminescence Under RF Operation in GaN-HEMTs: A Comparison Among Operational Classes*. IEEE Transactions on Electron Devices, 2017. **64**(5): p. 2155-2160.
8. Matulionis, A., *Hot phonons in GaN channels for HEMTs*. physica status solidi (a), 2006. **203**(10): p. 2313-2325.
9. Jones, J.P., et al., *Transient stress characterization of AlGaIn/GaN HEMTs due to electrical and thermal effects*. Microelectronics Reliability, 2015. **55**(12): p. 2634-2639.
10. Choi, S., et al., *The impact of mechanical stress on the degradation of AlGaIn/GaN high electron mobility transistors*. Journal of Applied Physics, 2013. **114**(16): p. 164501.
11. del Alamo, J.A. and J. Joh, *GaN HEMT reliability*. Microelectronics Reliability, 2009. **49**(9): p. 1200-1206.
12. Meneghesso, G., et al., *Reliability of GaN High-Electron-Mobility Transistors: State of the Art and Perspectives*. IEEE Transactions on Device and Materials Reliability, 2008. **8**(2): p. 332-343.

13. Joh, J. and J.A. del Alamo, *Critical voltage for electrical degradation of GaN high-electron mobility transistors*. IEEE Electron Device Letters, 2008. **29**(4): p. 287-289.
14. Joh, J., et al., *A model for the critical voltage for electrical degradation of GaN high electron mobility transistors*. Microelectronics Reliability, 2010. **50**(6): p. 767-773.
15. Park, S.Y., et al., *Physical degradation of GaN HEMT devices under high drain bias reliability testing*. Microelectronics Reliability, 2009. **49**(5): p. 478-483.
16. Bagnall, K.R., et al., *Electric field dependence of optical phonon frequencies in wurtzite GaN observed in GaN high electron mobility transistors*. Journal of Applied Physics, 2016. **120**(15): p. 155104.
17. Beechem, T., et al., *Assessment of stress contributions in GaN high electron mobility transistors of differing substrates using Raman spectroscopy*. Journal of Applied Physics, 2009. **106**(11): p. 114509.
18. Choi, S., et al., *Analysis of the residual stress distribution in AlGaIn/GaN high electron mobility transistors*. Journal of Applied Physics, 2013. **113**(9): p. 093510.
19. Pearson, S., et al., *GaN electronics for high power, high temperature applications*. Materials Science and Engineering: B, 2001. **82**(1-3): p. 227-231.
20. Schwierz, F. and O. Ambacher. *Recent advances in GaN HEMT development*. in *Electron Devices for Microwave and Optoelectronic Applications, 2003. EDMO 2003. The 11th IEEE International Symposium on*. 2003. IEEE.
21. Amano, H., et al., *The 2018 GaN power electronics roadmap*. Journal of Physics D: Applied Physics, 2018. **51**(16): p. 163001.
22. Micovic, M., et al. *High frequency GaN HEMTs for RF MMIC applications*. in *Electron Devices Meeting (IEDM), 2016 IEEE International*. 2016. IEEE.
23. Cho, J., et al., *Near-junction thermal management: Thermal conduction in gallium nitride composite substrates*. Ann. Rev. Heat Transfer, 2014. **18**.
24. Donmez, N. and S. Graham, *The impact of noncontinuum thermal transport on the temperature of AlGaIn/GaN HFETs*. IEEE Transactions on Electron Devices, 2014. **61**(6): p. 2041-2048.
25. Chou, Y., et al., *Degradation of AlGaIn/GaN HEMTs under elevated temperature lifetesting*. Microelectronics Reliability, 2004. **44**(7): p. 1033-1038.
26. Pomeroy, J.W., et al., *Operating channel temperature in GaN HEMTs: DC versus RF accelerated life testing*. Microelectronics Reliability, 2015. **55**(12): p. 2505-2510.

27. Ejeckam, F., et al. *GaN-on-diamond: A brief history*. in *Proc. IEEE Lester Eastman Conf. High Perform. Devices*. 2014.
28. Yates, L., et al., *Low Thermal Boundary Resistance Interfaces for GaN-on-Diamond Devices*. *Acs Applied Materials & Interfaces*, 2018. **10**(28): p. 24302-24309.
29. Chao, P.C., et al., *Low-Temperature Bonded GaN-on-Diamond HEMTs With 11 W/mm Output Power at 10 GHz*. *Ieee Transactions on Electron Devices*, 2015. **62**(11): p. 3658-3664.
30. Hirama, K., M. Kasu, and Y. Taniyasu, *RF high-power operation of AlGaIn/GaN HEMTs epitaxially grown on diamond*. *IEEE Electron Device Letters*, 2012. **33**(4): p. 513-515.
31. Dumka, D., et al. *Electrical and thermal performance of AlGaIn/GaN HEMTs on diamond substrate for RF applications*. in *Compound Semiconductor Integrated Circuit Symposium (CSICS), 2013 IEEE*. 2013. IEEE.
32. Altman, D., et al. *Analysis and characterization of thermal transport in GaN HEMTs on Diamond substrates*. in *Thermal and Thermomechanical Phenomena in Electronic Systems (ITherm), 2014 IEEE Intersociety Conference on*. 2014. IEEE.
33. Graham, S., *Thermal Transport in Diamond Films for Electronics Thermal Management*. 2018, Georgia Institute of Technology Atlanta United States.
34. May, P.W., *Diamond thin films: a 21st-century material*. *Philosophical Transactions of the Royal Society of London Series a-Mathematical Physical and Engineering Sciences*, 2000. **358**(1766): p. 473-495.
35. Kuo, K.-P., *Microwave-assisted plasma CVD of diamond films using thermal-like plasma discharge*. 1997, Michigan State University: Ann Arbor. p. 258.
36. Kamo, M., et al., *Growth and Formation of Diamond on Steel*. *Cryst J. Growth*, 1983. **62**: p. 642.
37. Bachmann, P.K., G. Gärtner, and H. Lydtin, *Plasma-Assisted Chemical Vapor Deposition Processes*. *MRS Bulletin*, 1988. **13**(12): p. 52-59.
38. Schreck, M., et al., *Large-area high-quality single crystal diamond*. *Mrs Bulletin*, 2014. **39**(6): p. 504-510.
39. Graebner, J.E., et al., *Phonon-Scattering in Chemical-Vapor-Deposited Diamond*. *Physical Review B*, 1994. **50**(6): p. 3702-3713.
40. Anaya, J., et al. *Thermal management of GaN-on-diamond high electron mobility transistors: Effect of the nanostructure in the diamond near nucleation region*. in

2016 15th IEEE Intersociety Conference on Thermal and Thermomechanical Phenomena in Electronic Systems (ITherm). 2016.

41. Anaya, J., et al., *Thermal conductivity of ultrathin nano-crystalline diamond films determined by Raman thermography assisted by silicon nanowires*. Applied Physics Letters, 2015. **106**(22).
42. Bougher, T.L., et al., *Thermal Boundary Resistance in GaN Films Measured by Time Domain Thermoreflectance with Robust Monte Carlo Uncertainty Estimation*. Nanoscale and Microscale Thermophysical Engineering, 2016. **20**(1): p. 22-32.
43. Koh, Y.K., et al., *Comparison of the 3 omega method and time-domain thermoreflectance for measurements of the cross-plane thermal conductivity of epitaxial semiconductors*. Journal of Applied Physics, 2009. **105**(5).
44. Rodin, D. and S.K. Yee, *Simultaneous measurement of in-plane and through-plane thermal conductivity using beam-offset frequency domain thermoreflectance*. Review of Scientific Instruments, 2017. **88**(1).
45. Sood, A., et al., *Anisotropic and inhomogeneous thermal conduction in suspended thin-film polycrystalline diamond*. Journal of Applied Physics, 2016. **119**(17).
46. Kommandur, S. and S. Yee, *A suspended 3-omega technique to measure the anisotropic thermal conductivity of semiconducting polymers*. Review of Scientific Instruments, 2018. **89**(11): p. 114905.
47. Yang, J., E. Ziade, and A.J. Schmidt, *Uncertainty analysis of thermoreflectance measurements*. Review of Scientific Instruments, 2016. **87**(1).
48. Anaya, J., et al., *Simultaneous determination of the lattice thermal conductivity and grain/grain thermal resistance in polycrystalline diamond*. Acta Materialia, 2017. **139**(Supplement C): p. 215-225.
49. Nazari, M., et al., *Optical characterization and thermal properties of CVD diamond films for integration with power electronics*. Solid-State Electronics, 2017. **136**: p. 12-17.
50. Squires, B., et al., *Hexagonal boron nitride particles for determining the thermal conductivity of diamond films based on near-ultraviolet micro-Raman mapping*. Journal of Physics D-Applied Physics, 2017. **50**(24).
51. Sood, A., et al., *Direct Visualization of Thermal Conductivity Suppression Due to Enhanced Phonon Scattering Near Individual Grain Boundaries*. Nano Letters, 2018. **18**(6): p. 3466-3472.

52. Anaya, J., et al., *Control of the in-plane thermal conductivity of ultra-thin nanocrystalline diamond films through the grain and grain boundary properties*. Acta Materialia, 2016. **103**: p. 141-152.
53. Williams, O.A., *Nanocrystalline diamond*. Diamond and Related Materials, 2011. **20**(5-6): p. 621-640.
54. Bougher, T.L., et al. *Experimental considerations of CVD diamond film measurements using time domain thermoreflectance*. in *Thermal and Thermomechanical Phenomena in Electronic Systems (ITherm)*, 2017 16th IEEE Intersociety Conference on. 2017. IEEE.
55. Ferraro, J.R., *Introductory raman spectroscopy*. 2003: Elsevier.
56. Jimenez, J. and J.W. Tomm, *Raman Spectroscopy*, in *Spectroscopic Analysis of Optoelectronic Semiconductors*. 2016, Springer International Publishing: Switzerland. p. 77-142.
57. Beechem, T.E. and J.R. Serrano, *Raman Thermometry of Microdevices: Choosing a Method to Minimize Error*. Spectroscopy, 2011. **26**(11): p. 36-44.
58. Beechem, T., L. Yates, and S. Graham, *Invited Review Article: Error and uncertainty in Raman thermal conductivity measurements*. Review of Scientific Instruments, 2015. **86**(4).
59. Simon, R.B., J.W. Pomeroy, and M. Kuball, *Diamond micro-Raman thermometers for accurate gate temperature measurements*. Applied Physics Letters, 2014. **104**(21).
60. Dallas, J., et al., *Thermal characterization of gallium nitride p-i-n diodes*. Applied Physics Letters, 2018. **112**(7): p. 073503.
61. Du, Y.L., Y. Deng, and M.S. Zhang, *Variable-temperature Raman scattering study on anatase titanium dioxide nanocrystals*. Journal of Physics and Chemistry of Solids, 2006. **67**(11): p. 2405-2408.
62. Burda, C., et al., *Enhanced nitrogen doping in TiO₂ nanoparticles*. Nano Letters, 2003. **3**(8): p. 1049-1051.
63. Achatz, P., et al., *Optical properties of nanocrystalline diamond thin films*. Applied Physics Letters, 2006. **88**(10).
64. Cahill, D.G., *Thermal-Conductivity Measurement from 30-K to 750-K - the 3-Omega Method*. Review of Scientific Instruments, 1990. **61**(2): p. 802-808.
65. Pavlidis, G., et al., *Characterization of AlGaIn/GaN HEMTs Using Gate Resistance Thermometry*. Ieee Transactions on Electron Devices, 2017. **64**(1): p. 78-83.

66. Sarua, A., et al., *Thermal boundary resistance between GaN and substrate in AlGaIn/GaN electronic devices*. Ieee Transactions on Electron Devices, 2007. **54**(12): p. 3152-3158.
67. Bergman, T.L., et al., *Fundamentals of Heat and Mass Transfer*. Seventh Edition ed. 2011: John Wiley & Sons, Inc.
68. Cabaleiro, D., et al., *Thermal conductivity of dry anatase and rutile nano-powders and ethylene and propylene glycol-based TiO₂ nanofluids*. The Journal of Chemical Thermodynamics, 2015. **83**: p. 67-76.
69. Mollart, T.P., et al., *Factors affecting the optical performance of CVD diamond infrared optics*. Semiconductor Science and Technology, 2003. **18**(3): p. S117-S124.
70. Edalatpour, S. and M. Francoeur, *Size effect on the emissivity of thin films*. Journal of Quantitative Spectroscopy & Radiative Transfer, 2013. **118**: p. 75-85.
71. Papadopoulos, C.E. and H. Yeung, *Uncertainty estimation and Monte Carlo simulation method*. Flow Measurement and Instrumentation, 2001. **12**(4): p. 291-298.
72. Wei, C.D., et al., *Invited Article: Micron resolution spatially resolved measurement of heat capacity using dual-frequency time-domain thermoreflectance*. Review of Scientific Instruments, 2013. **84**(7).
73. Liu, W.L., et al., *Thermal conduction in nanocrystalline diamond films: Effects of the grain boundary scattering and nitrogen doping*. Applied Physics Letters, 2006. **89**(17).
74. Cheaito, R., et al. *Thermal conductivity measurements on suspended diamond membranes using picosecond and femtosecond time-domain thermoreflectance*. in *Thermal and Thermomechanical Phenomena in Electronic Systems (ITherm)*, 2017 *16th IEEE Intersociety Conference on*. 2017. IEEE.
75. Liu, D., et al., *Impact of diamond seeding on the microstructural properties and thermal stability of GaN-on-diamond wafers for high-power electronic devices*. Scripta Materialia, 2017. **128**: p. 57-60.
76. Sun, H., et al., *Temperature-dependent thermal resistance of GaN-on-diamond HEMT wafers*. IEEE Electron Device Letters, 2016. **37**(5): p. 621-624.
77. Won, Y., et al., *Fundamental cooling limits for high power density gallium nitride electronics*. IEEE Transactions on Components, Packaging and Manufacturing Technology, 2015. **5**(6): p. 737-744.
78. Yamamoto, Y., et al., *The measurement of thermal properties of diamond*. Diamond and Related Materials, 1997. **6**(8): p. 1057-1061.

79. Hirama, K., Y. Taniyasu, and M. Kasu, *AlGaN/GaN high-electron mobility transistors with low thermal resistance grown on single-crystal diamond (111) substrates by metalorganic vapor-phase epitaxy*. Applied Physics Letters, 2011. **98**(16): p. 162112.
80. Su, J., et al., *Stress engineering with AlN/GaN superlattices for epitaxial GaN on 200 mm silicon substrates using a single wafer rotating disk MOCVD reactor*. Journal of Materials Research, 2015. **30**(19): p. 2846-2858.
81. Wośko, M., et al., *GaN/AlN superlattice high electron mobility transistor heterostructures on GaN/Si (111)*. physica status solidi (b), 2015. **252**(5): p. 1195-1200.
82. Francis, D., et al., *Formation and characterization of 4-inch GaN-on-diamond substrates*. Diamond and Related Materials, 2010. **19**(2-3): p. 229-233.
83. Ejeckam, F., et al., *GaN-on-diamond: the next GaN*. Microwave journal. Internation. ed., 2014. **57**(5): p. 124-128.
84. Cho, J., et al., *Phonon conduction in GaN-diamond composite substrates*. Journal of Applied Physics, 2017. **121**(5).
85. Sun, H., et al., *Reducing GaN-on-diamond interfacial thermal resistance for high power transistor applications*. Applied Physics Letters, 2015. **106**(11): p. 111906.
86. English, T.S., et al., *Enhancing and tuning phonon transport at vibrationally mismatched solid-solid interfaces*. Physical review B, 2012. **85**(3): p. 035438.
87. Gordiz, K. and A. Henry, *Phonon transport at crystalline Si/Ge interfaces: the role of interfacial modes of vibration*. Scientific reports, 2016. **6**: p. 23139.
88. Pomeroy, J.W., et al., *Low thermal resistance GaN-on-diamond transistors characterized by three-dimensional Raman thermography mapping*. Applied Physics Letters, 2014. **104**(8).
89. Reeber, R.R. and K. Wang, *Lattice parameters and thermal expansion of GaN*. Journal of Materials Research, 2000. **15**(1): p. 40-44.
90. Edwards, M.J., et al., *Modelling wafer bow in silicon–polycrystalline CVD diamond substrates for GaN-based devices*. Journal of Physics D: Applied Physics, 2010. **43**(38): p. 385502.
91. Liu, D., et al., *GaN-on-diamond electronic device reliability: Mechanical and thermo-mechanical integrity*. Applied Physics Letters, 2015. **107**(25): p. 251902.
92. Hancock, B.L., et al., *Ultraviolet and visible micro-Raman and micro-photoluminescence spectroscopy investigations of stress on a 75-mm GaN-on-diamond wafer*. physica status solidi c, 2017. **14**(8): p. 1600247.

93. Feng, Z.C. *Micro-Raman scattering and micro-photoluminescence of GaN thin films grown on sapphire by metalorganic chemical vapor deposition*. 2002. SPIE.
94. Wang, F., et al., *Residual thermal strain in thick GaN epilayers revealed by cross-sectional Raman scattering and cathodoluminescence spectra*. Semiconductor science and technology, 2007. **22**(8): p. 896.
95. Wagner, J.-M. and F. Bechstedt, *Properties of strained wurtzite GaN and AlN: Ab initio studies*. Physical Review B, 2002. **66**(11): p. 115202.
96. Li, Y., et al., *Biaxial stress-dependent optical band gap, crystalline, and electronic structure in wurtzite ZnO: Experimental and ab initio study*. Journal of applied physics, 2008. **104**(8): p. 083516.
97. Choi, S., *Stress metrology and thermometry of AlGaIn/GaN HEMTs using optical methods*. 2013, Georgia Institute of Technology.
98. Beechem, T., et al., *Micro-Raman thermometry in the presence of complex stresses in GaN devices*. Journal of Applied Physics, 2008. **103**(12).
99. Batten, T., et al., *Simultaneous measurement of temperature and thermal stress in AlGaIn/GaN high electron mobility transistors using Raman scattering spectroscopy*. Journal of Applied Physics, 2009. **106**(9): p. 094509.
100. Choi, S., et al., *Thermometry of AlGaIn/GaN HEMTs Using Multispectral Raman Features*. Ieee Transactions on Electron Devices, 2013. **60**(6): p. 1898-1904.
101. Bagnall, K.R., et al., *Simultaneous measurement of temperature, stress, and electric field in GaN HEMTs with micro-Raman spectroscopy*. Review of Scientific Instruments, 2017. **88**(11): p. 113111.
102. Zhao, D., et al., *Stress and its effect on optical properties of GaN epilayers grown on Si (111), 6H-SiC (0001), and c-plane sapphire*. Applied physics letters, 2003. **83**(4): p. 677-679.
103. Muth, J., et al., *Absorption coefficient, energy gap, exciton binding energy, and recombination lifetime of GaN obtained from transmission measurements*. Applied Physics Letters, 1997. **71**(18): p. 2572-2574.
104. Hancock, B.L., et al., *Ultraviolet micro-Raman spectroscopy stress mapping of a 75-mm GaN-on-diamond wafer*. Applied Physics Letters, 2016. **108**(21): p. 211901.
105. Tadjer, M.J., et al., *Electrothermal Evaluation of AlGaIn/GaN Membrane High Electron Mobility Transistors by Transient Thermoreflectance*. IEEE Journal of the Electron Devices Society, 2018. **6**: p. 922-930.

106. Komiak, J.J., K. Chu, and P.C. Chao. *Decade bandwidth 2 to 20 GHz GaN HEMT power amplifier MMICs in DFP and No FP technology*. in *2011 IEEE MTT-S International Microwave Symposium*. 2011.
107. Burton, J., et al., *Spatial characterization of doped SiC wafers by Raman spectroscopy*. Journal of Applied Physics, 1998. **84**(11): p. 6268-6273.
108. Richter, H., Z. Wang, and L. Ley, *The one phonon Raman spectrum in microcrystalline silicon*. Solid State Communications, 1981. **39**(5): p. 625-629.
109. Ižák, T., et al., *Temperature-dependent stress in diamond-coated AlGaIn/GaN heterostructures*. Materials & Design, 2016. **106**: p. 305-312.
110. Jirásek, V., et al., *Investigation of residual stress in structured diamond films grown on silicon*. Thin Solid Films, 2015. **589**: p. 857-863.
111. TriQuint, *TGA2814: 3.1 - 3.6 GHz 80W GaN Power Amplifier*. 2013, TriQuint.
112. Heller, E., et al., *Electrical and structural dependence of operating temperature of AlGaIn/GaN HEMTs*. Microelectronics Reliability, 2013. **53**(6): p. 872-877.
113. Kim, H.-H., et al., *Thermal transient characteristics of die attach in high power LED PKG*. Microelectronics Reliability, 2008. **48**(3): p. 445-454.
114. Murdock, D. and M.C. Woods, *White Paper: GaN Thermal Analysis for High-Performance Systems*. Qorvo.
115. Pavlidis, G., et al., *Transient Thermal Characterization of AlGaIn/GaN HEMTs Under Pulsed Biasing*. IEEE Transactions on Electron Devices, 2018. **65**(5): p. 1753-1758.
116. Pavlidis, G., et al. *Improving the Transient Thermal Characterization of GaN HEMTs*. in *2018 17th IEEE Intersociety Conference on Thermal and Thermomechanical Phenomena in Electronic Systems (ITherm)*. 2018.
117. Bagnall, K.R. and E.N. Wang, *Theory of Thermal Time Constants in GaN High-Electron-Mobility Transistors*. IEEE Transactions on Components, Packaging and Manufacturing Technology, 2018. **8**(4): p. 606-620.